University of Alberta

Light Scattering in an Integrated Microfluidic Waveguide Cytometer

by

Xuantao Su 

A thesis submitted to the Faculty of Graduate Studies and Research
in partial fulfillment of the requirements for the degree of

Doctor of Philosophy

Department of Physics

Edmonton, Alberta

Spring 2008

Your file Votre référence
ISBN: 978-0-494-45612-5
Our file Notre référence
ISBN: 978-0-494-45612-5

Abstract

This dissertation presents a 2D cytometric technique for the study of light scattering from single scatterers. Compared with conventional 1D cytometric technique, this method gives a better understanding of the light scattering mechanism and is more useful for cellular diagnostics.

An integrated microfluidic optical waveguide cytometer is developed. This addresses many interesting interdisciplinary issues such as integration of laser optics with a liquid-core waveguide and single particle immobilization in a fluidic flow. The operation of this cytometer is validated by performing analyses on polystyrene microbeads. The all planar structures without the need for an optical lens between the scatterer and the sensor simplify both the experiment and theoretical modeling of the system. The obtained 2D scatter patterns allow identification of the location of 90 degree scatter. Good agreement between experimental spectra and Mie theory simulations is obtained. A Fourier method is developed for microsize differentiation.

Finite-Difference Time-Domain (FDTD) simulations are applied in our cytometer to give 2D scatter patterns from biological cells. Experimental 2D scatter patterns are obtained from yeast and human Raji cells. These scatter patterns are compared with the FDTD simulations. Our results show that cellular microstructures generate fringes of scattered light, allowing the Fourier method to

be applied to determine the yeast cell sizes. In the Raji cells the light scattered by the mitochondria dominates the scatter pattern, forming compact regions of high intensity that we term "small scale 2D structures". The analysis of these structures may ultimately be a useful diagnostic technique.

Mitochondrial aggregation in single cells is studied by FDTD simulations. Small angle forward scattering is used to differentiate normal cell models from cancerous ones. Fourier spectra of the wide angle side scattered light show that the highest dominant frequency can be used to determine cell sizes, while mitochondria contribute to lower frequency components.

In summary, we develop a 2D cytometric technique for the analysis of microscopic particles and biological cells. This technique has potential clinical applications such as detection of mitochondria-related diseases. With the advances of "lab-on-a-chip" techniques, a miniaturized inexpensive 2D cytometer can be of further interest.

Preface

This dissertation is in accordance to the "paper format" regulations of the Faculty of Graduate Studies and Research, University of Alberta, and is based on the following published papers and other papers in preparation.

1. X. T. Su, K. Singh, C. Capjack, J. Petracek, C. Backhouse and W. Rozmus, "Measurements of light scattering in an integrated microfluidic waveguide cytometer," *Journal of Biomedical Optics* (accepted).
2. X. T. Su, C. Capjack, W. Rozmus and C. Backhouse, "2D light scattering patterns of mitochondria in single cells," *Optics Express* **15**, 10562-10575 (2007).
3. X. T. Su, W. Rozmus, C. Capjack and C. Backhouse, "Side scatter light for micro-size differentiation and cellular analysis," *Proc. of SPIE* **6446**, 64460w (2007).
4. K. Singh, X. T. Su, C. G. Liu, C. Capjack, W. Rozmus and C. J. Backhouse, "A miniaturized wide-angle 2D cytometer," *Cytometry Part A* **69A**, 307-315 (2006).

Acknowledgements

I would like to thank my supervisors Dr. Wojciech Rozmus, Dr. Clarence Capjack and Dr. Christopher Backhouse for the guidance and support over the course of my program. I would especially like to thank Dr. Clarence Capjack for funding me for international conferences and the many long talks and discussions.

I thank the members of my supervisory committee, Dr. Mark Freeman and Dr. Ying Tsui, for many valuable suggestions. I thank other members of my examination committee, Dr. Richard London and Dr. Sharon Morsink, for the improvements of my thesis. In addition, I thank the former group members, Dr. Caigen Liu and Dr. Kirat Singh, for valuable discussions. In particular, I would like to thank Dr. Caigen Liu for providing me with the original "AETHER" FDTD code.

I am grateful to the people in the Applied Miniaturization Lab, WestGrid (University of Alberta) and Nanofab (University of Alberta), particularly Dr. Jon Johansson for the help in biological cell visualizations. I would also like to thank Jana Lauzon, Dr. Moira Glerum and Dr. Linda Pilarski for assistance with the human Raji cells.

I thank my parents and family for their love and support through the years.

Table of contents

List of tables

List of figures

List of symbols

ABC	absorbing boundary condition
Al	aluminum
AVS	Advanced Visual Systems
c	light speed in vacuum
CCD	charge coupled device
C	Celsius
δ	step size
DEP	dielectrophoresis
Δt	time step size
Δx	space grid spacing along x axis
DFT	discrete Fourier transform
DNA	deoxyribonucleic acid
dpi	dots per inch
$\vec{E}$	electric field
E. coli	*Escherichia coli*
ε	permittivity
FDTD	Finite-Difference Time-Domain
FFT	fast Fourier transform
GB	Gigabyte
$\vec{H}$	magnetic field
HAD	Hole-Accumulation Diode
I	intensity flux
IPA	isopropyl alcohol
$\vec{J}_s$	electric currents
$\vec{k}$	wave propagation vector

λ	wavelength
LED	light-emitting device
LOC	lab-on-a-chip
m	relative refractive index
$\bar{M}_s$	magnetic currents
μm	micrometer
μ	permeability
mL	milliliter
mm	millimeter
mW	milliwatt
n	refractive index
nm	nanometer
NSOM	near-field scanning optical microscopy
OCT	optical coherence tomography
ω	angular frequency
OPD	optical path difference
P_n^m	associated Legendre functions
PBS	phosphate buffered saline
PDMS	polydimethylsiloxane
φ	azimuth angle
PML	perfectly matched layer
PMTs	photomultiplier tubes
QE	quantum efficiency
RBC	red blood cell
RDG	Rayleigh-Debye-Gans
rpm	revolutions per minute
s	second
S	element of the scattering amplitude matrix
SD	standard deviation

SGI	Silicon Graphics Inc.
S/N	signal to noise
SPR	surface plasmon resonance
t	amplitude transmission coefficient
T	transmission
TE	transverse electric
TF/SF	total-field/scattered-field
θ	polar angle
TM	transverse magnetic
UV	ultra-violet
WKB	Wentzel-Kramers-Brillouin
z_n	spherical Bessel functions

Chapter 1

Introduction

Many diseases such as cancer result from defects in fundamental cell regulatory mechanisms, thus they are diseases that ultimately have to be understood at the molecular or cellular levels.[1] However, this understanding is not easily achieved. For example, diffraction effects limit the resolution that can be obtained with conventional optical microscopy to dimensions of the order of the illumination light wavelength.[2] Although an electron microscope has a very high resolution, the cell samples must be fixed, stained and thinly sliced.[3] Furthermore, electron microscopy can only characterize the cellular structures at one moment in time.[4] A better understanding of cell biology requires that the cellular information be obtained in living cells, and preferably non-destructively.

Bio-labels have been used to enhance the optical contrast for the study of cellular structure *in vivo*. Fluorophores[5-8] and quantum dots[9, 10] are widely used bio-labels. The main drawbacks of the fluorescence technique include photo-bleaching that will eventually transform the excited fluorophore into a non-fluorescent product, and blinking (alternation of on-fluorescing and off-fluorescing states).[11] Although passivated semiconductor nanocrystals resist bleaching longer than fluorophores, they also bleach eventually.[9] The more appealing labels are metal particles because they do not photo-bleach and do not optically saturate at reasonable exciting intensities.[11, 12] These bio-labeling

techniques however are invasive to the living cells, and may change the cellular functions.

Light scattering as a non-invasive, label-free technique can be used to obtain cellular information of living cells.[13] Recent developments have shown that light scattering techniques are promising in precancerous detections.[14, 15] Scattered light has also been measured in dark field microscopy,[16] confocal microscopy[17-19] and optical coherence tomography (OCT)[20, 21] to obtain cellular information *in vivo*. The side-scattered light (large angle scattering), is measured in dark field microscopy, while in confocal microscopy and OCT the backward-scattered light is used. Such techniques demand a fundamental understanding of light scattering in biological tissues.

Flow cytometry measures cells or particles in a fluid stream as they pass through a measuring apparatus.[22] Light scattering measurements in a flow cytometer can be used to obtain cellular information *in vivo*/*in vitro*. The integration of light sources, detectors and microfluidic chips makes flow cytometry of interest to many fields such as laser optics, photonics and microfluidics.[22-24] Furthermore, the recently-developed "lab-on-a-chip" (LOC) technology shows promise in developing miniaturized inexpensive flow cytometers.[25-28] Thus, the developments and measurements of light scattering in a novel flow cytometer will not only benefit the understanding of light scattering mechanism from cells or particles, but also have other potential applications in the biomedical field.

1.1 Cell biology

Biological cells are divided into two main classes, prokaryotic cells (bacteria) and eukaryotic cells, according to whether they have a nucleus or not. The prokaryotes lack a nuclear envelope and have diameters approximately 1 to 10μm.[1] A typical prokaryotic cell is *Escherichia coli* (E. coli). Most prokaryotes do not contain cytoplasmic organelles except for the many ribosomes (the sites of protein

synthesis). Unlike the prokaryotes, most eukaryotes contain a nucleus and are much more complex, with a variety of other cytoplasmic organelles. Eukaryotes are of more interest for better understanding the organelles in biological cells.

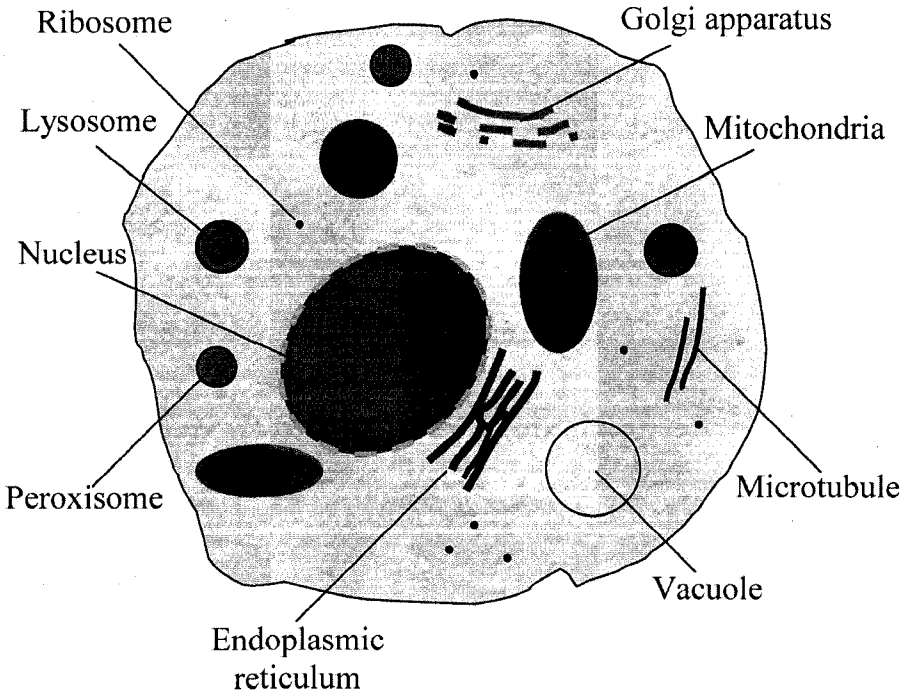

Figure 1.1 A cross section illustration of the representative components in a typical animal cell.

Figure 1.1 shows an illustration of a typical eukaryotic cell. The largest organelle of a eukaryotic cell is the nucleus. The nucleus is the site of the deoxyribonucleic acid (DNA). Mitochondria contain their own DNA and are the sites for cell respiration. Other important organelles in a typical eukaryotic cell include lysosomes (for digestive enzymes), peroxisomes (for specific enzymes) and Golgi apparatus (to process and package proteins and lipids). Among all types of organelles, the nucleus and the mitochondria are widely studied for providing a better understanding of many diseases. For example, cancerous cells are characterized by an increased nuclear size.[14, 15, 29] Mitochondria have been reported to serve as the central control point of apoptosis (a programmed cell

death, key in better understanding tumors).[30] There are also many other mitochondria-related diseases, such as Alzheimer's and Parkinson's.[31] Thus, both the nucleus and mitochondria are of great interest in light scattering cellular measurements.

Cell component	Size (Diameter)	Refractive index	Volume ratio
Cytoplasm	**10~30μm**	**1.38**	**50~80%**
Nucleus	**3~10μm**	**1.39**	**5~10%**
Mitochondrion	**0.3~0.7μm**	**1.42**	**5~15%**
Lysosome	**0.2~0.5μm**	**1.3785**	**1~10% (including many other organelles)**

Table 1.1 Important eukaryotic cell components and their size, refractive index and volume ratio (see references in the text).

As can be seen from Table 1.1, the nucleus and mitochondria are of different sizes (volume ratios) and refractive indices in eukaryotic cells compared with other organelles. Typically, the cell cytoplasm has a diameter of 10~30μm, the nucleus has a diameter about 3~10μm, the mitochondrion has a diameter of 0.3~0.7μm, and the peroxisome and lysosome are approximately the same size of 0.2~0.5μm in diameter.[1] The volume ratio (total volume of each cell component to the entire cell volume) of each cell component varies, but typically the cell cytoplasm occupies 50~80% of the total cell volume, the nucleus 5~10%, mitochondria 5~15%, and all the other organelles 1~10%.[32] Although the values for the refractive index of each cell component are not definitive for different types of cells, typical cell cytoplasm has a refractive index of 1.38,[33] nucleus 1.39,[34] and the mitochondrion 1.42.[35] The nucleus and mitochondria can be differentiated from the cytoplasm and other organelles due to their typical refractive indices. As can be see from Table 1.1, the cell cytoplasm, nucleus and the mitochondria occupy a very large fraction of the total cell volume. All the other cell components occupy a very small volume fraction, and some of them

have a refractive index very close to the cell cytoplasm (*e.g.* the cell lysosome has a refractive index of 1.3785[36]). Due to the small volume fraction and a refractive index that is comparable to the cell cytoplasm, the other organelles (lysosomes, peroxisomes…) will scatter light much more weakly compared with the cell cytoplasm, nucleus and the mitochondria.

1.2 Current research involving light scattering from particles and biological systems

1.2.1 Theoretical approaches

Light scattering occurs when light propagates through a medium in which there is a variation in refractive index. For the case of light propagation in a typical biological cell, the variations in the refractive index have a spatial scale of the same order of the incident light wavelength or even smaller. Thus an electromagnetic approach has to be used to resolve light scattering from biological cells. The well-known Maxwell's Equations govern the light propagation in any medium. Analytical and numerical methods can be used to solve Maxwell's Equations in light scattering studies.

Mie theory gives the analytical solution of light scattering from a homogeneous spherical scatterer excited by a plane wave.[37-39] Mie theory can be simplified as Rayleigh scattering and Fraunhofer scattering for very small (scatterer diameter far less than the illumination wavelength) and very big (scatterer diameter far greater than the illumination wavelength) scatterers, respectively.[2, 39] Mie theory has been used as an approximation to study the light scattering from biological tissues, where the scatterer is assumed to be spherical and homogeneous. Recently, Mie theory has been applied to study coated-layer spheres[39] although this model is still not accurate in real biological situations. As Mie theory demands a rigid solution of the boundary problems, it is invalid to use Mie theory for the light scattering from biological cells with arbitrary shapes and complex inner structures.

Rayleigh-Debye-Gans (RDG) theory[38, 40] and the Wentzel-Kramers-Brillouin (WKB) method[41, 42] are commonly used as approximate analytical methods to solve light scattering from homogeneous particles with arbitrary shapes. However both methods are only applicable to the situations of light scattering from "optically soft" particles, that is, the relative refractive index magnitude of the particle to the surrounding medium is approximately equal to 1.[38] Other disadvantages are that the RDG method has a limitation on the particle size compared to the incident wavelength, and the WKB method ignores the wave polarization effects. Furthermore, the RDG and WKB methods are impractical to solve light scattering from biological cells with complex inner structure. All these limit the applications of RDG and WKB methods in solving light scattering from biological cells.

The light scattering from biological cells with arbitrary shapes and randomly distributed organelles require a numerical solution of the Maxwell's Equations. The T-matrix method[43, 44] and the coupled dipole method[45, 46] have been used to simulate light scattering from an inhomogeneous object. However the T-matrix method is usually used for symmetric particles, while the coupled dipole method is limited to particle size comparable to the incident wavelength, since the solution does not converge for large particles.

Recently, the Finite-Difference Time-Domain (FDTD) method has been widely used to numerically determine light scattering from inhomogeneous cells with arbitrary shapes.[47-51] The FDTD technique solves Maxwell's Equations both in spatial and temporal steps in the near field of the object. The near field data are transferred to the far field where most observations of light scattering are performed experimentally. Although computationally intensive, the FDTD technique is readily applied to arbitrarily inhomogeneous particles. The FDTD technique can be used to predict the light scattering from arbitrary biological cells with various randomly distributed organelles.

1.2.2 Experimental approaches

Measurements of fluorescence light and/or scattered light are commonly used to obtain cellular information.[22] Compared with the fluorescence technique, light scattering measurements serve as a label-free non-invasive technique to probe biological cells. Recently, light scattering has attracted intensive interest in the experimental study of biological tissues and cells.

The single scattering technique has been used to obtain nucleus information in biological tissues.[14, 15, 52] Polarized light scattering spectroscopy has been used to distinguish between single backscattered light and multiply scattered light.[52] The size distribution of the cell nuclei and their refractive indices can be obtained via this technique. An alternative method of angle-resolved low-coherence interferometry has recently been developed to obtain nucleus size distributions.[4] All the above analyses are based on the comparisons between experimental results and Mie theory simulations. However, most biological cells (with arbitrary shapes) contain not only nuclei but also many randomly distributed organelles. The more accurate FDTD method needs to be adopted for a better understanding of light scattering from these biological cells.

Goniometric measurement of light scattering has been applied to obtain information from biological systems involving multiple scattering.[53] The obtained experimental results are compared with FDTD simulations. The scattering properties are strongly influenced by cellular biochemical and morphological structures. Results have shown that mitochondria are responsible for scattering at large angles, whereas nuclei are responsible for small angle scattering.[13, 47, 50] However, the obtained one-dimensional (1D) scatter angular distribution and the lack of comparisons with more accurate simulations (*e.g.* 3D FDTD simulation of biological cells with randomly distributed organelles) limit such an understanding. The measurements of 2D light scattering in the side scatter or wide angular ranges can help to provide a better understanding of organelles in biological cells through comparisons with theoretical simulations.

1.3 Specific aims

The main goal of this project is to develop an integrated cytometer that can obtain 2D light scattering patterns from single scatterers in a microfluidic flow. By comparing the experimental results with Mie theory and FDTD simulations, we aim to achieve better understanding of the light scattering mechanism from single particles and biological cells.

This cytometer must address the many challenging issues in current light scattering research field such as single particle manipulations, light sources, detectors, and wide angle 2D light scattering measurements. Since theoretical simulations of light scattering are important to validate the experimental measurements, the integrated cytometer will be specifically designed to simplify the light scattering simulations of this apparatus.

The correct operation of this integrated cytometer will be validated by comparing light scattering experimental results with analytical simulations. Specifically Mie theory is used to confirm the light scattering measurements that are obtained with different sizes of polystyrene beads in the developed cytometer.

The FDTD code will be applied to simulate light scattering in the integrated cytometer from inhomogeneous scatterers that can not be described using analytical Mie theory predictions. The application of the FDTD code must address the challenging of transforming the far field scattered intensity onto a plane surface 2D CCD detector.

Light scattering experimental measurements on biological cells will be performed with the integrated cytometer. The experimental data will be compared to FDTD simulations for better understanding of light scattering mechanism from biological cells. The contributions on the light scattering patterns from different cellular components will be studied.

The light scattering technique has the potential to differentiate diseased cells from normal cells. The mitochondrial distribution effects on the light scattering

patterns will be studied for the differentiation between normal cell models and cancerous cell models.

1.4 References

1. G. M. Cooper and R. E. Hausman, *The cell: A molecular approach*, (AMS Press, Washington, 2004).

2. E. Hecht, *Optics*, (Addison Wesley Longman, Inc., Reading, 2002).

3. D. B. Williams and C. B. Carter, *Transmission electron microscopy: A textbook for materials science*, (Plenum Press, New York, 1996).

4. A. Wax, C. H. Yang, V. Backman, K. Badizadegan, C. W. Boone, R. R. Dasari and M. S. Feld, "Cellular organization and substructure measured using angle-resolved low-coherence interferometry," *Biophysical Journal* **82**, 2256-2264 (2002).

5. M. Chalfie, Y. Tu, G. Euskirchen, W. W. Ward and D. C. Prasher, "Green Fluorescent Protein as a Marker for Gene-Expression," *Science* **263**, 802-805 (1994).

6. R. M. Dickson, A. B. Cubitt, R. Y. Tsien and W. E. Moerner, "On/off blinking and switching behaviour of single molecules of green fluorescent protein," *Nature* **388**, 355-358 (1997).

7. L. A. Herzenberg, D. Parks, B. Sahaf, O. Perez and M. Roederer, "The history and future of the fluorescence activated cell sorter and flow cytometry: A view from Stanford," *Clinical* Chemistry **48**, 1819-1827 (2002).

8. A. Keppler, H. Pick, C. Arrivoli, H. Vogel and K. Johnsson, "Labeling of fusion proteins with synthetic fluorophores in live cells," *Proceedings of the National Academy of Sciences of the United States of America* **101**, 9955-9959 (2004).

9. M. Nirmal, B. O. Dabbousi, M. G. Bawendi, J. J. Macklin, J. K. Trautman, T. D. Harris and L. E. Brus, "Fluorescence intermittency in single cadmium selenide nanocrystals," *Nature* **383**, 802-804 (1996).

10. W. C. W. Chan and S. M. Nie, "Quantum dot bioconjugates for ultrasensitive nonisotopic detection," *Science* **281**, 2016-2018 (1998).

11. L. Cognet, C. Tardin, D. Boyer, D. Choquet, P. Tamarat and B. Lounis, "Single metallic nanoparticle imaging for protein detection in cells," *Proceedings of the National Academy of Sciences of the United States of America* **100**, 11350-11355 (2003).

12. D. Boyer, P. Tamarat, A. Maali, B. Lounis and M. Orrit, "Photothermal imaging of nanometer-sized metal particles among scatterers," *Science* **297**, 1160-1163 (2002).

13. J. R. Mourant, J. P. Freyer, A. H. Hielscher, A. A. Eick, D. Shen and T. M. Johnson, "Mechanisms of light scattering from biological cells relevant to noninvasive optical-tissue diagnostics," *Applied Optics* **37**, 3586-3593 (1998).

14. L. T. Perelman, V. Backman, M. Wallace, G. Zonios, R. Manoharan, A. Nusrat, S. Shields, M. Seiler, C. Lima, T. Hamano, I. Itzkan, J. Van Dam, J. M. Crawford and M. S. Feld, "Observation of periodic fine structure in reflectance from biological tissue: A new technique for measuring nuclear size distribution," *Physical Review Letters* **80**, 627-630 (1998).

15. R. S. Gurjar, V. Backman, L. T. Perelman, I. Georgakoudi, K. Badizadegan, I. Itzkan, R. R. Dasari and M. S. Feld, "Imaging human epithelial properties with polarized light-scattering spectroscopy," *Nature Medicine* **7**, 1245-1248 (2001).

16. T. Horio and H. Hotani, "Visualization of the Dynamic Instability of Individual Microtubules by Dark-Field Microscopy," *Nature* **321**, 605-607 (1986).

17. K. Carlsson and N. Aslund, "Confocal Imaging for 3-D Digital Microscopy," *Applied Optics* **26**, 3232-3238 (1987).

18. A. Hernandezcruz, F. Sala and P. R. Adams, "Subcellular Calcium Transients Visualized by Confocal Microscopy in a Voltage-Clamped Vertebrate Neuron," *Science* **247**, 858-862 (1990).

19. S. M. Nie, D. T. Chiu and R. N. Zare, "Probing Individual Molecules with Confocal Fluorescence Microscopy," *Science* **266**, 1018-1021 (1994).

20. D. Huang, E. A. Swanson, C. P. Lin, J. S. Schuman, W. G. Stinson, W. Chang, M. R. Hee, T. Flotte, K. Gregory, C. A. Puliafito and J. G. Fujimoto, "Optical Coherence Tomography," *Science* **254**, 1178-1181 (1991).

21. S. A. Boppart, B. E. Bouma, C. Pitris, J. F. Southern, M. E. Brezinski and J. G. Fujimoto, "In vivo cellular optical coherence tomography imaging," *Nature Medicine* **4**, 861-865 (1998).

22. H. M. Shapiro, *Practical flow cytometry*, (John Wiley & Sons, Inc., Hoboken, 2003).

23. M. Koch, A. Evans and A. Brunnschweiler, *Microfluidic technology and applications*, (Research Studies Press Ltd., Philadelphia, 2000).

24. G. Durack and J. P. Robinson, *Emerging tools for single cell analysis: advances in optical measurement technology*, (Wiley-Liss, Inc., New York, 2000).

25. H. Andersson and A. van den Berg, "Microfluidic devices for cellomics: a review," *Sensors and Actuators B-Chemical* **92**, 315-325 (2003).

26. H. Andersson and A. van den Berg, "Microfabrication and microfluidics for tissue engineering: state of the art and future opportunities," *Lab on a Chip* **4**, 98-103 (2004).

27. H. Craighead, "Future lab-on-a-chip technologies for interrogating individual molecules," *Nature* **442**, 387-393 (2006).

28. Z. Wang, J. El-Ali, M. Engelund, T. Gotsaed, I. R. Perch-Nielsen, K. B. Mogensen, D. Snakenborg, J. P. Kutter and A. Wolff, "Measurements of scattered light on a microchip flow cytometer with integrated polymer based optical elements," *Lab on a Chip* **4**, 372-377 (2004).

29. R. Drezek, M. Guillaud, T. Collier, I. Boiko, A. Malpica, C. Macaulay, M. Follen and R. Richards-Kortum, "Light scattering from cervical cells throughout neoplastic progression: influence of nuclear morphology, DNA content, and chromatin texture," *Journal of Biomedical Optics* **8**, 7-16 (2003).

30. S. Desagher and J. C. Martinou, "Mitochondria as the central control point of apoptosis," *Trends in Cell Biology* **10**, 369-377 (2000).

31. P. A. Trimmer, R. H. Swerdlow, J. K. Parks, P. Keeney, J. P. Bennett, S. W. Miller, R. E. Davis and W. D. Parker, "Abnormal mitochondrial morphology in sporadic Parkinson's and Alzheimer's disease cybrid cell lines," *Experimental Neurology* **162**, 37-50 (2000).

32. B. Albertas, D. Bray, J. Levis, K. Raff, K. Roberts and J. D. Watson, *Molecular biology of the cell*, (Garland, New York, 1994).

33. J. Beuthan, O. Minet, J. Helfmann, M. Herrig and G. Muller, "The spatial variation of the refractive index in biological cells," *Physics in Medicine and Biology* **41**, 369-382 (1996).

34. A. Brunstin and P. F. Mullaney, "Differential Light-Scattering from Spherical Mammalian-Cells," *Biophysical Journal* **14**, 439-453 (1974).

35. H. L. Liu, B. Beauvoit, M. Kimura and B. Chance, "Dependence of tissue optical properties on solute-induced changes in refractive index and osmolarity," *Journal of Biomedical Optics* **1**, 200-211 (1996).

36. P. R. Pryor, B. M. Mullock, N. A. Bright, S. R. Gray and J. P. Luzio, "The role of intraorganellar Ca2+ in late endosome-lysosome heterotypic fusion and in the reformation of lysosomes from hybrid organelles," *Journal of Cell Biology* **149**, 1053-1062 (2000).

37. G. Mie, "Articles on the optical characteristics of turbid tubes, especially colloidal metal solutions," *Annalen Der Physik* **25**, 377-445 (1908).

38. C. F. Bohren and D. R. Huffman, *Absorption and scattering of light by small particles*, (John Wiley & Sons, Inc., New York, 1983).

39. W. T. Grandy, *Scattering of Waves from Large Spheres*, (Cambridge University Press, Cambridge, 2000).

40. S. Stoylov and M. Stoimenova, "Anisotropy of Optical Polarizability in Rayleigh-Debye-Gans Approximation," *Journal of Colloid and Interface Science* **59**, 179-180 (1977).

41. L. I. Schiff, "Approximation Method for High-Energy Potential Scattering," *Physical Review* **103**, 443-453 (1956).

42. J. D. Klett and R. A. Sutherland, "Approximate Methods for Modeling the Scattering Properties of Nonspherical Particles - Evaluation of the Wentzel-Kramers-Brillouin Method," *Applied Optics* **31**, 373-386 (1992).

43. P. C. Waterman, "Matrix Formulation of Electromagnetic Scattering," *Proceedings of the Institute of Electrical and Electronics Engineers* **53**, 805-811 (1965).

44. P. Barber and C. Yeh, "Scattering of Electromagnetic-Waves by Arbitrarily Shaped Dielectric Bodies," *Applied Optics* **14**, 2864-2872 (1975).

45. E. M. Purcell and C. R. Pennypacker, "Scattering and Absorption of Light by Nonspherical Dielectric Grains," *Astrophysical Journal* **186**, 705-714 (1973).

46. S. B. Singham and C. F. Bohren, "Light-Scattering by an Arbitrary Particle - a Physical Reformulation of the Coupled Dipole Method," *Optics Letters* **12**, 10-12 (1987).

47. A. Dunn and R. Richards-Kortum, "Three-dimensional computation of light scattering from cells," *IEEE Journal of Selected Topics in Quantum Electronics* **2**, 898-905 (1996).

48. A. Taflove, *Computational electrodynamics: the finite-difference time-domain method*, (Artech House Inc., Boston, 1995).

49. R. Drezek, A. Dunn and R. Richards-Kortum, "A pulsed finite-difference time-domain (FDTD) method for calculating light scattering from biological cells over broad wavelength ranges," *Optics Express* **6**, 147-157 (2000).

50. C. G. Liu, C. Capjack and W. Rozmus, "3-D simulation of light scattering from biological cells and cell differentiation," *Journal of Biomedical Optics* **10**, 014007 (2005).

51. J. Q. Lu, P. Yang and X. H. Hu, "Simulations of light scattering from a biconcave red blood cell using the finite-difference time-domain method," *Journal of Biomedical Optics* **10**, 024022 (2005).

52. V. Backman, V. Gopal, M. Kalashnikov, K. Badizadegan, R. Gurjar, A. Wax, I. Georgakoudi, M. Mueller, C. W. Boone, R. R. Dasari and M. S. Feld,

"Measuring cellular structure at submicrometer scale with light scattering spectroscopy," *IEEE Journal of Selected Topics in Quantum Electronics* **7**, 887-893 (2001).

53. R. Drezek, A. Dunn and R. Richards-Kortum, "Light scattering from cells: finite-difference time-domain simulations and goniometric measurements," *Applied Optics* **38**, 3651-3661 (1999).

Chapter 2

Light scattering study from Mie theory to FDTD

2.1 Introduction

The physical origin of light scattering can be envisioned in a macroscopic approach as the incident fields inducing electric and magnetic multipoles that oscillate, and hence radiate in all directions, producing a "scattered" wave. In terms of the index of refraction, light scattering occurs when there is a spatial variation of the index of refraction that is seen by the propagating light. Analytical or numerical approaches can be used to solve Maxwell's Equations to obtain a solution to light scattering problems.

Mie theory gives the exact analytical solution for light scattering from a homogeneous isotropic spherical scatterer excited by an incident plane wave.[1-3] Mie simulation has been compared with the measured scattered light from a spherical bead.[4, 5] Mie theory is also often used as an approximation for the light scattering from biological cells.[4, 6] Recently, Mie theory has been used to obtain nucleus size information in tissue.[7, 8] However, due to the complex inner structure of a biological cell, there are no convincing experiments that have shown that Mie theory can be used to accurately predict single cell light scattering measurements.

The FDTD method can be used to obtain accurate numerical solutions of light scattering from biological cells.[9-13] Owing to advancements in computational

technology, the FDTD technique can be used to perform studies of light scattering with a space step of nanometers. Researchers have performed FDTD simulations on various biological cell modes, and the effects of organelles on the light scattering spectra have been studied.[9, 10, 12] Mie theory has been used for the validation of these FDTD codes.[9-11]

A numerical simulation code named "AETHER" has been developed in our group to perform FDTD simulations of light scattering from biological cells.[10] The validation of AETHER by using Mie theory results is performed over the full polar angle range and the small scatterer size cases in this chapter. The code that was used to perform Mie theory simulations is validated by published data from other groups over the full angle range. Due to the fundamental importance of Mie theory and the FDTD method in light scattering studies, brief overviews of their theoretical backgrounds are introduced in chapter 2. The computational considerations of FDTD method are also discussed.

2.2 Mie theory

2.2.1 Theoretical background of Mie theory

In a homogeneous, isotropic media, the time-harmonic plane waves satisfy the source-free Maxwell's Equations:

$$\nabla \cdot \vec{E} = 0 \tag{2.1a}$$

$$\nabla \cdot \vec{H} = 0 \tag{2.1b}$$

$$\nabla \times \vec{E} = i\omega\mu\vec{H} \tag{2.1c}$$

$$\nabla \times \vec{H} = -i\omega\varepsilon\vec{E}, \tag{2.1d}$$

where ω is the angular frequency, μ is the permeability, and ε is the permittivity. In this study of light scattering from a single scatterer (section 2.2), the field inside the scatterer is denoted by ($\vec{E}_1$, $\vec{H}_1$). The total field in the medium surrounding the scatterer is denoted by ($\vec{E}_2$, $\vec{H}_2$), which is the superposition of the incident field ($\vec{E}_i$, $\vec{H}_i$) and the scattered field ($\vec{E}_s$, $\vec{H}_s$), where

$\vec{E}_i = \vec{E}_0 \exp(i\vec{k}\cdot\vec{z} - i\omega t)$, $\vec{H}_i = \vec{H}_0 \exp(i\vec{k}\cdot\vec{z} - i\omega t)$, and $\vec{k}$ is the wave propagation vector, and $k^2 = \omega^2 \varepsilon\mu$.

The light scattering geometry is shown in Fig. 2.1 where $\vec{k}_i$ and $\vec{k}_s$ define the scattering plane. If the incident wave has a polarization that is either perpendicular or parallel to this plane, so does the scattered wave.[1] The relationship between the incident and scattered fields is conveniently written in a matrix form. For spherically symmetric scatterers,

$$\begin{pmatrix} \vec{E}_{\|s} \\ \vec{E}_{\perp s} \end{pmatrix} = \frac{e^{ik(r-z)}}{-ikr} \begin{pmatrix} S_2 & 0 \\ 0 & S_1 \end{pmatrix} \begin{pmatrix} \vec{E}_{\|i} \\ \vec{E}_{\perp i} \end{pmatrix}, \tag{2.2}$$

where S_1 and S_2 are the elements of the scattering amplitude matrix, $\|$ denotes the polarization parallel to the scattering plane, and $\perp$ denotes the polarization perpendicular to the scattering plane. If I_i is the incident flux, the scattered fluxes in terms of the different polarizations are,

$$I_{s1} = \frac{i_1}{k^2 r^2} I_i \tag{2.3a}$$

$$I_{s2} = \frac{i_2}{k^2 r^2} I_i \tag{2.3b}$$

$$I_s = \frac{i_1 + i_2}{2k^2 r^2} I_i . \tag{2.3c}$$

Here (2.3a) is for a perpendicular polarized incident beam, (2.3b) is for a parallel polarized incident beam, and (2.3c) is for an unpolarized incident beam. The scattered polarized intensities for perpendicular and parallel polarization are defined by $i_1 = |S_1|^2$ and $i_2 = |S_2|^2$, respectively. The objective of the analysis that follows is to give analytical solutions for S_1 and S_2.

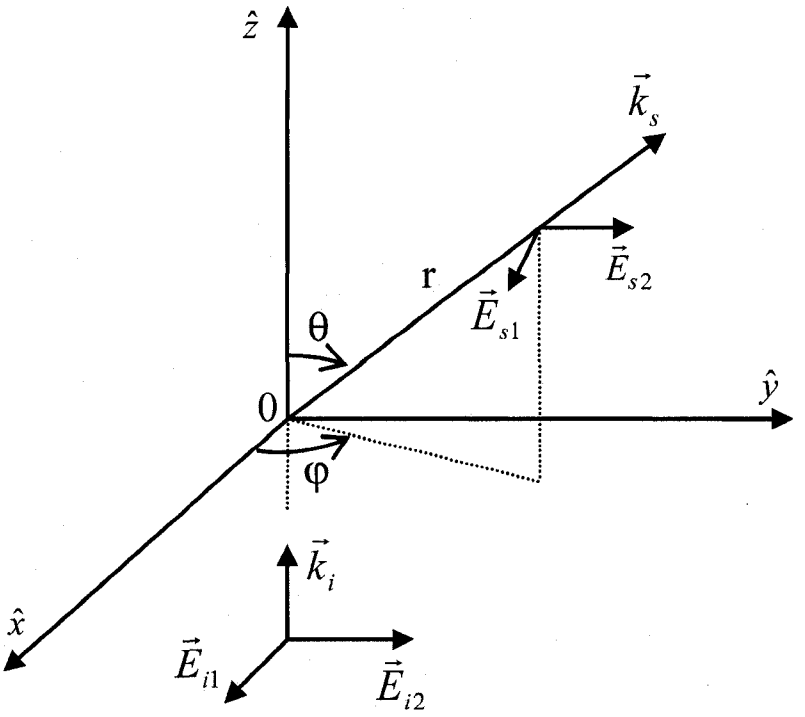

Figure 2.1 Light scattering geometry for a single scatterer. The incident wave propagates along the $+z$ direction, the scattered wave has a polar angle θ and an azimuth angle φ as shown in the figure. (r,θ,φ) defines the spherical coordinates. The spherical scatterer with a radius a is centered at the origin.

The time-harmonic electromagnetic field $(\vec{E},\vec{H})$ in a linear, isotropic, homogenerous medium satisfies the wave equations,

$$\nabla^2\vec{E}+k^2\vec{E}=0 \tag{2.4a}$$

$$\nabla^2\vec{H}+k^2\vec{H}=0\,. \tag{2.4b}$$

We define two vector functions in spherical polar coordinates,[3]

$$\vec{M}=\nabla\times(\vec{r}\psi) \tag{2.5a}$$

$$\vec{N}=\frac{\nabla\times\vec{M}}{k}\,. \tag{2.5b}$$

$\vec{M}$ and $\vec{N}$ satisfy the wave equations (2.4) and have all the required properties of an electromagnetic field. The scalar wave equation in spherical polar coordinates is,

$$\frac{1}{r^2}\frac{\partial}{\partial r}(r^2\frac{\partial \psi}{\partial r})+\frac{1}{r^2\sin\theta}\frac{\partial}{\partial \theta}(\sin\theta\frac{\partial \psi}{\partial \theta})+\frac{1}{r^2\sin\theta}\frac{\partial^2 \psi}{\partial \varphi^2}+k^2\psi=0. \quad (2.6)$$

By separation of variables, $\psi(r,\theta,\varphi)=R(r)\Theta(\theta)\Phi(\varphi)$, the solutions for (2.6) can be constructed as

$$\psi_{emn}=\cos(m\varphi)P_n^m(\cos\theta)z_n(kr) \quad (2.7a)$$

$$\psi_{omn}=\sin(m\varphi)P_n^m(\cos\theta)z_n(kr), \quad (2.7b)$$

where subscripts e and o denote even and odd numbers, $m=0,1,2,\cdots$, $n=m,m+1,\cdots$. $\sin(m\varphi)$ and $\cos(m\varphi)$ are the azimuth functions, $P_n^m(\cos\theta)$ are the associated Legendre functions as solutions to $\Theta(\theta)$, and $z_n(kr)$ is any of the four spherical Bessel functions as solutions to $R(r)$:

$$j_n(\rho)=\sqrt{\frac{\pi}{2\rho}}J_{n+1/2}(\rho) \quad (2.8a)$$

$$n_n(\rho)=\sqrt{\frac{\pi}{2\rho}}N_{n+1/2}(\rho) \quad (2.8b)$$

$$h_n^{(1)}=j_n(\rho)+in_n(\rho) \quad (2.8c)$$

$$h_n^{(2)}=j_n(\rho)-in_n(\rho), \quad (2.8d)$$

where $\rho=kr$. Equations (2.8c and 2.8d) are the spherical Bessel functions of the third kind (spherical Hankel functions). Now the vector spherical harmonics generated by ψ_{emn} and ψ_{omn} can be given as

$$\vec{M}_{emn}=\nabla\times(\vec{r}\psi_{emn}),\ \vec{M}_{omn}=\nabla\times(\vec{r}\psi_{omn}) \quad (2.9a)$$

$$N_{emn}=\frac{\nabla\times\vec{M}_{emn}}{k},\ N_{omn}=\frac{\nabla\times\vec{M}_{omn}}{k}. \quad (2.9b)$$

From now on, superscripts will be appended to the functions $\vec{M}$ and $\vec{N}$ to denote the kind of spherical Bessel function z_n as ordered in Equation 2.8. For example, (1) denotes $j_n(\rho)$, and (3) denotes $h_n^{(1)}(\rho)$.

A plane wave can be expanded in vector spherical harmonics as

$$\vec{E}_i=E_0\sum_{n=1}^{\infty}i^n\frac{2n+1}{n(n+1)}(\vec{M}_{o1n}^{(1)}-i\vec{N}_{e1n}^{(1)}). \quad (2.10)$$

The corresponding incident magnetic field is obtained from the curl of (2.10),

$$\vec{H}_i = \frac{-k}{\omega\mu} E_0 \sum_{n=1}^{\infty} i^n \frac{2n+1}{n(n+1)} (\vec{M}_{o1n}^{(1)} + i\vec{N}_{e1n}^{(1)}) . \tag{2.11}$$

Thus, expansion of the field $(\vec{E}_1, \vec{H}_1)$ can be given as

$$\vec{E}_1 = E_0 \sum_{n=1}^{\infty} i^n \frac{2n+1}{n(n+1)} (c_n \vec{M}_{o1n}^{(1)} - id_n \vec{N}_{e1n}^{(1)}) \tag{2.12a}$$

$$\vec{H}_1 = \frac{-k_1}{\omega\mu_1} E_0 \sum_{n=1}^{\infty} i^n \frac{2n+1}{n(n+1)} (d_n \vec{M}_{o1n}^{(1)} + ic_n \vec{N}_{e1n}^{(1)}) . \tag{2.12b}$$

Similarly, the expansion of the scattered field is given by

$$\vec{E}_s = E_0 \sum_{n=1}^{\infty} i^n \frac{2n+1}{n(n+1)} (ia_n \vec{N}_{e1n}^{(3)} - ib_n \vec{M}_{o1n}^{(3)}) \tag{2.13a}$$

$$\vec{H}_s = \frac{k}{\omega\mu} E_0 \sum_{n=1}^{\infty} i^n \frac{2n+1}{n(n+1)} (ib_n \vec{N}_{e1n}^{(3)} + a_n \vec{M}_{o1n}^{(3)}) . \tag{2.13b}$$

It is convenient to define the angle dependent functions,

$$\pi_n = \frac{P_n^1}{\sin\theta}, \quad \tau_n = \frac{dP_n^1}{d\theta} . \tag{2.14}$$

We can write the vector spherical harmonics (2.9) (with $m = 1$) in the expansions of the internal field (2.12) and the scattered field (2.13) in a concise form,

$$\vec{M}_{o1n} = \cos(\varphi)\pi_n(\cos\theta) z_n(\rho)\hat{\theta} - \sin(\varphi)\tau_n(\cos\theta) z_n(\rho)\hat{\varphi} \tag{2.15a}$$

$$\vec{M}_{e1n} = -\sin(\varphi)\pi_n(\cos\theta) z_n(\rho)\hat{\theta} - \cos(\varphi)\tau_n(\cos\theta) z_n(\rho)\hat{\varphi} \tag{2.15b}$$

$$\vec{N}_{o1n} = \sin(\varphi) n(n+1) \sin\theta \pi_n(\cos\theta) \frac{z_n(\rho)}{\rho} \hat{r} + \sin(\varphi)\tau_n(\cos\theta) \frac{[\rho z_n(\rho)]'}{\rho} \hat{\theta}$$

$$+ \cos(\varphi)\pi_n(\cos\theta) \frac{[\rho z_n(\rho)]'}{\rho} \hat{\varphi} \tag{2.15c}$$

$$\vec{N}_{e1n} = \cos(\varphi) n(n+1) \sin\theta \pi_n(\cos\theta) \frac{z_n(\rho)}{\rho} \hat{r} + \cos(\varphi)\tau_n(\cos\theta) \frac{[\rho z_n(\rho)]'}{\rho} \hat{\theta}$$

$$- \sin(\varphi)\pi_n(\cos\theta) \frac{[\rho z_n(\rho)]'}{\rho} \hat{\varphi} . \tag{2.15d}$$

We now address how various observable quantities vary with the size and optical properties of the scatterer and the surrounding medium. In order to do so we need to obtain expressions for the scattering coefficients a_n and b_n, and the coefficients c_n and d_n for the inner field. These coefficients are obtained from the boundary conditions at $r = a$, where the tangential components are continuous,

$$E_{i\theta} + E_{s\theta} = E_{1\theta}\,,\ E_{i\varphi} + E_{s\varphi} = E_{1\varphi} \tag{2.16a}$$

$$H_{i\theta} + H_{s\theta} = H_{1\theta}\,,\ H_{i\varphi} + H_{s\varphi} = H_{1\varphi}\,. \tag{2.16b}$$

Solving the boundary conditions (2.16) gives the internal coefficients,

$$c_n = \frac{\mu_1 j_n(x)\left[xh_n^{(1)}(x)\right]' - \mu_1 h_n^{(1)}(x)\left[xj_n(x)\right]'}{\mu_1 j_n(mx)\left[xh_n^{(1)}(x)\right]' - \mu h_n^{(1)}(x)\left[mxj_n(mx)\right]'} \tag{2.17a}$$

$$d_n = \frac{\mu_1 m j_n(x)\left[xh_n^{(1)}(x)\right]' - \mu_1 m h_n^{(1)}(x)\left[xj_n(x)\right]'}{\mu m^2 j_n(mx)\left[xh_n^{(1)}(x)\right]' - \mu_1 h_n^{(1)}(x)\left[mxj_n(mx)\right]'}\,, \tag{2.17b}$$

and the scattering coefficients,

$$a_n = \frac{\mu m^2 j_n(mx)\left[xj_n(x)\right]' - \mu_1 j_n(x)\left[mxj_n(mx)\right]'}{\mu m^2 j_n(mx)\left[xh_n^{(1)}(x)\right]' - \mu_1 h_n^{(1)}(x)\left[mxj_n(mx)\right]'} \tag{2.18a}$$

$$b_n = \frac{\mu_1 j_n(mx)\left[xj_n(x)\right]' - \mu j_n(x)\left[mxj_n(mx)\right]'}{\mu_1 j_n(mx)\left[xh_n^{(1)}(x)\right]' - \mu h_n^{(1)}(x)\left[mxj_n(mx)\right]'}\,, \tag{2.18b}$$

where x is the size parameter and m is the relative refractive index. $x = ka = \frac{2\pi Na}{\lambda}$, $m = \frac{k_1}{k} = \frac{N_1}{N}$, where N_1 and N are the refractive indices of the scatterer and the surrounding medium, respectively. The incident wavelength in vacuum is given by λ. The scattering coefficients (2.18) can be simplified by introducing the Riccati-Bessel functions,

$$\eta(\rho) = \rho j_n(\rho)\,,\ \xi(\rho) = \rho h_n^{(1)}(\rho)\,.$$

If we take the permeability of the scatterer and the surrounding medium to be the same, then

$$a_n = \frac{m\eta_n(mx)\eta_n'(x) - \eta_n(x)\eta_n'(mx)}{m\eta_n(mx)\xi_n'(x) - \xi_n(x)\eta_n'(mx)} \tag{2.19a}$$

$$b_n = \frac{\eta_n(mx)\eta_n'(x) - m\eta_n(x)\eta_n'(mx)}{\eta_n(mx)\xi_n'(x) - m\xi_n(x)\eta_n'(mx)}. \tag{2.19a}$$

By substituting Equations (2.15) and (2.19) into Equation 2.13, the matrix elements S_1 and S_2 can be given as

$$S_1 = \sum_n \frac{2n+1}{n(n+1)}(a_n\pi_n + b_n\tau_n) \tag{2.20a}$$

$$S_2 = \sum_n \frac{2n+1}{n(n+1)}(a_n\tau_n + b_n\pi_n), \tag{2.20b}$$

where π_n and τ_n are given by Equation 2.14.

2.2.2 Full angle validation of our Mie code

A FORTRAN code has been used in our group to perform Mie theory simulations.[10] Here this Mie code is compared with published data in the full angular range. The Mie simulated data was first normalized by I_0, the intensity at the polar angle 0 degree. A logarithm was then applied to the normalized data to show the full angle intensity variations (note the several order intensity variations), which gives an intensity of 0 at polar angle 0 degree in the logarithm scale. This normalization (by a constant) and logarithm (for better visualization) method has been widely used in wide angle 1D light scattering comparisons both in theories and experiments.[4, 5, 10-12, 14-16]

Figure 2.2 shows one example of such a comparison. The homogeneous spherical scatterer in the published article[11] has a radius of 2.655μm with a refractive index of $1.402 + i1.6804\times10^{-5}$, while the surrounding medium has a refractive index 1.35. The incident wave has a wavelength of 1μm. We perform our Mie code on the same constants, and give the comparison as shown in Fig. 2.2. In Fig. 2.2, both results are the averages of the perpendicular and parallel polarization intensity distributions in the full polar angle range of $0\sim180^0$. From

Fig. 2.2, we find that our Mie code simulation agrees well with the published result in the full polar angle range, with a maximum intensity variation around 1%.

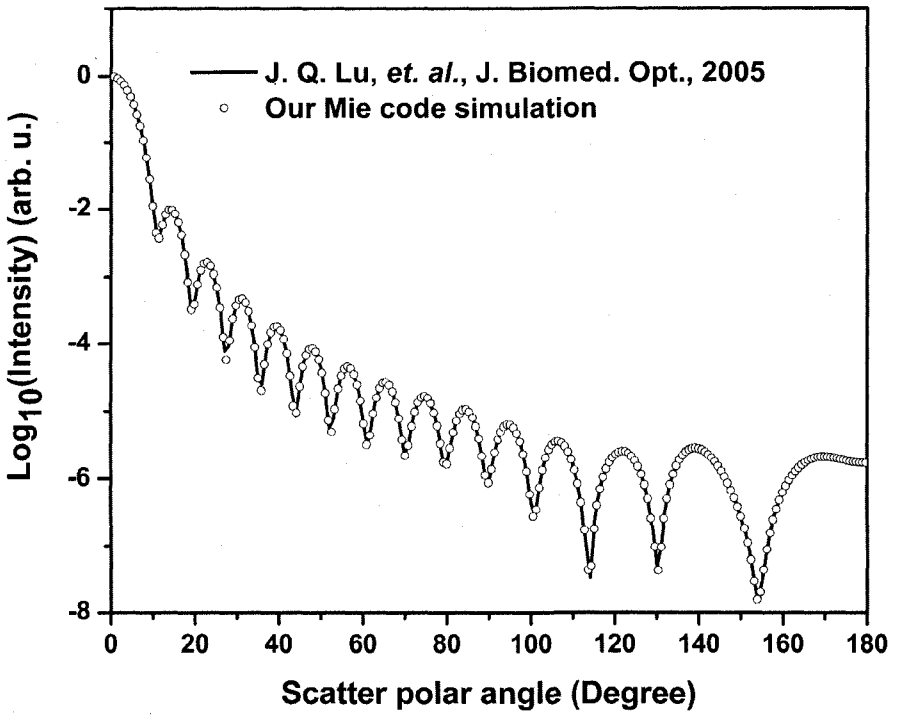

Figure 2.2 Validation of our Mie code in full angular range.

2.3 FDTD method for light scattering simulations

2.3.1 Theoretical background of FDTD light scattering simulation

2.3.1.1 Yee's algorithm

Yee's FDTD algorithm solves for both the electric and magnetic fields in time and in space by using the coupled Maxwell's curl equations rather than solving for the electric (or the magnetic) field alone.[17] The electric and magnetic components are centered in three-dimensional space so that every electric component is surrounded by four circulating magnetic components, and every magnetic component is surrounded by four circulating electric components as shown in Fig. 2.3. Continuity of the tangential electric field and magnetic field is naturally

maintained. The locations of the electric field and magnetic field components in the Yee grid and the central difference operations on these components implicitly enforce the two Maxwell's divergence equations.[18] The electric field and magnetic field are centered in time in what is termed a leapfrog arrangement.

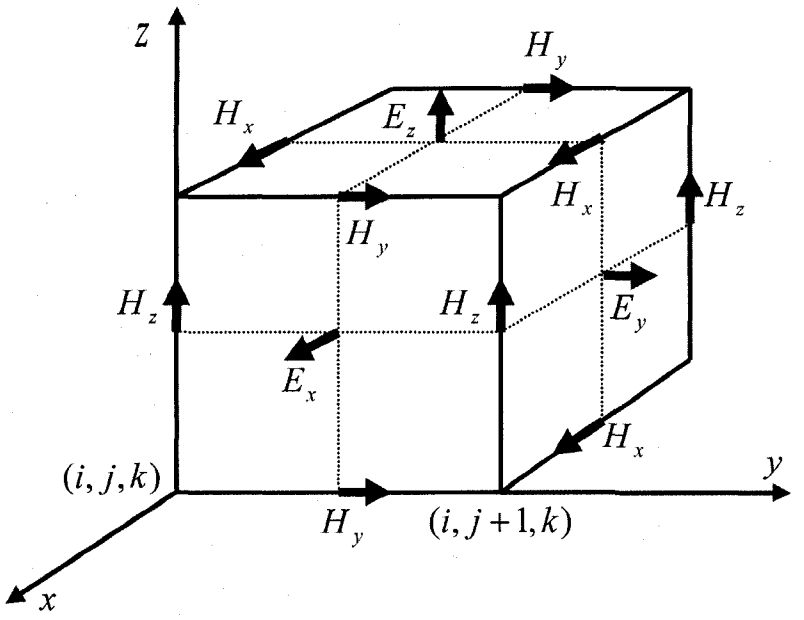

Figure 2.3 Electric and magnetic field vector components in the Yee space lattice.

The Maxwell's curl equations in a source-free medium read,

$$\frac{\partial \vec{H}}{\partial t} = -\frac{1}{\mu}\nabla \times \vec{E} \tag{2.21a}$$

$$\frac{\partial \vec{E}}{\partial t} = \frac{1}{\varepsilon}\nabla \times \vec{H}\,. \tag{2.21b}$$

In the 3D rectangular coordinate system (x, y, z), the two curl equations can be written as:

$$\frac{\partial H_x}{\partial t} = \frac{1}{\mu}\left(\frac{\partial E_y}{\partial z} - \frac{\partial E_z}{\partial y}\right) \tag{2.22a}$$

$$\frac{\partial H_y}{\partial t} = \frac{1}{\mu}\left(\frac{\partial E_z}{\partial x} - \frac{\partial E_x}{\partial z}\right) \tag{2.22b}$$

$$\frac{\partial H_z}{\partial t} = \frac{1}{\mu}\left(\frac{\partial E_x}{\partial y} - \frac{\partial E_y}{\partial x}\right) \tag{2.22c}$$

$$\frac{\partial E_x}{\partial t} = -\frac{1}{\varepsilon}\left(\frac{\partial H_y}{\partial z} - \frac{\partial H_z}{\partial y}\right) \tag{2.23a}$$

$$\frac{\partial E_y}{\partial t} = -\frac{1}{\varepsilon}\left(\frac{\partial H_z}{\partial x} - \frac{\partial H_x}{\partial z}\right) \tag{2.23b}$$

$$\frac{\partial E_z}{\partial t} = -\frac{1}{\varepsilon}\left(\frac{\partial H_x}{\partial y} - \frac{\partial H_y}{\partial x}\right). \tag{2.23c}$$

Yee defines a uniform, rectangular lattice as

$$(i, j, k) = (i\Delta x, j\Delta y, k\Delta z), \tag{2.24}$$

where Δx, Δy, and Δz are the grid spacings in x, y, and z directions, respectively. Any function u of space and time can be denoted as

$$u^n_{i,j,k} = u(i\Delta x, j\Delta y, k\Delta z, n\Delta t), \tag{2.25}$$

where Δt is the time spacing, and n is the time index. The first partial space derivative of u in the x direction (similarly in the y and z directions), at a fixed time $t_n = n\Delta t$ is given by

$$\frac{\partial u^n_{i,j,k}}{\partial x} = \frac{u^n_{i+1/2,j,k} - u^n_{i-1/2,j,k}}{\Delta x}, \tag{2.26}$$

and the first partial time derivative of u at a fixed space point (i, j, k) is,

$$\frac{\partial u^n_{i,j,k}}{\partial t} = \frac{u^{n+1/2}_{i,j,k} - u^{n-1/2}_{i,j,k}}{\Delta t}. \tag{2.27}$$

By substituting the first partial space and time derivatives of u into (2.23), and using a semi-implicit approximation (for example, $H_x|^n_{i,j,k} = \frac{H_x|^{n+1/2}_{i,j,k} + H_x|^{n-1/2}_{i,j,k}}{2}$), we obtain the six coupled explicit second-order accurate finite difference equations:

$$H_x|^{n+1/2}_{i,j,k} = H_x|^{n-1/2}_{i,j,k} + \frac{\Delta t}{\mu_{i,j,k}}\left(\frac{E_y|^n_{i,j,k+1/2} - E_y|^n_{i,j,k-1/2}}{\Delta z} - \frac{E_z|^n_{i,j+1/2,k} - E_z|^n_{i,j-1/2,k}}{\Delta y}\right) \tag{2.28a}$$

$$H_y\Big|_{i,j,k}^{n+1/2} = H_y\Big|_{i,j,k}^{n-1/2} + \frac{\Delta t}{\mu_{i,j,k}}\left(\frac{E_z\Big|_{i+1/2,j,k}^{n} - E_z\Big|_{i-1/2,j,k}^{n}}{\Delta x} - \frac{E_x\Big|_{i,j,k+1/2}^{n} - E_x\Big|_{i,j,k-1/2}^{n}}{\Delta z}\right) \quad (2.28b)$$

$$H_z\Big|_{i,j,k}^{n+1/2} = H_z\Big|_{i,j,k}^{n-1/2} + \frac{\Delta t}{\mu_{i,j,k}}\left(\frac{E_x\Big|_{i,j+1/2,k}^{n} - E_x\Big|_{i,j-1/2,k}^{n}}{\Delta y} - \frac{E_y\Big|_{i+1/2,j,k}^{n} - E_y\Big|_{i-1/2,j,k}^{n}}{\Delta x}\right) \quad (2.28c)$$

$$E_x\Big|_{i,j,k}^{n+1} = E_x\Big|_{i,j,k}^{n} + \frac{\Delta t}{\varepsilon_{i,j,k}}\left(\frac{H_z\Big|_{i,j+1/2,k}^{n+1/2} - H_z\Big|_{i,j-1/2,k}^{n+1/2}}{\Delta y} - \frac{H_y\Big|_{i,j,k+1/2}^{n+1/2} - H_y\Big|_{i,j,k-1/2}^{n+1/2}}{\Delta z}\right) \quad (2.29a)$$

$$E_y\Big|_{i,j,k}^{n+1} = E_y\Big|_{i,j,k}^{n} + \frac{\Delta t}{\varepsilon_{i,j,k}}\left(\frac{H_x\Big|_{i,j,k+1/2}^{n+1/2} - H_x\Big|_{i,j,k-1/2}^{n+1/2}}{\Delta z} - \frac{H_z\Big|_{i+1/2,j,k}^{n+1/2} - H_z\Big|_{i-1/2,j,k}^{n+1/2}}{\Delta x}\right) \quad (2.29b)$$

$$E_z\Big|_{i,j,k}^{n+1} = E_z\Big|_{i,j,k}^{n} + \frac{\Delta t}{\varepsilon_{i,j,k}}\left(\frac{H_y\Big|_{i+1/2,j,k}^{n+1/2} - H_y\Big|_{i-1/2,j,k}^{n+1/2}}{\Delta x} - \frac{H_x\Big|_{i,j+1/2,k}^{n+1/2} - H_x\Big|_{i,j-1/2,k}^{n+1/2}}{\Delta y}\right). \quad (2.29c)$$

2.3.1.2 Incident light consideration

The total-field/scattered-field (TF/SF) technique is used to apply the incident field and to compute the scatter patterns.[18] From the linearity of Maxwell's Equations, we have

$$\vec{E}_{tot} = \vec{E}_{inc} + \vec{E}_{scat} \quad (2.30a)$$

$$\vec{H}_{tot} = \vec{H}_{inc} + \vec{H}_{scat}. \quad (2.30b)$$

The total field is calculated inside the TF/SF interface (Figure 2.4). Outside the TF/SF interface, only the scattered field is calculated. Therefore, values of the incident light are required only on the TF/SF interfaces to connect the total field domain and the scattered field domain. Thus computer storage is minimized.

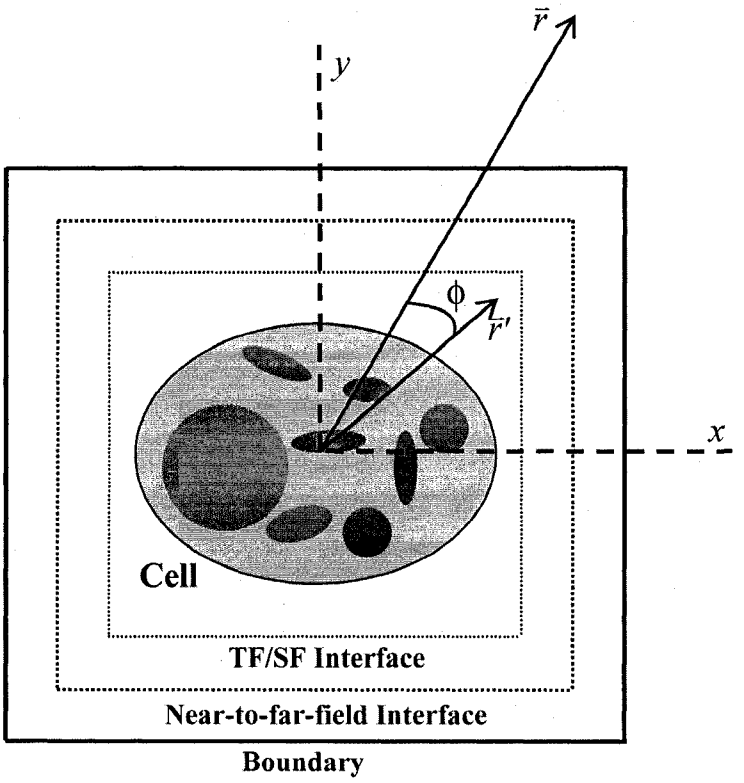

Figure 2.4 The geometry of the FDTD computational domain.

Since the incident field can be specified analytically on the TF/SF interface, the TF/SF technique allows the FDTD method to be used for arbitrary incident fields. In this work we will be interested in the interaction of laser light with the scatterer. In order to avoid high-frequency components that may be introduced by a sudden onset of the incident wave, the Hamming function is used for describing the magnitude of the startup of the incident light:[10]

$g(t) = 0$, if $t \le 0$

$g(t) = 0.5 - 0.5\cos(\pi t / \Delta T)$, if $0 \le t \le \Delta T$

$g(t) = 1$, otherwise

where ΔT denotes the startup time. In our calculation, ΔT is selected to be π / ω, where ω is the angular frequency of the incident light.

2.3.1.3 Grid consideration

While performing the FDTD simulations, the stability condition must be considered,[18]

$$\Delta t \le \frac{1}{c\sqrt{\left(\frac{1}{(\Delta x)^2}+\frac{1}{(\Delta y)^2}+\frac{1}{(\Delta z)^2}\right)}}, \tag{2.31}$$

where c is the incident light speed in vacuum, Δx, Δy and Δz are the grid spacings, and Δt is the time step size.

When the grid spacings are the same in all directions as denoted by δ, the stability condition can be simplified,

$$\frac{c\Delta t}{\delta} \le \frac{1}{\sqrt{N}}, \tag{2.32}$$

where N is the number of spatial dimensions. The grid spacing is suggested to be less than $\lambda/10$ to yield accurate results.[18] If a wavelength of 632.8nm is used, the maximum suggested grid spacing is 63.28nm. According to the stability condition in (2.32), this grid spacing gives a maximum time step of 0.122 femtosecond for a 3D problem.

2.3.1.4 Absorbing boundary conditions

FDTD computations can only be conducted in a limited spatial domain, although light actually travels in an unbounded space. Without appropriate boundary conditions, the scattered waves would be artificially reflected at the boundaries, which would lead to inaccurate results. Absorbing boundary conditions (ABCs) such as Mur boundary condition,[19] Liao boundary condition,[20] and "perfectly matched layer" (PML) boundary condition[21] have been used to suppress the spurious reflections of the outgoing numerical waves, permitting FDTD solutions to be valid for all time steps.

Mur introduced a simple and successful finite-difference scheme for the ABCs. As an example of the first-order Mur boundary condition, the E_z component at $x = 0$ can be written as

$$E_z\Big|_{0,j,k}^{n+1} = -E_z\Big|_{1,j,k}^{n-1} + \frac{c\Delta t - \delta}{c\Delta t + \delta}\left(E_z\Big|_{1,j,k}^{n+1} + E_z\Big|_{0,j,k}^{n-1}\right) + \frac{2\delta}{c\Delta t + \delta}\left(E_z\Big|_{0,j,k}^{n} + E_z\Big|_{1,j,k}^{n}\right). \quad (2.33)$$

The second-order Mur boundary condition can be used to give a more accurate result.

Liao *et al.* proposed an ABC that has a reflection coefficient (1% or less) that is approximately one order of magnitude less than that of the second-order Mur ABC. The Liao boundary condition uses a backward-difference polynomial to interpolate the filed values u_j ($j = 1,2...N$) at the boundary. Consider an outer grid boundary located at $x_{\max}$, the *mth* backward difference can be written as

$$\Delta^m u(t, x_{\max} - \alpha c\Delta t) = \sum_{j=1}^{m+1} (-1)^{j+1} C_{j-1}^m u\left[t - (j-1)\Delta t, x_{\max} - j\alpha c\Delta t\right], \quad (2.34)$$

where α is a scaling factor ($0 \le \alpha \le 2$), the coefficient C_j^m is,

$$C_j^m = \frac{m!}{(m-j)!\,j!}. \quad (2.35)$$

For example, if $\alpha = 2$, $c\Delta t = \delta/2$ and $N = 3$, the Liao boundary condition can be given as

$$u_3 = u(t - 2\Delta t, x_{\max} - 3\delta) \quad (2.36a)$$

$$u_2 = u(t - \Delta t, x_{\max} - 2\delta) \quad (2.36b)$$

$$u_1 = u(t, x_{\max} - \delta). \quad (2.36c)$$

The PML boundary condition reduces the artificial reflection at the boundary by several orders of magnitude compared with Mur and Liao ABCs. In the PML boundary condition, an artificial material region surrounding the scatterer is created which has both electrical conductivities and magnetic losses. Each field component in this region is split into two parts, resulting in a total of 12 field component in 3D. Although the PML boundary condition improves the artificial

reflection significantly, it requires larger computational storage and is more complicated to implement compared with Mur and Liao ABCs.

In this work, the Liao boundary condition is used due to its improved performance over the Mur boundary condition, and the less computational storage memory requirements as compared with the PML boundary condition.

2.3.1.5 Near-to-far-field transformation

The FDTD method computes the fields in a region around the scatterer that lies in the near field. However most light scattering measures the far field scattered light. To determine the far field scattering pattern, the near field data is transformed from time-domain to frequency-domain by using the discrete Fourier transform (DFT). The technique of equivalent electric/magnetic currents is used to calculate the scattered field at a distance by using the near field data.[18]

The radiation source inside the near-to-far-field interface can be equivalently represented by virtual electric currents $\vec{J}_s$ and magnetic currents $\vec{M}_s$, which are defined on the near-to-far-field surface (S),

$$\vec{J}_s(\vec{r}') = \hat{n} \times \vec{H}\ ,\ \vec{M}_s(\vec{r}') = -\hat{n} \times \vec{E} \tag{2.37}$$

where $\vec{r}'$ is a point on the surface, and $\hat{n}$ is a unit vector normal to S. In spherical coordinates, the far field electric and magnetic field components are given by,

$$E_r = 0 \tag{2.38a}$$

$$E_\theta = -\frac{jk\exp(-jkr)}{4\pi r}(L_\varphi + \sqrt{\frac{\mu}{\varepsilon}}N_\theta) \tag{2.38b}$$

$$E_\varphi = -\frac{jk\exp(-jkr)}{4\pi r}(L_\theta - \sqrt{\frac{\mu}{\varepsilon}}N_\varphi) \tag{2.38c}$$

$$H_r = 0 \tag{2.39a}$$

$$H_\theta = -\frac{jk\exp(-jkr)}{4\pi r}(N_\varphi - \sqrt{\frac{\varepsilon}{\mu}}L_\theta) \tag{2.39b}$$

$$H_\varphi = -\frac{jk\exp(-jkr)}{4\pi r}(N_\theta + \sqrt{\frac{\varepsilon}{\mu}}L_\varphi) \tag{2.39c}$$

where k is the wave propagation number, and scalar r is a point in the far field. The vector potentials $\vec{N}$ and $\vec{L}$ are defined as,

$$\vec{N} = \iint_S (\hat{x}J_x + \hat{y}J_y + \hat{z}J_z)\exp(jkr'\cos\Phi)dS' \tag{2.40a}$$

$$\vec{L} = \iint_S (\hat{x}M_x + \hat{y}M_y + \hat{z}M_z)\exp(jkr'\cos\Phi)dS' \tag{2.40b}$$

where Φ is the angle between the equivalent near field source point r' and the far field point r (Fig. 2.4), and $r'\cos\Phi = x'\sin\theta\cos\varphi + y'\sin\theta\sin\varphi + z'\cos\theta$. Once the scattered field components are known, all quantities about the far field light scattering can be described. For example, the far field scattered light intensity can be given as,

$$I(\theta,\varphi) = \frac{1}{2}\mathrm{Re}(E_\theta H_\varphi^*) + \frac{1}{2}\mathrm{Re}(-E_\varphi H_\theta^*) \tag{2.41}$$

2.3.1.6 Computational considerations

In this work, the scatterer is modeled by assigning values of ε and μ at different positions. The FDTD method is implemented in a FORTRAN 90 code running on Silicon Graphics Inc. (SGI) parallel computers.

The memory requirement of a program depends on the size of its important arrays. In the AETHER FDTD code, we declare 8 arrays of double precision type, 6 for the field components and 2 for ε and μ, each with approximate dimensions (n_x, n_y, n_z). As such, the memory needed for these arrays would be the product of,

$n_x \times n_y \times n_z$ ... number of elements in each array,

8..... size (in bytes) of one array element, and

8..... number of arrays.

For the simulation of a 10μm cell in radius, if the grid spacing is chosen to be 20nm, the program would require about 64GB of memory.

2.3.2 Validation of our FDTD code

2.3.2.1 Full angle validation of our FDTD code

The validation of the AETHER FDTD code was performed by comparing the FDTD results with Mie simulation results. FDTD and Mie simulations for a spherical cell of size 1.5μm (radius) with a refractive index 1.3 are performed. The surrounding medium is assumed to have a refractive index 1.0, and the incident wavelength λ is assumed to be 0.6328μm. For the FDTD simulation, a space step of $\lambda/20$ is used. Figure 2.5 shows the perpendicular polarization results from both the FDTD and Mie simulations. The FDTD results agree well with the Mie results especially in the angular range from 0 to 10 degrees, with a maximum intensity variation around 3%. The larger difference caused in backward scatter angular range (160 to 180 degrees) is mainly due to the artificial reflections.[10]

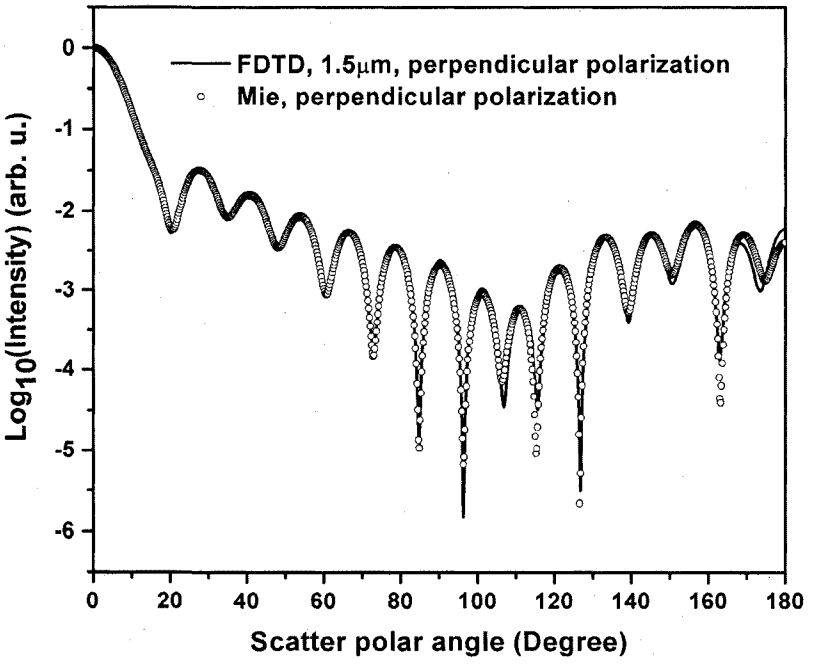

Figure 2.5 Full angle validation of our AETHER FDTD code.

2.3.2.2 Small size validation of our FDTD code

The characterization of organelle information in biological cells is of great interest in FDTD light scattering simulations. The organelles in a biological cell have size variations from nano scale to micro scale. The accuracy of FDTD method when applied to nano scale cases is validated in Fig. 2.6. The assumed spherical organelle has a radius of 250nm, and a refractive index 1.38. The surrounding medium has a refractive index 1.334. The wavelength of the incident laser illumination is 632.8nm. As shown in Fig. 2.6, our AETHER FDTD simulation for a nano scale organelle agrees well with the Mie theory simulation over the full polar angle range of $0\sim180^0$, with a maximum intensity variation around 6%.

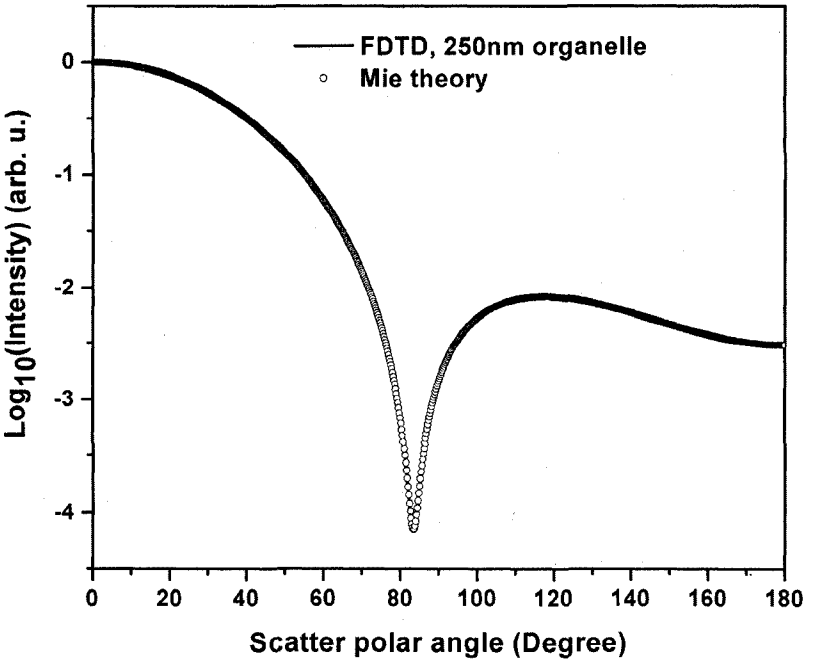

Figure 2.6 Small organelle size validation of our FDTD code.

2.4 Conclusions

Codes have been developed by our group for implementing Mie theory predictions and the FDTD method for light scattering studies. The Mie code can

be used to give analytical solutions for spherical scatterers, while the AETHER FDTD code can be used for numerical solutions of light scattering involving complex biological cells. Validation of Mie code was performed over the full angular range by comparing results with published data from other groups. The good agreement between FDTD and Mie simulation results over the full angular range and for small organelle sizes shows the promise of the use of AETHER for predicting light scattering from biological cells.

2.5 References

1. W. T. Grandy, *Scattering of Waves from Large Spheres*, (Cambridge University Press, Cambridge, 2000).

2. G. Mie, "Articles on the optical characteristics of turbid tubes, especially colloidal metal solutions," *Annalen Der Physik* **25**, 377-445 (1908).

3. C. F. Bohren and D. R. Huffman, *Absorption and scattering of light by small particles*, (John Wiley & Sons, Inc., New York, 1983).

4. J. R. Mourant, J. P. Freyer, A. H. Hielscher, A. A. Eick, D. Shen and T. M. Johnson, "Mechanisms of light scattering from biological cells relevant to noninvasive optical-tissue diagnostics," *Applied Optics* **37**, 3586-3593 (1998).

5. D. Watson, N. Hagen, J. Diver, P. Marchand and M. Chachisvilis, "Elastic light scattering from single cells: Orientational dynamics in optical trap," *Biophysical Journal* **87**, 1298-1306 (2004).

6. J. Neukammer, C. Gohlke, A. Hope, T. Wessel and H. Rinneberg, "Angular distribution of light scattered by single biological cells and oriented particle agglomerates," *Applied Optics* **42**, 6388-6397 (2003).

7. L. T. Perelman, V. Backman, M. Wallace, G. Zonios, R. Manoharan, A. Nusrat, S. Shields, M. Seiler, C. Lima, T. Hamano, I. Itzkan, J. Van Dam, J. M. Crawford and M. S. Feld, "Observation of periodic fine structure in reflectance from biological tissue: A new technique for measuring nuclear size distribution," *Physical Review Letters* **80**, 627-630 (1998).

8. A. Wax, C. H. Yang, V. Backman, K. Badizadegan, C. W. Boone, R. R. Dasari and M. S. Feld, "Cellular organization and substructure measured using angle-resolved low-coherence interferometry," *Biophysical Journal* **82**, 2256-2264 (2002).

9. A. Dunn and R. Richards-Kortum, "Three-dimensional computation of light scattering from cells," *IEEE Journal of Selected Topics in Quantum Electronics* **2**, 898-905 (1996).

10. C. G. Liu, C. Capjack and W. Rozmus, "3-D simulation of light scattering from biological cells and cell differentiation," *Journal of Biomedical Optics* **10**, 014007 (2005).

11. J. Q. Lu, P. Yang and X. H. Hu, "Simulations of light scattering from a biconcave red blood cell using the finite-difference time-domain method," *Journal of Biomedical Optics* **10**, 024022 (2005).

12. R. Drezek, A. Dunn and R. Richards-Kortum, "A pulsed finite-difference time-domain (FDTD) method for calculating light scattering from biological cells over broad wavelength ranges," *Optics Express* **6**, 147-157 (2000).

13. A. Karlsson, J. P. He, J. Swartling and S. Andersson-Engels, "Numerical simulations of light scattering by red blood cells," *IEEE Transactions on Biomedical Engineering* **52**, 13-18 (2005).

14. R. Drezek, A. Dunn and R. Richards-Kortum, "Light scattering from cells: finite-difference time-domain simulations and goniometric measurements," *Applied Optics* **38**, 3651-3661 (1999).

15. S. V. Tsinopoulos and D. Polyzos, "Scattering of He-Ne laser light by an average-sized red blood cell," *Applied Optics* **38**, 5499-5510 (1999).

16. J. D. Wilson, C. E. Bigelow, D. J. Calkins and T. H. Foster, "Light scattering from intact cells reports oxidative-stress-induced mitochondrial swelling," *Biophysical Journal* **88**, 2929-2938 (2005).

17. K. S. Yee, "Numerical Solution of Initial Boundary Value Problems Involving Maxwells Equations in Isotropic Media," *IEEE Transactions on Antennas and Propagation* **AP14**, 302-307 (1966).

18. A. Taflove, *Computational electrodynamics: the finite-difference time-domain method*, (Artech House Inc., Boston, 1995).

19. G. Mur, "Absorbing Boundary-Conditions for the Finite-Difference Approximation of the Time-Domain Electromagnetic-Field Equations," *IEEE Transactions on Electromagnetic Compatibility* **23**, 377-382 (1981).

20. Z. P. Liao, H. L. Wong, B. Yang and Y. Yuan, "A Transmitting Boundary for Transient Wave Analyses," *Scientia Sinica Series a-Mathematical Physical Astronomical & Technical Sciences* **27**, 1063-1076 (1984).

21. J. P. Berenger, "A Perfectly Matched Layer for the Absorption of Electromagnetic-Waves," *Journal of Computational Physics* **114**, 185-200 (1994).

Chapter 3

An integrated microfluidic planar waveguide cytometer

3.1 Introduction

Flow cytometry allows characterization of single particles and biological cells in a stream of fluid. This technique has applications in the fields such as cellular biology and biomedical applications. A procedure for obtaining 2D wide angle light scattering patterns from a single scatterer is of great interest in cytometry. It has been reported that the scattered light distribution (over polar angle range) contains specific cellular information.[1, 2] For example, the nucleus (the largest organelle in a cell) is the main contributor to scattered light at small angles.[3, 4] Numerous studies indicate that nano-scale structures such as mitochondria within a cell play an important role in the observed side-scatter spectra.[3-6] Furthermore, the azimuthally-distributed light scattering contains information about organelles inside biological cells. Limitations with conventional cytometry in obtaining such rich information are due to the limited angular range that can be detected and/or the lack of 2D scatter patterns.

The "lab-on-a-chip" (LOC)[7, 8] techniques have recently be applied in the development of new flow cytometers.[9] This requires the shining of laser light into the microchannel to illuminate the scatterers. A direct method for coupling a beam into a slab waveguide is "end-fire" coupling.[10] This technique requires that the

waveguide has clean edges, and that the incident beam be well focused and positioned. Available light scattering measurements also have used a fiber to illuminate scatterers in a tank.[4] Micro fabrication technique have also been used to shine light into a micro channel for light scattering illumination via a micro-fabricated tapered structure waveguide.[11]

There are many other issues that need to be addressed for better light scattering measurements in flow cytometry. This includes the alignment of the single scatterer and the detector in a bulk system, which make it difficult to induce and detect side-scattered light, and the lack of an effective method to trap or otherwise to immobilize the single scatterer in a microfluidic flow. Although researchers have resorted to short integration times (500ns) in order to obtain single scatterer light scattering spectra in a fluidic flow,[12] short integration times however require high quality detectors and high power lasers.

We aim to develop an inexpensive cytometer that can resolve the above challenges in cytometry. In chapter 3, I will try to address all the above mentioned issues for the development of a novel cytometer. A UV-curable epoxy edge bonding method for microchip fabrication is developed. A prism coupling technique is described to couple laser beam into a liquid-core waveguide cytometer. A method for immobilizing a single scatterer in a fluidic flow is also developed. Finally, the integration of the microfluidic planar waveguide cytometer in a laser safety dark room is described. This cytometer can be further developed as a miniaturized handheld cytometer with the advancements in LOC techniques.

This chapter is based on a recently accepted journal paper by X. T. Su, *et al.*,[13] and a recently published Proceedings of SPIE paper by X. T. Su, *et al.*[14]

3.2 From a hemispherical lens cytometer to an integrated microfluidic planar waveguide cytometer

As a first step, our group has previously developed a hemispherical lens cytometer for the purpose of obtaining 2D scatter patterns.[15] Figure 3.1(a) shows the experimental setup of the hemispherical lens cytometer, and Fig. 3.1(b) is a schematic cross section of this cytometer. The rationale for using a hemispherical lens for collecting the scattered light was to enable one to observe very wide angle 2D light scattering patterns. As can be seen from Fig. 3.1(b), for a digital camera at a certain distance d from the superstrate, the hemispherical lens bends the scattered light to its central line. Without the hemispherical lens, the large angle scattering will be out of the numerical aperture of the digital camera. In this hemispherical lens cytometer, a prism-coupling technique has been used to illuminate the scatterers. This prism-coupling technique will be explained later in this chapter. The light scattering from a scatterer can be collected by the hemispherical lens, and 2D light scattering patterns can be obtained by using the digital camera. By using this hemispherical lens cytometer, 2D backward scattered light patterns of 4 and 9.6μm (diameter) polystyrene beads have been obtained. A more complete description about how this cytometer works can be found in our recently published work.[15]

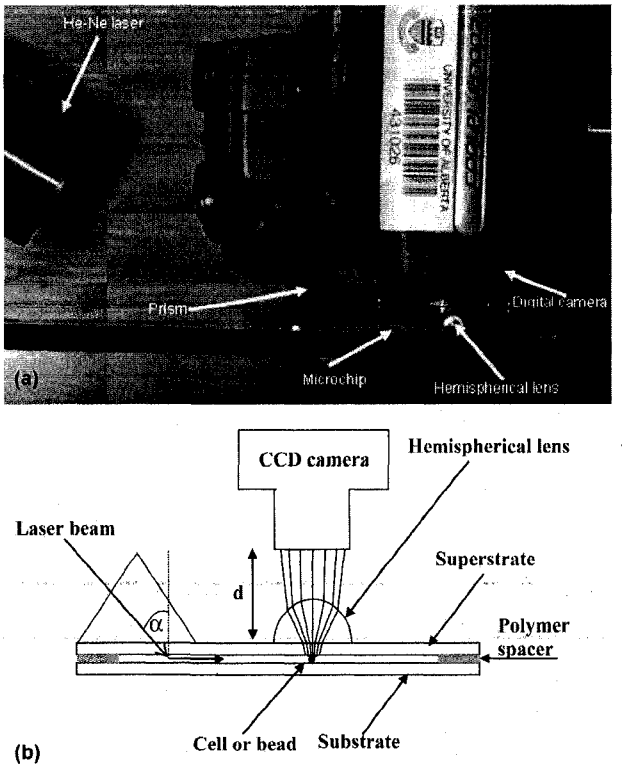

Figure 3.1 A hemispherical lens cytometer capable of obtaining wide angle 2D light scattering patterns. (a), experimental setup of the hemispherical lens cytometer. (b), a schematic of the hemispherical lens cytometer. In this experimental setup, the light scattering is collected through a hemispherical lens, and 2D light scattering patterns are obtained by using a digital camera.

The hemispherical lens cytometer has some serious limitations. The use of the hemispherical lens and the optical lens in the digital camera make the light scattering simulations in the experimental instrument complex, especially for 2D simulations. As we need to transform the 2D simulated far-field scattered light through the complex lens system onto a detector to compare with the experimental results. Secondly, there is no control of the scatterer position in the hemispherical lens cytometer, which cause difficulties in comparing the experimental results with simulations.[15] Besides, the digital camera that is used as a detector limits the understanding of light scattering as compared with the high resolution 2D scatter patterns that will be shown in Chapter 4. Furthermore, wide

angle light scattering measurements can be better achieved with new experimental designs.

The idea of using a CCD detector to obtain the 2D light scattering patterns is adopted to overcome some of the limitations of the hemispherical lens cytometer. If a single scatterer is positioned very close above a plane CCD, its wide angle 2D light scatter patterns can then be obtained by the CCD. Figure 3.2(a) shows the idea of using a CCD detector to obtain scatter patterns. In Fig. 3.2(a), the laser beam is prism-coupled into the glass chip (fabricated by bonding two Fisher glass slides), and a CCD detector is put in close proximity underneath the glass chip. However the design shown in Fig. 3.2(a) cannot be used to obtain light scatter patterns from single microbeads, since the strong laser beam propagating in the glass chip causes blooming of the CCD detector.

The limitations of the earlier designs in which a CCD detector was used include large background scattering in the experimental design depicted in Fig. 3.2(a) and the lack of an effective means of controlling the position of the scatterer in both the designs shown in Fig. 3.1(a) and Fig. 3.2(a). That is, we have no idea where the position of the single scatterer is relative to the detectors. This makes it difficult to determine the scattering angular range that will be obtained. To have better control of the experiments, an idea to simultaneously image a single immobilized scatterer and obtain its 2D scatter patterns was developed. As will be discussed later in Chapter 3, an Aluminum(Al)-coated glass slide with microsize observation windows helps to reduce the background light scattering. The microsize observation window helps in immobilizing a single scatterer in the microfluidic channel. The methods developed for microfluidic chip fabrication and single scatterer immobilization in a fluidic flow are also of great importance to this project. The new developed experimental instrument sits on an optical bench in a dark room and is shown in Fig. 3.2(b). As compared with the experimental instruments shown in Fig. 3.1 (a) and Fig. 3.2(a), the use of an optical bench makes the new system more stable for immobilizing a single

scatterer in a fluidic flow and for light scattering measurements. The dark room not only serves as a control area but also helps to reduce the stray light from the surroundings. Figures 3.2(c) and (d) show the main differences between the experimental setups as shown in Figs. 3.2(a) and (b), where Fig. 3.2(b) is with a microscope and an Al-coated substrate.

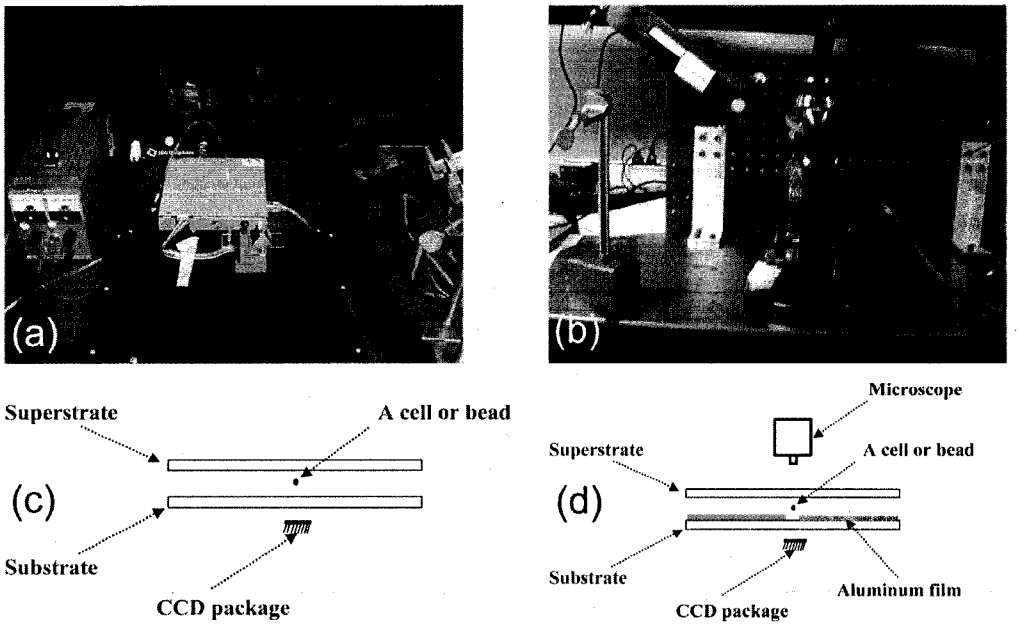

Figure 3.2 Experimental setups for light scattering measurements. (a), the experimental setup to use a CCD to obtain 2D scatter patterns. (b), the experimental setup to simultaneously image a single scatterer and obtain its scatter patterns by using a CCD. The whole system of (b) sits on an optical bench in a dark room. (c) and (d) are the cross section schematics for the core parts of (a) and (b), respectively, to show the differences.

The development and the integration of the microfluidic planar waveguide cytometer as shown in Fig. 3.2(b) will be discussed in the following sections in Chapter 3.

3.3 Microchip fabrication

3.3.1 Fabrication of the aluminum-coated glass slides with micro-size observation windows

In order to improve the signal to noise (S/N) ratio of the designed cytometer, an aluminum coated glass slide with micro-size observation windows was fabricated, and this serves as the waveguide substrate. This thin Al film will block most of the noise (scattering from the scatterers not in the observation window, and from the waveguide structure) from being collected by the CCD detector.

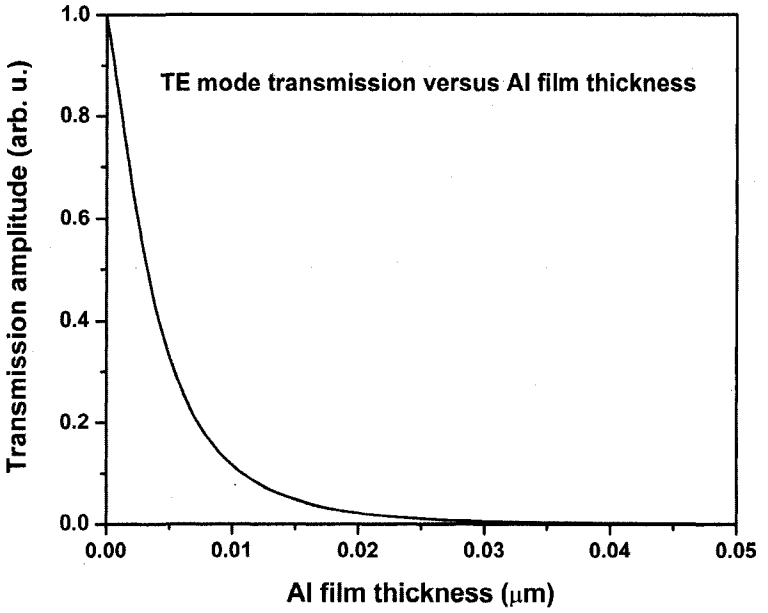

Figure 3.3 Simulation shows the Al film thickness needed to block most of the light at normal incidence.

Simulations of the film transmission were performed by using the transfer matrix method.[16] For the simulations, a planar waveguide was assumed containing a semi-infinite superstrate of glass (refractive index 1.5), a layer of water with a thickness of 200μm (refractive index 1.334), and a semi-infinite substrate (refractive index 1.47) coated with a layer of Al (refractive index $1.38 + i7.62$)[17]. Figure 3.3 shows the transmission amplitude versus the Al film thickness for

normal incidence of a 632.8nm wavelength from the water to the Al-coated substrate. As shown in Fig. 3.3 we find that the transmission amplitudes are very small when the Al film thickness is greater than 25nm. A 45nm Al film blocks 99% of the incident light even at an incident angle of 0^0 (Fig. 3.3).

The fabrication of the Al coated glass slides used the techniques of sputtering and photolithography. Al was sputtered onto a 4 by 4 inch Borofloat glass substrate (Paragon Optical Company, USA) using a Lesker magnetron sputtering system (Kurt J. Lesker Company, USA). The film thickness measured by an Alpha-Step profilometer (KLA-Tencor, USA), is 45nm. A HPR 504 thin photoresist (Shipley Microelectronics, USA) coating was then spun onto the film side of the substrate using a Solitec spinner (Solitec Spinner, USA). The constants set for the spinner are: spread 500rpm for 10 seconds, and spinning at 4000rpm for 40 seconds. In order to remove the photoresist solvent and to promote adhesion of the photoresist to the wafer, the photoresist-coated substrates were baked in an oven for 30 minutes at 115^0C.

The mask used in the experiments was designed using L-Edit version 8.0 (MEMS Pro, France). The mask pattern is shown in Fig. 3.4. The micro windows shown in Fig. 3.4 are of diameters 150, 200, 300, 400, 600 and 800 microns. The dark square corners were designed for better alignment. This mask was specially designed to bond with a standard 3 inch by 1 inch pre-cleaned microscope slide superstrate (12-550A, Fisher Scientific, USA). As shown in Fig. 3.5, the superstrate is designed with inlet and outlet holes drilled by using a water jet driller. The two holes were designed on the same end of the microscope slide for better compact integration of the system. The mask designed as in Fig. 3.4 guarantees the good alignment of the fabricated substrate with the superstrate, by allowing a prism sitting on one end of the substrate, and the other end for pump in and pump out holes. Compared with the conventional photomasks prepared using a mask writer,[18, 19] here we printed our pattern onto a transparency film (1828dpi, Fuji Luxel F-9000 POS, Japan.), which is inexpensive and can be done in hours.

The AB-M mask aligner (AB-M Inc., USA) was used for the UV exposure. The illumination light source wavelength was 400nm (50mW/cm^2), and the exposure time was 40 seconds. After UV exposure, the substrates were then developed using the 354 developer (Shipley Microelectronics, USA), where the photoresist exposed to the UV light was dissolved. The uncovered (photoresist removed) Al film was then etched off by using an Al etchant (Arch Chemicals Inc., USA). The 4 inch by 4 inch glass substrates were cut into 3 inch by 1 inch glass slides using a diamond saw. The cut out glass slides were then cleaned using acetone and methanol.

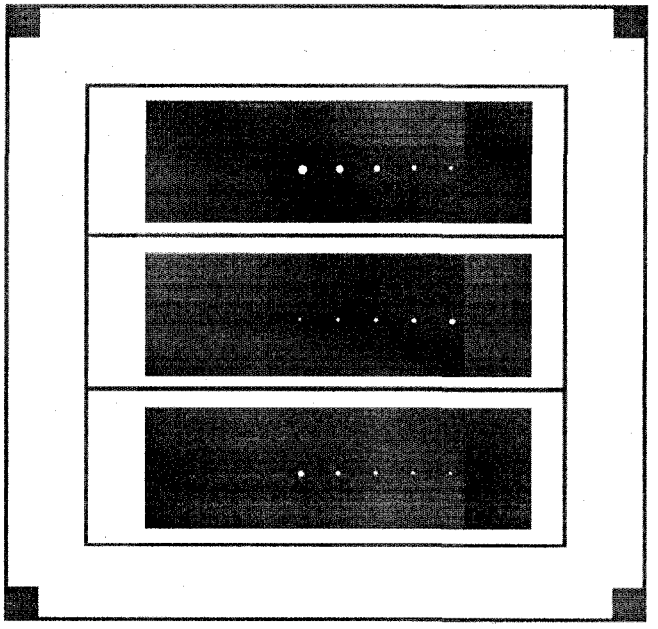

Figure 3.4 Mask designed for the chip substrate fabrication. The micro windows were designed with diameters 150, 200, 300, 400, 600 and 800 microns, shown as white dots.

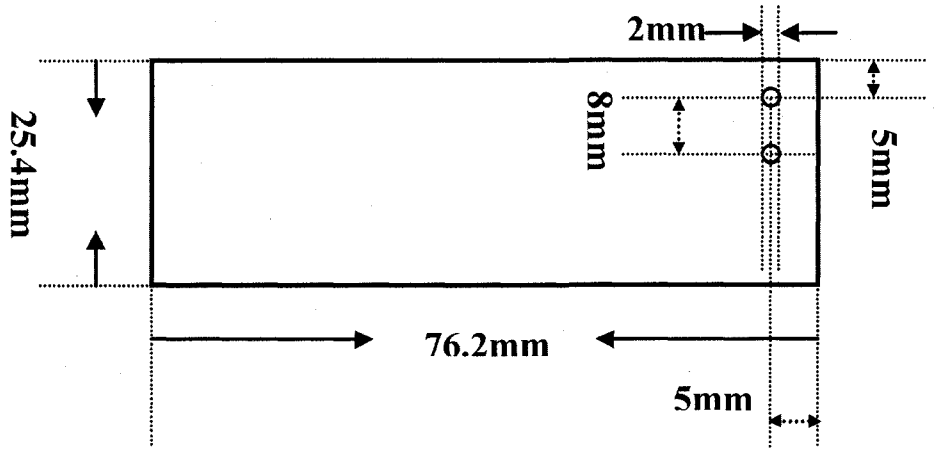

Figure 3.5 Design for the chip superstrate. The two holes serve as the solution inlet and outlet.

3.3.2 Chip fabrication using UV-curable epoxy edge bonding method

The conventional photolithographic technique is well developed for the fabrication of microfluidic channels.[18, 19] The high cost of the photolithographic equipment, the necessity for clean rooms, and the toxic materials used in the fabrication limit the application of this photolithographic technique in the area of biology. Recently, Whitesides and colleagues have developed a set of techniques called "soft lithography",[20, 21] which is an alternative to photolithography and which is more suitable for biological applications. The soft lithography technique uses polydimethylsiloxane (PDMS), which is transparent to visible light and can be used to fabricate films as thin as 100μm.[22] Recently, an epoxy-based[23] microchannel fabrication technique has been developed. We demonstrate here a UV-curable epoxy edge bonding method that combines the standard gasket method[24] and epoxy method for microchip fabrication. This method is inexpensive and time efficient when compared with any other reported microchannel fabrication technique, and there is no clean room requirement. By using this technique, a transparent microchip can be obtained.

The fabrication of the microchip is illustrated in Figure 3.6. The superstrate is the microscope glass slide with two drilled access holes. The U-channel was designed using L-Edit and then printed out on a transparency (Canon Transparency type E, thickness 100μm, Canon USA Inc.). The U-channel model as shown in Figure 3.6 is cut from the transparency. The designed U-channel has a width of 1500μm, larger than the laser beam diameters of interest and hence ensuring that light scattering from the channel edges is small. The substrate is the Al coated glass slide. Both the superstrate (as shown in Fig. 3.5) and the substrate were pre-cleaned using acetone and methanol, and rinsed with IPA (Isopropyl alcohol). The three slides were aligned using the holes on both substrates, and UV-curable epoxy (Norland Optical Adhesive 81, Norland Products Inc., USA) was applied on the edges. This adhesive is sensitive to the entire range of long wavelength UV light from 320 to 380nm. The epoxy is cured using a high intensity UV lamp (SB-100P, Spectroline UV lamp, 4.8mW, Spectronics Corporation, USA) for 2 minutes. Since the epoxy is oxygen inhibited, any excess epoxy on the edges remains uncured can be removed by using an acetone or alcohol-moistened clean room wipe. The bonded chip can be separated by soaking in a chlorinated solvent such as methylene chloride. Normally, the bonded area will separate overnight.

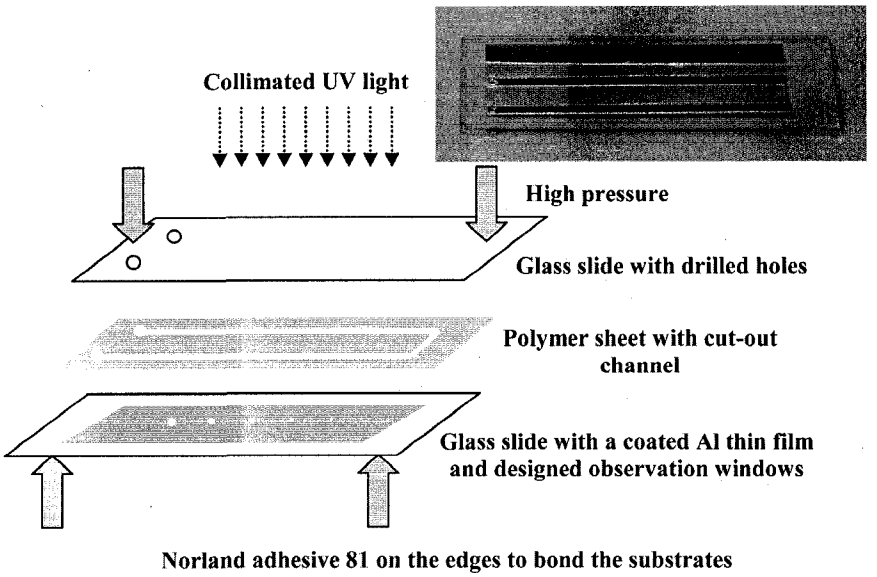

Figure 3.6 Illustration of the UV-curable epoxy edge bonding method for chip fabrication. The inset shows a fabricated microchip.

The fabricated microchip was examined under a Zeiss Axiovert 200 microscope (Carl Zeiss, Germany). Special attention was paid to the micro-size observation window area. The micro-size observation window not only improves the S/N ratio, but also serves as an important element for immobilizing the single scatter in the flow. Furthermore, the idea of using a micro-size observation window makes single scatterer light scattering measurements possible. It is also worth mentioning that the micro-size observation window helps in the alignment of the bulk system. The micro-size observation window images are shown in Fig. 3.7. As shown in Fig. 3.7, (a) is for an observation window of 200μm diameter, (b) is for an observation window of 300μm diameter, (c) is for an observation window of 400μm diameter, and (d) is for an observation window of 600μm diameter. All the observation windows appear to be clear of contaminants.

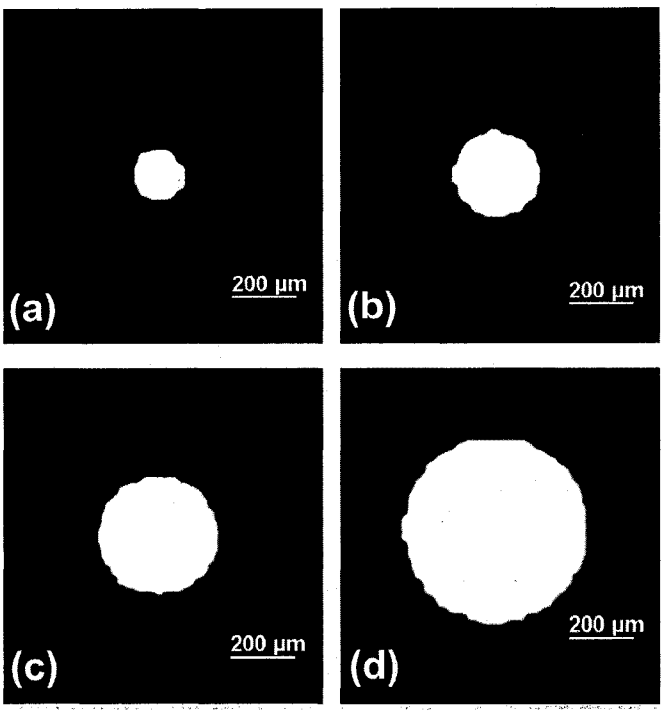

Figure 3.7 The different size micro observation windows on chip under a microscope. The designed sizes are 200, 300, 400 and 600µm, for (a), (b), (c) and (d), respectively.

3.4 Prism coupling laser light into a liquid-core waveguide

The prism coupling technique that was used to couple a laser beam into a liquid-core waveguide is illustrated in Fig. 3.8. Contrary to a conventional waveguide, where the light is confined in the waveguide by total internal reflection, the liquid-core waveguide has a core of lower refractive index compared with the substrates. The light that propagates in such a waveguide will be confined due to the high Fresnel reflectivity.[15] Such a waveguide supports the propagation of leaky modes.[25]

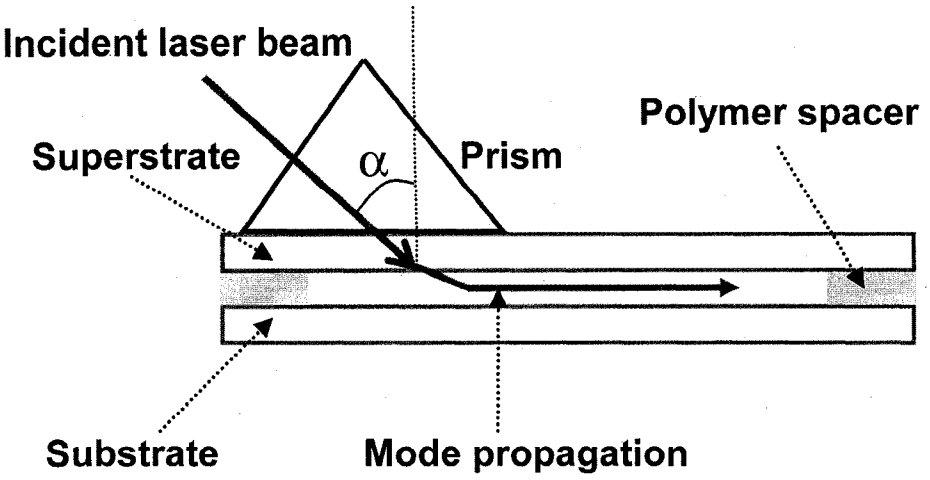

Figure 3.8 Prism coupling a laser beam into the liquid-core waveguide. The mode can propagate for several centimeters.

As shown in Fig. 3.8, a prism sits on top of the microchip. The prism and the superstrate can be assumed to have a constant refractive index N. Unlike the well-known prism coupling technique in thin film measurements,[26-28] where the evanescent field is used to couple the beam into a thin film, we have used the leaky nature of the liquid-core waveguide. As the light can leak out from such a liquid-core waveguide, light can also be coupled into it. Yet the mode can only be generated when the phase matching condition[29] (Equation 3.1) is satisfied,

$$\sin\alpha = \beta / N, \tag{3.1}$$

where β is the effective mode index of the waveguide, and α is the incident angle as shown in Fig. 3.8.

The phase matching condition can be explained in Fig. 3.9 as follows.

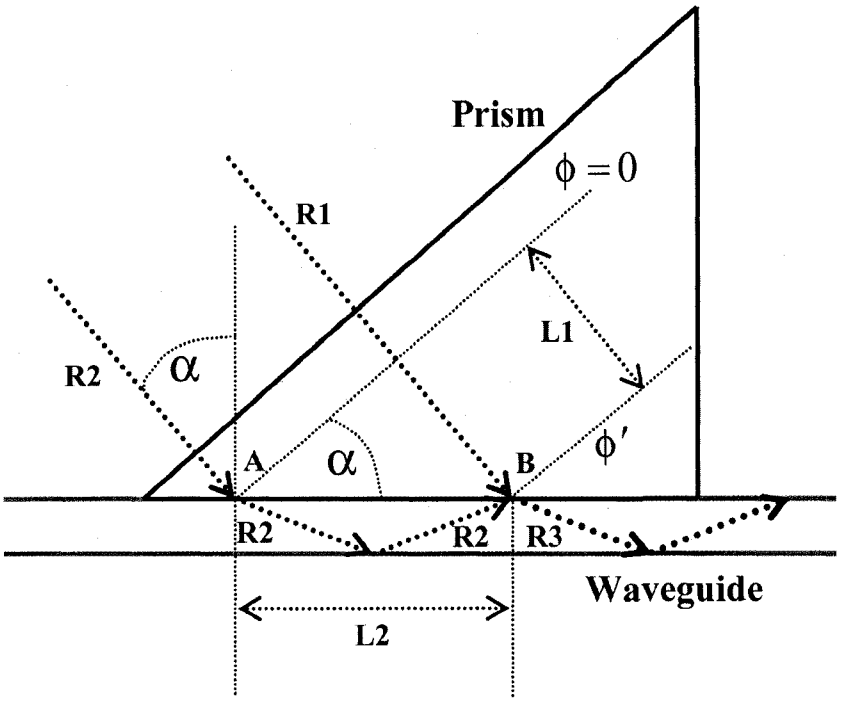

Figure 3.9 Light ray analysis for the phase matching condition of the prism coupling technique. The phase matching condition is satisfied at a particular angle α.

The phase difference[30] is defined as

$$\delta = k_0 \Lambda = \frac{2\pi}{\lambda_0} n(x_1 - x_2), \tag{3.2}$$

where $\Lambda = n(x_1 - x_2)$ is the optical path difference(OPD), k_0 is the incident wave propagation number in vacuum, and n is the refractive index of the medium. Suppose we have two light rays from an incident laser beam denoted as R_1 and R_2. At a certain point, they have the same phase $\phi = 0$. Ray R_1 immediately goes into the micro channel at point A, and follows a zigzag propagation[26, 31] in the channel. At point B, we assume R_1 and R_2 have the same phase ϕ'. During this time of propagation, the phase difference for R_1 is,

$$\delta_1 = k_0 N L_1, \tag{3.3}$$

the phase difference for R_2 is,

$$\delta_2 = k_0 \beta L_2, \tag{3.4}$$

the phase matching condition is $\delta_1 = \delta_2$, that is,

$$k_0 N L_1 = k_0 \beta L_2 . \tag{3.5}$$

From Fig. 3.7 we can find that,

$$\sin\alpha = \frac{L_1}{L_2} . \tag{3.6}$$

Combining Equations (3.5) and (3.6), we find the phase matching condition as

$$\sin\alpha = \frac{L_1}{L_2} = \frac{\beta}{N} . \tag{3.7}$$

The distance that the coupled mode can propagate in the liquid-core waveguide is typically centimeters, which enables the integration of other elements on a glass slide substrate.

3.5 Cytometer detector consideration - using a CCD detector

In cytometry, a suitable detector is required to convert the optical information to a digital form suitable for subsequent analysis. The most common detector is the semiconductor photodiode. The photodiode has excellent linearity of output current to the incident light intensity, and a high quantum efficiency (typically of 80%), where the quantum efficiency (QE) is defined as[1]

$$QE = 100\% \times \frac{\text{electrons out}}{\text{photons in}} . \tag{3.8}$$

The photodiode is commonly used for the forward scatter detection since it has no gain. Compared with a photodiode, photomultiplier tubes (PMTs) have a relatively high gain (10^7 or more electrons out for each photon in), and are suitable for detecting weakly scattered side-scatter signals. The disadvantage of PMTs compared with the photodiodes is their low QE (less than 25%), and the fact that they need to be operated at high voltage (300~2000V).

Modern CCDs have a higher QE (greater than 40%)[32] and have their own gain. Moreover, a CCD can be used for an integrated exposure time, and the observed 2D scene can be easily divided into a well-determined 2D positional output. We chose a consumer grade, uncooled CCD (Sony, ICX098BQ) that has a low dark

current (using Sony's Hole-Accumulation Diode (HAD) technology), which was obtained as part of a consumer webcam (a Logitech Quickcam 4000). The data was acquired at a depth of 8-bits per pixel using the webcam software.

In the field of CCD image processing, dark field and flat field images are of great importance for better understanding of the signal.[32] The CCD dark field images are taken with the CCD shutter closed for a time period equal to the exposure time used to take the object image. This image usually can be subtracted from the object image, and accounts for both readout noise and dark current. A representative scan of the Sony ICX098BQ dark field image is shown in Fig. 3.10, where an integration time of 1/15 second has been used. The scan is performed horizontally from pixels 0 to 639, and averaged from pixels 239 to 241 vertically for the obtained 2D CCD frame (not shown here). As can be seen from Fig. 3.9, the dark field intensity level is quite uniform, and with a mean around 3 counts out of a total CCD counts of 256.

Compared with its neighbors, each pixel of a CCD has a slightly different gain or QE value. A flat field image is usually obtained in order to flatten the relative response for each pixel to the incident radiation, where the object image is divided by the mean flat field image. Ideally, a flat field image is obtained by a uniform illumination of every pixel on the CCD. The variations in pixel sensitivity of the CCD were checked by illuminating each pixel with the same intensity under an LED (EFR5366X, LED red clear 5mm) illumination at a wavelength of 635nm. The LED was positioned perpendicular to the CCD center at a height of 40cm. A flat field image obtained with an integration time 1/15 second is shown in Fig. 3.11. A cross section scan of this flat field image (horizontally from pixels 0 to 639, and averaged from pixels 239 to 241 vertically) has a mean of 188 counts, with a SD of 3 counts. This shows the flat field image is fairly uniform. The "doughnuts" in the image are from dust or other contaminated specks on the CCD window glass.[32]

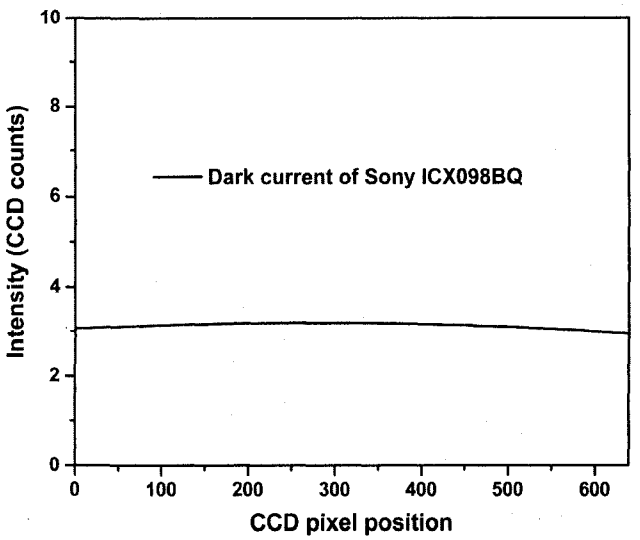

Figure 3.10 A scan of the CCD dark field image shows the dark field intensity variations with CCD pixel positions. The CCD dark field intensity mean level is about 3 counts of a total CCD count of 256 at an integration time of 1/15 second.

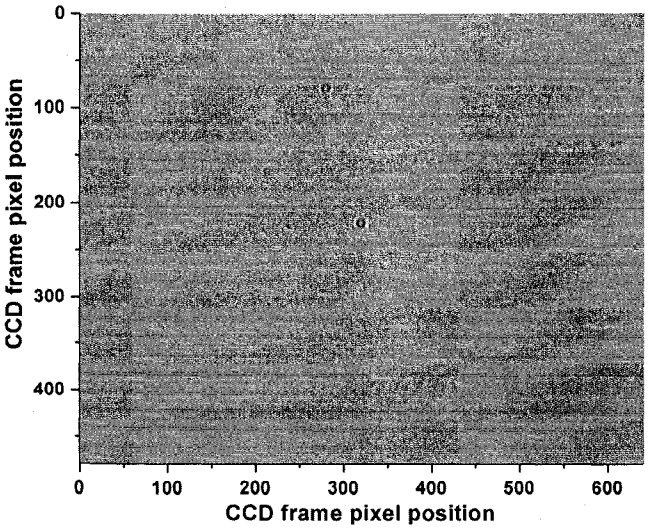

Figure 3.11 CCD flat field image under LED illumination.

3.6 Cytometer light source considerations - building the laser safety dark room

Light scattering measurements in a flow cytometer usually take only a few microseconds or less. The scattered light, especially in the side-scatter direction is

only a very small fraction of the total illumination intensity. Thus, to obtain wide angle light scattering spectra, the light sources used must emit a relatively large number of photons per unit time per unit area. Arc lamps and lasers are two classes of light sources that meet such criteria.[33]

The use of arc lamps in light scattering measurements involves complex optical designs. Although a low power laser can be focused to achieve a higher irradiance, the task of focusing and then collimating the laser beam is not easily integrated into light scattering measurements. Usually the light scattering measurements in flow cytometry use a laser source of output power greater than 5mW.[2, 4, 34] These lasers belong to class IIIa and class IIIb lasers. A high energy laser control area is mandatory for performing experiments with these lasers.

The high energy laser control area that I built for this project is fully covered and separated with heavy black cloth. This laser control area also serves as a dark room. The experimental setup in the laser control area sits on an optical bench.

3.7 Method to immobilize the micro-size scatterer in flow

There are several reported ideas for trapping the micro-size objects in flow, such as dielectrophoresis (DEP),[35] an optical trap[2, 9, 36] and eddy flow trapping.[37] The DEP trapping strategy is challenging to apply in light scattering experiments due to many limitations such as the rigid requirement in microfabrication. The optical manipulation techniques derived from single-beam optical traps are known as optical tweezers. Optical tweezers use the forces exerted by a strongly focused laser beam to trap and move object ranging in size from tens of nanometers to tens of micrometers. Stable trapping requires the optical tweezers to be constructed around microscope objective lenses. Also, the use of a second laser for the optical trap requires further determination of the light scattering that originates from the illumination source. For the eddy flow trapping method, mechanical oscillation is necessary to generate eddies, making it difficult to be used in the study of the light scattering problems. The method I have used here to immobilize a microbead in a

flow is simple. As shown in Fig. 3.12, the arrow shows the flow direction under a positive pressure, which is also the laser mode propagation direction in the micro channel. By applying positive (along the arrow direction) and negative pressure as required, we are able to manually immobilize a single scatterer in the observation window area in a microfluidic flow.

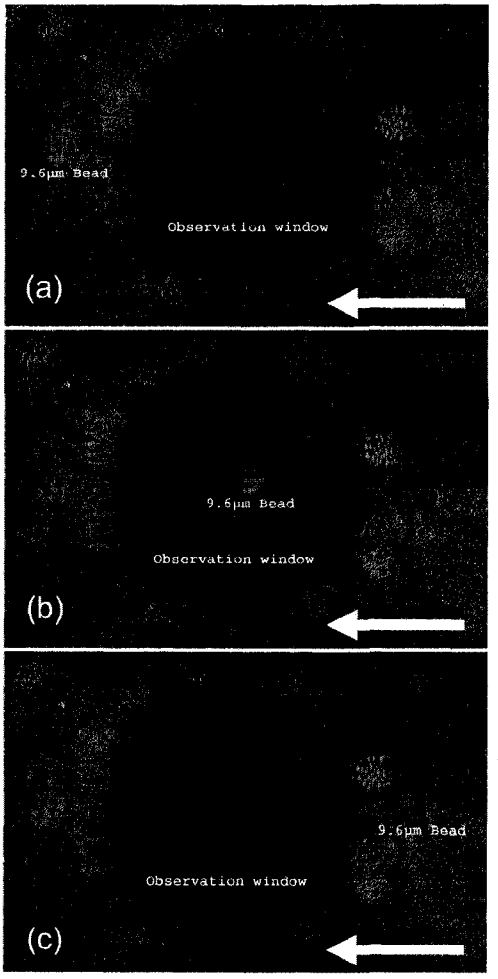

Figure 3.12 Immobilization of a 9.6μm (diameter) polystyrene bead traversing the observation window. The arrow shows the laser propagation direction, which is also the flow direction under positive pressure.

Figure 3.12 shows the immobilization results of a 9.6μm polystyrene bead in a microfluidic flow by using this immobilization method. The obtaining of the images as shown in Fig. 3.12 is as follows. Once the system is in good micro

alignment, I focus the microscope on the observation window. If the scatterer is positioned in the observation window area, we defocus the microscope on the observation window, and hence the scatterer is futher defocused due to the fact that there is a certain distance between the scatterer and the surface of the observation window. As shown in Fig. 3.12, by applying positive and negative pressures as required, a single 9.6μm polystyrene bead can be immobilized at different positions around the observation window area. The circular dark area in Fig. 3.12 is the observation window area. The 9.6μm polystyrene bead defocused scatter images with clear fringes are at different positions around the observation window area. Figure 3.12(a) shows the bead that has passed over the observation window, Fig. 3.12(b) shows the same bead immobilized around the center of the observation window, and Fig. 3.12(c) shows the bead after it has been moved out of the observation window area. The images shown in Figs. 3.12(a) to (c) were taken using a Nikon camera (Nikon Coolpix 990) with an integration time of 1/4 second (F4).

3.8 Integration of the microfluidic planar waveguide cytometer

A detailed picture of the integrated microfluidic planar waveguide cytometer is shown in Fig. 3.13. The laser is mounted on a breadboard by using a cylinder tube laser holder. The breadboard is mounted vertically on an optical bench. The laser can be rotated freely to set the phase matching angle. Once the phase matching angle is satisfied, the laser light will be prism-coupled into the waveguide cytometer. The CCD detector in an aluminum box is put right beneath one of the observation windows on the microchip. The inlet pump tube is connected with a syringe pump, through which we apply positive or negative pressure to immobilize a single scatterer in the micro channel observation window area. The digital camera is mounted on the microscope eyepiece tube. The CCD is connected to a computer to record the 2D scatter patterns.

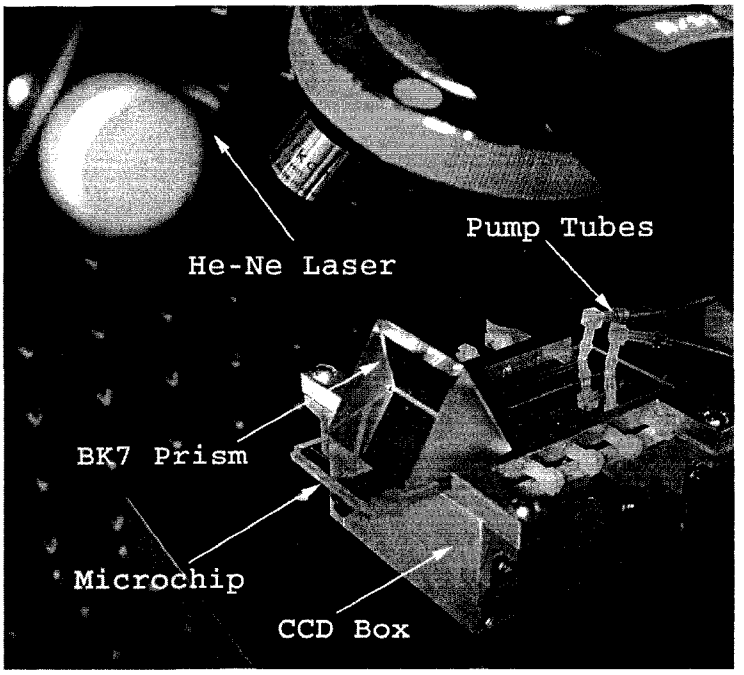

Figure 3.13 The integrated microfluidic planar waveguide cytometer.

A schematic cross section of the experimental setup of Fig. 3.13 is shown in Fig. 3.14. The core part of the integrated waveguide system is a compact structure, including the prism, microchip and the CCD detector. The laser light is incident on the microchip at the phase matching angle, and the optical mode or modes in the waveguide propagate along the microchannel. Once a scatterer is immobilized in the observation window area, a frame of the 2D scattered light pattern is taken by the CCD located beneath the microchannel. A defocused scatter pattern image is also taken by using a digital camera that is mounted on top of the microscope. Another important advantage is that the micro channel and the CCD detector form a planar waveguide structure, which simplifies the application of Mie theory and FDTD method in analyzing results obtained by this experimental setup.[14] The applications of Mie theory and FDTD method in the waveguide cytometer will be discussed in the later chapters.

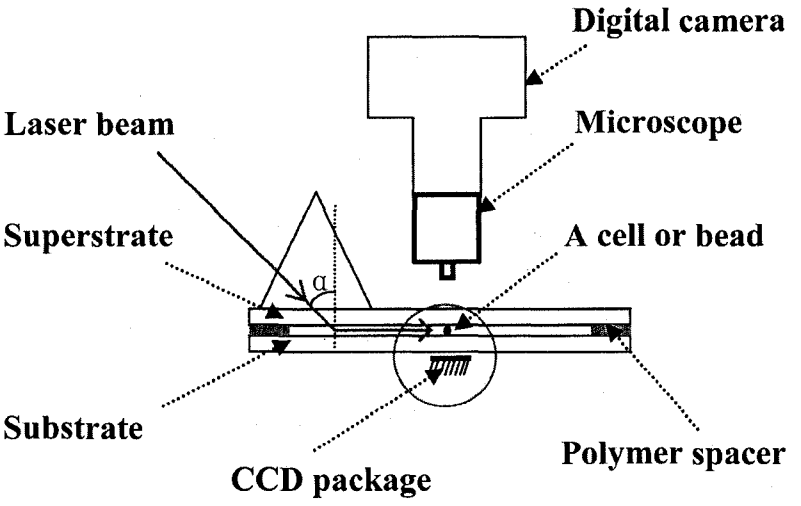

Figure 3.14 A schematic cross section of the integrated waveguide cytometer shown in Fig. 3.13.

The integrated waveguide cytometer is particularly designed to obtain side-scatter patterns because the side-scattered light contains rich information about organelles in single cells.[3, 4] Mie theory simulations were performed to study the single organelle light scattering size dependence. Figure 3.15 gives the light scattering spectra from a single organelle with a radius of 50, 150, 250 and 350nm, respectively. The organelles used here have a refractive index of 1.42. The incident wavelength is 632.8nm, and the surrounding medium has a refractive index of 1.334. As can be seen from Fig. 3.15 for the 50nm scatterer, the scattering intensity is isotropic over the full polar angle range. When the size changes to 150nm, the scattering intensity gradually decreases from 0 to 180^0. Compared with the sizes of 50nm and 150nm, the light scattering intensity variations for the 250nm and 350nm organelles are more complex in the full angular range. A close study of the side-scatter range shows that there is a valley for the organelle of size 250nm and a peak for the 350nm organelle around 80^0. In this case, the side-scatter spectra contain characteristic information (isotropic intensity, gradually decreased intensity, valley intensity and peak intensity) for the different size organelles.

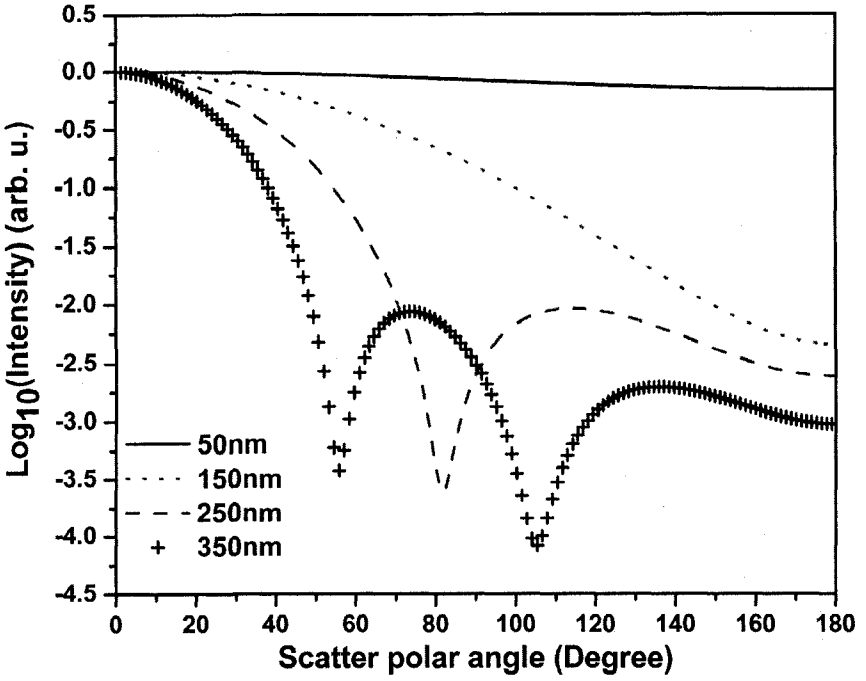

Figure 3.15 Mie theory shows that the side-scatter light is sensitive to the organelle size.

3.9 Conclusions

A UV-curable epoxy edge bonding method was developed for fabrication of the microchips. A prism coupling method was used to introduce the laser beam into a liquid-core waveguide cytometer. A simple but effective method was developed to immobilize a single scatterer in a fluidic flow by applying positive and negative pressures, where the micro fabricated observation windows play important roles in determining the position of the scatterers.

A high energy laser control area has been constructed and an integrated microfluidic planar waveguide cytometer was built on an optical bench in this control area. The integrated waveguide cytometer design enables one to observe a single scatterer immobilized in the observation window area by using a digital camera, while obtain its 2D scatter pattern simultaneously by using a CCD detector underneath the microchip. The new design of the integrated cytometer is ideal for obtaining 2D side-scatter patterns, where the side-scatter spectra contains

characteristic information about the size variation of single organelles as shown by using Mie thoery.

3.10 References

1. H. M. Shapiro, *Practical flow cytometry*, (John Wiley & Sons, Inc., Hoboken, 2003).

2. D. Watson, N. Hagen, J. Diver, P. Marchand and M. Chachisvilis, "Elastic light scattering from single cells: Orientational dynamics in optical trap," *Biophysical Journal* **87**, 1298-1306 (2004).

3. H. B. Steen and T. Lindmo, "Differential of Light-Scattering Detection in an Arc-Lamp-Based Epi-Illumination Flow Cytometer," *Cytometry* **6**, 281-285 (1985).

4. J. R. Mourant, J. P. Freyer, A. H. Hielscher, A. A. Eick, D. Shen and T. M. Johnson, "Mechanisms of light scattering from biological cells relevant to noninvasive optical-tissue diagnostics," *Applied Optics* **37**, 3586-3593 (1998).

5. A. Dunn and R. Richards-Kortum, "Three-dimensional computation of light scattering from cells," *IEEE Journal of Selected Topics in Quantum Electronics* **2**, 898-905 (1996).

6. C. G. Liu, C. Capjack and W. Rozmus, "3-D simulation of light scattering from biological cells and cell differentiation," *Journal of Biomedical Optics* **10**, 014007 (2005).

7. D. Figeys and D. Pinto, "Lab-on-a-chip: A revolution in biological and medical sciences," *Analytical Chemistry* **72**, 330A-335A (2000).

8. H. Craighead, "Future lab-on-a-chip technologies for interrogating individual molecules," *Nature* **442**, 387-393 (2006).

9. H. Andersson and A. van den Berg, "Microfluidic devices for cellomics: a review," *Sensors and Actuators B-Chemical* **92**, 315-325 (2003).

10. C. R. Pollock and M. Lipson, *Integrated phtonics*, (Kluwer Academic Publishers, Norwell, 2003).

11. Z. Wang, J. El-Ali, M. Engelund, T. Gotsaed, I. R. Perch-Nielsen, K. B. Mogensen, D. Snakenborg, J. P. Kutter and A. Wolff, "Measurements of scattered light on a microchip flow cytometer with integrated polymer based optical elements," *Lab on a Chip* **4**, 372-377 (2004).

12. J. Neukammer, C. Gohlke, A. Hope, T. Wessel and H. Rinneberg, "Angular distribution of light scattered by single biological cells and oriented particle agglomerates," *Applied Optics* **42**, 6388-6397 (2003).

13. X. T. Su, K. Singh, C. Capjack, J. Petracek, C. Backhouse and W. Rozmus, "Measurements of light scattering in an integrated microfluidic waveguide cytometer," *Journal of Biomedical Optics* (accepted).

14. X. T. Su, W. Rozmus, C. Capjack and C. Backhouse, "Side scatter light for micro-size differentiation and cellular analysis," *Proc. of SPIE* **6446**, 64460w (2007).

15. K. Singh, X. T. Su, C. G. Liu, C. Capjack, W. Rozmus and C. J. Backhouse, "A miniaturized wide-angle 2D cytometer," *Cytometry Part A* **69A**, 307-315 (2006).

16. J. Petracek and K. Singh, "Determination of leaky modes in planar multilayer waveguides," *IEEE Photonics Technology Letters* **14**, 810-812 (2002).

17. D. R. Lide, *CRC handbook of chemistry and physics*, (Taylor and Francis, Boca Raton, 2007).

18. S. Britland, E. Perezarnaud, P. Clark, B. McGinn, P. Connolly and G. Moores, "Micropatterning Proteins and Synthetic Peptides on Solid Supports - a Novel Application for Microelectronics Fabrication Technology," *Biotechnology Progress* **8**, 155-160 (1992).

19. B. Lom, K. E. Healy and P. E. Hockberger, "A Versatile Technique for Patterning Biomolecules onto Glass Coverslips," *Journal of Neuroscience Methods* **50**, 385-397 (1993).

20. Y. N. Xia, E. Kim, X. M. Zhao, J. A. Rogers, M. Prentiss and G. M. Whitesides, "Complex optical surfaces formed by replica molding against elastomeric masters," *Science* **273**, 347-349 (1996).

21. Y. N. Xia and G. M. Whitesides, "Soft lithography," *Annual Review of Materials Science* **28**, 153-184 (1998).

22. R. S. Kane, S. Takayama, E. Ostuni, D. E. Ingber and G. M. Whitesides, "Patterning proteins and cells using soft lithography," *Biomaterials* **20**, 2363-2376 (1999).

23. P. Sethu and C. H. Mastrangelo, "Cast epoxy-based microfluidic systems and their application in biotechnology," *Sensors and Actuators B-Chemical* **98**, 337-346 (2004).

24. L. Licklider, X. Q. Wang, A. Desai, Y. C. Tai and T. D. Lee, "A micromachined chip-based electrospray source for mass spectrometry," *Analytical Chemistry* **72**, 367-375 (2000).

25. C. Vassallo, *Optical waveguide concepts*, (Elseview Science Publishing Company, Inc., New York, 1991).

26. P. K. Tien, "Light Waves in Thin Films and Integrated Optics," *Applied Optics* **10**, 2395-2413 (1971).

27. R. T. Kersten, "Prism-Film Coupler as a Precision Instrument .2. Measurements of Refractive-Index and Thickness of Leaky Waveguides," *Optica Acta* **22**, 515-521 (1975).

28. R. T. Kersten, "New Method for Measuring Refractive-Index and Thickness of Liquid and Deposited Solid Thin-Films," *Optics Communications* **13**, 327-329 (1975).

29. N. J. Harrick, *Internal Reflection Spectroscopy*, (Wiley, New York, 1967).

30. E. Hecht, *Optics*, (Addison Wesley Longman, Inc., Reading, 2002).

31. H. Hoekstra, J. C. Vantspijker and H. Koerkamp, "Ray Picture for Prism Film Coupling," *Journal of the Optical Society of America a-Optics Image Science and Vision* **10**, 2226-2230 (1993).

32. S. B. Howell, *Handbook of CCD astronomy*, (Cambridge University Press, Cambridge, 2000).

33. G. Durack and J. P. Robinson, *Emerging tools for single cell analysis: advances in optical measurement technology*, (Wiley-Liss, Inc., New York, 2000).

34. R. Drezek, A. Dunn and R. Richards-Kortum, "Light scattering from cells: finite-difference time-domain simulations and goniometric measurements," *Applied Optics* **38**, 3651-3661 (1999).

35. H. Morgan, M. P. Hughes and N. G. Green, "Separation of submicron bioparticles by dielectrophoresis," *Biophysical Journal* **77**, 516-525 (1999).

36. D. G. Grier, "A revolution in optical manipulation," *Nature* **424**, 810-816 (2003).

37. B. R. Lutz, J. Chen and D. T. Schwartz, "Microfluidics without microfabrication," *Proceedings of the National Academy of Sciences of the United States of America* **100**, 4395-4398 (2003).

Chapter 4

Micro-size differentiation with the integrated cytometer

4.1 Introduction

The development of miniaturized cytometers that measure forward scattered[1] and backward scattered[2] light has recently been reported. The task of obtaining side-scatter patterns is challenging due to the lower intensity level of the side-scattered light and the difficulty in resolving the angular structure of this scattering. Furthermore, the validation of a particular light scattering measurement approach requires that comparisons be made with analytical models such as Mie theory or by using numerical simulations such as the Finite-Difference Time-Domain (FDTD) method. This is not easily accomplished when complex experimental setups are involved.

The integrated planar waveguide cytometer as described in chapter 3 addresses a number of issues such as the ability to compare experimental results with known theoretical predictions, the obtaining of 2D high resolution side-scatter patterns, and the resolution of the angular dependence of the scattering. The planar waveguide structure simplifies the modal analysis in such an integrated cytometer. The absence of an optical lens in this planar waveguide structure allows a resolution of the angular dependence of the scattering to be made as well as simplifying the comparison of measured results with predictions

obtained using either Mie theory or simulations employing the FDTD method. The 2D features of the scatter patterns are used to develop a method for determining the location of 90 degree scatter (both polar angle and azimuth angle).

The operation of this cytometer is validated through the use of polystyrene micro-beads that serve as cell mimics in the microfluidic channel. Conventional validation of experimental result tries to match the shape of experimental scatter pattern with theoretical prediction,[3-6] whereas we perform the comparisons both in space and Fourier domain. Comparisons of the 2D scatter patterns that are experimentally obtained with Mie theory predictions confirm the correct operation of the device. A Fourier method for quick size differentiation has also been developed. This is based on comparisons between the Fourier peaks of Mie theory simulations and experimental results from polystyrene beads that range in size from 4μm to 20μm.

This chapter is based on a recently accepted journal paper by X. T. Su, *et al.*[7]

4.2 Modal analysis of the liquid-core waveguide

4.2.1 A method to find modes in a planar liquid-core waveguide

The optical waveguide used in the integrated cytometer as described in chapter 3 has a liquid core that also serves as the microfluidic channel. The planar waveguide structure of the integrated cytometer is illustrated as in Fig. 4.1, which contains a superstrate layer, a fluid layer, and a substrate layer coated with Al film. These three layers form the liquid-core planar waveguide. Such liquid-core waveguides (the core refractive index is lower than the substrates) are therefore optically leaky and this feature allows use of the prism coupling method to excite the modes. The modes propagate along $+z$ direction. In cases where the optical thickness of the core is large, the angular separation between modes may be less than the typical angular divergence of single mode lasers. In such cases, several leaky waveguide modes will be excited, with the optical intensity within the waveguide being a superposition of these modal intensities. Since the liquid-core

waveguide is fundamentally important in the present cytometer design, the method used for modal analysis[8] is described here. The great advantage of this method is its simplicity over the rigorous analytical technique[9, 10] and other various approximation methods.[11, 12]

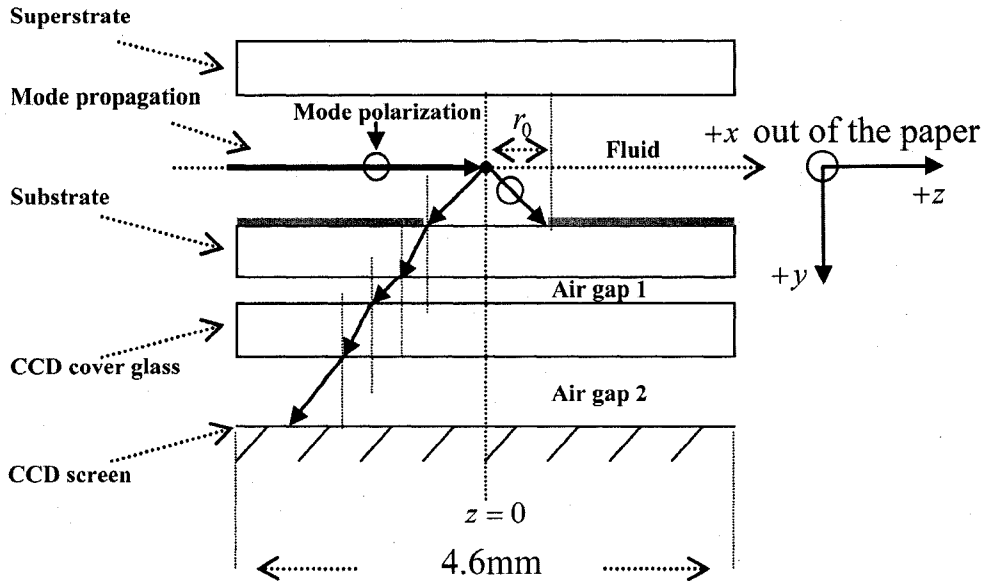

Figure 4.1 Illustration of the planar waveguide structure and the mapping of Mie results onto the CCD screen. The mode propagates along $+z$ direction. The observation window has a radius of r_0. The scattered light is collected by a CCD detector.

The most popular method for finding the modes of a planar waveguide is the thin-film transfer matrix method.[13, 14] This method provides a dispersion equation whose solutions correspond to bound and leaky modes of the waveguide. A simple yet efficient and exact technique based on a smooth transition between bound modes of closed waveguide and leaky modes of open waveguide was used to find the modes.

The planar multilayer waveguide and definition of its parameters are shown in Fig. 4.2. The waveguide consists of N layers labelled with j, $j = 0...N-1$; each layer is specified by its relative permittivity ε_j and thickness d_j. Interfaces between adjacent layers have positions y_j, $j = 1...N-1$. y_0 and y_N are artificial

boundaries placed inside the substrate ($y < y_1$) and the cover ($y > y_{N-1}$) and they are necessary for numeric treatment.

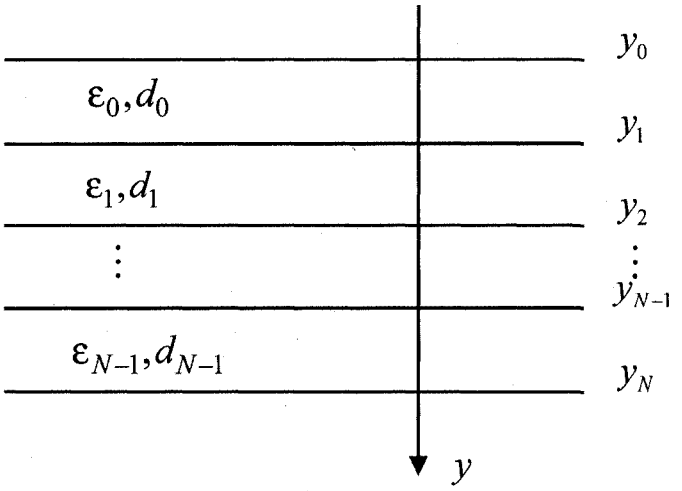

Figure 4.2 Planar waveguide consisting of N layers. The *jth* layer has relative permittivity ε_j and a thickness d_j ; y_j is position of layer interface except artificial boundaries y_0 and y_N.

The electric field of a transverse electric (TE) mode or the magnetic field of a transverse magnetic (TM) mode can be expressed using function $\varphi(y)$ which is solution of the Helmholtz equation. This function in *jth* layer is given by

$$\varphi_j(y) = A_j \cos[a_j(y - y_j)] + \frac{B_j}{a_j} \sin[a_j(y - y_j)] \tag{4.1}$$

$$a_j = \sqrt{k_0^2 \varepsilon_j^2 - \beta^2}\ ,\ k_0 = 2\pi / \lambda_0\ , \tag{4.2}$$

where β^2 is the mode propagation constant, λ_0 is wavelength in vacuum and A_j and B_j are constants characteristic for given layer, mode and polarization.

Realizing that A_j and B_j are values of function $\varphi(y)$ and its derivative at $y = y_j$ and using continuity conditions for normal and tangential components of electric and magnetic field, we can obtain relations between pairs of (A_j, B_j) and

(A_{j+1}, B_{j+1}) for any $j = 0..N-1$. As a consequence, if we know β^2 and (A_j, B_j) for some j we can calculate these pairs for all j. On the other hand if we know (A_0, B_0) and (A_N, B_N) we can obtain dispersion equation for unknown β^2, which can be written in the general form

$$D(A_0, A_N, B_0, B_N, \beta^2) = 0. \tag{4.3}$$

Values of A_0, B_0, A_N and B_N depend on the type of boundary conditions used. It can be shown that (4.3) turns into a new form

$$D(w, \beta^2) = 0, \tag{4.4}$$

where parameter w is 0 for a closed waveguide ($B_0 = B_N = 0$) and 1 when searching for the leaky modes of open waveguide.

The numerical technique for solving this equation when searching for leaky modes is the following. First let us consider a waveguide with a real permittivity profile. For the case where $w = 0$, all solutions of (4.4) up to given order can be easily found as they are real and fulfil the relation $\beta^2 < k_0 \max(\varepsilon_j)$. To this aim we applied the well-known Brent method.[15] Now we allow continuous change of w from 0 to 1. The roots of (4.4) will move inside the complex plane and their new positions can be located using standard numerical routines (*e.g.* Newton-Raphson method[16]), since their previous positions can be used as the initial guess. If the permittivity of the waveguide is complex, we perform the described technique for its real part and then again track the roots in the complex plane while changing the imaginary part of waveguide permittivity.

The microfluidic chip used in this study has a channel height of 200μm, which supports multimode propagation in the waveguide. The modes can be found by using the above method. Shown in Fig. 4.3 are three modes supported by the planar waveguide. If we assume the incident lights for these three modes have equal intensity, Fig. 4.3 shows that the fundamental modes have the strongest intensity level, while the 2nd order mode intensity is the lowest. The solid line shown in Fig. 4.3 is the summation of the first 21 modes found in the waveguide.

This summed mode is symmetrical about the channel central line ($+z$ axis as in Fig. 4.1), with an intensity that drops quickly from the center to the substrates.

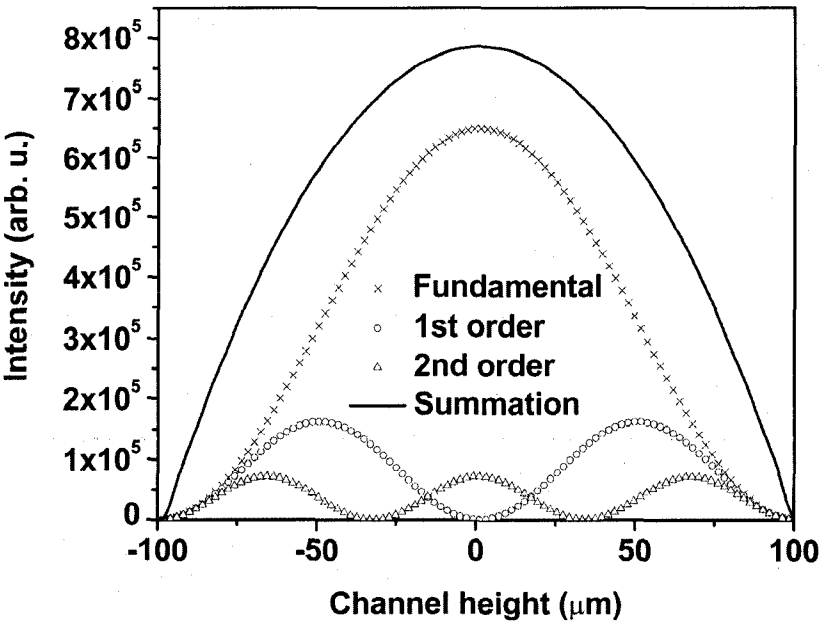

Figure 4.3 Mode profiles in the planar waveguide simulated by using the thin-film transfer matrix method. All modes are assumed to be excited by the same intensity. The summed mode intensity profile is for the first 21 modes.

4.2.2 Mode profile in the liquid-core waveguide

The excitation source used in our experiments is a laser with a Gaussian intensity distribution. In order to determine the excitation of a given mode in the waveguide, the transmission coefficients of the laser beam from the substrate to the liquid-core must be considered. Shown in Fig. 4.4 are the transmission intensity profiles for the laser beam to excite the 18^{th}, 19^{th} and 20^{th} order modes.[8] The areas under different profiles represent the transmission intensity level. These areas are calculated by performing integrations of the profiles in the same angular interval by using a trapezoidal method. Generally speaking, the higher order excited modes give higher transmission coefficients of the intensity for the incident laser beam.

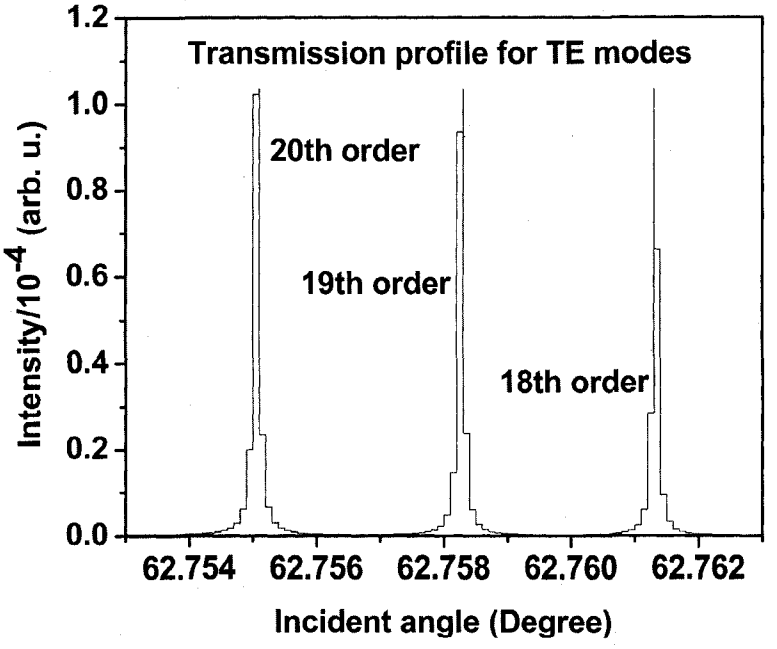

Figure 4.4 Transmission profile for the incident light to excite the modes in the waveguide. Each different mode profile has a different area under the curve.

In order to find the actual modal intensity in the planar waveguide, the modes as found in Fig. 4.3 are multiplied by the Gaussian distribution of the laser intensity and the transmission coefficients for the laser light to excite a given mode. The calculated intensity profiles for the 0^{th} order, 1^{st} order and 2^{nd} order modes are shown in Fig. 4.5. The summation of the first 21 modes supported by the waveguide structure is shown in Fig. 4.5 as the dark solid line, which is normalized to have a highest intensity level of 100 units. Higher order modes are not excited due to the small laser divergence (1.3mrad). This summed mode profile has a uniform intensity distribution across the waveguide with exceptions only very close to the substrates. Since most beads will travel in the uniformly distributed intensity area, an assumption is made that the bead is illuminated by a plane wave. In this case, Mie theory can be used for describing light scattering from a micro-size spherical bead in the integrated waveguide cytometer.

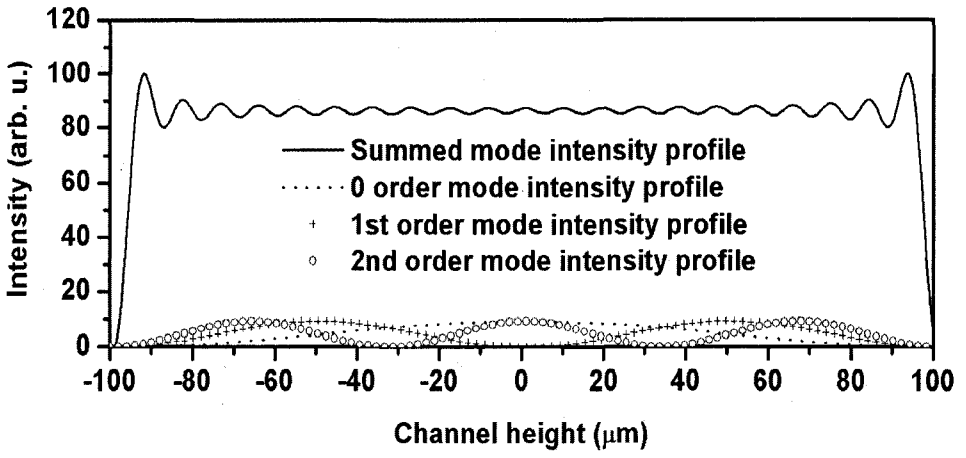

Figure 4.5 The summed mode profile in the waveguide. The summed mode intensity profile is for the first 21 modes. The summed mode intensity is uniform across most of the waveguide intersection.

In a ray diagram representation of mode propagation in a waveguide, the direction of propagation of the distinct modes can be regarded as a zig-zag pattern.[17] In a thick waveguide such as the one considered (200μm), all modes are almost paraxial. The fundamental mode is approximately 0.1^0 off the $+z$ axis, and the 20^{th} order mode is approximately 1.4^0 off the $+z$ axis for the zig-zag propagation. Thus all modes can be assumed to be propagating in parallel and there is no divergence due to the mode propagation through the waveguide.

4.3 Application of Mie theory to the integrated waveguide cytometer

4.3.1 Application of Mie theory: geometry used, transmission coefficients, mapping of far field scattering patterns

For an incident laser propagating in the $+z$ direction as shown in Fig. 4.1, Mie theory gives the spatial scattered intensity distribution (at a certain distance) as a function of polar angle θ and azimuth angle φ (refer to Fig. 1.1). The polar angle θ is measured from $+z$ axis, and the azimuth angle φ is in the xy plane. The mode polarization in the waveguide is the same as the scattered light polarization

(Fig. 4.1).[18] In order to compare Mie simulations with the observed experimental results, it is necessary to map the calculated far field scattering pattern onto the CCD screen. Figure 4.1 shows the integrated planar waveguide structure. This structure simplifies the ray tracing procedure for the propagation of the scattered light in the system. Another advantage of this system is that there are no optical lens systems between the CCD detector and the scatterer in the channel. This simplifies the comparisons between the experimental results and the Mie simulation results.

The amplitude transmission coefficients of Fresnel Equations at an interface are,[19]

$$t_{\perp} = \frac{2n_i \cos\theta_i}{n_i \cos\theta_i + n_t \cos\theta_t} \tag{4.5a}$$

$$t_{\parallel} = \frac{2n_i \cos\theta_i}{n_i \cos\theta_t + n_t \cos\theta_i}, \tag{4.5b}$$

where $t_{\perp}$ is for the perpendicular polarization, and $t_{\parallel}$ is for the parallel polarization. The transmittance T is defined as the ratio of the transmitted to the incident flux and is given by[19]

$$T = \frac{I_t \cos\theta_t}{I_i \cos\theta_i}. \tag{4.6}$$

The transmittances for the perpendicular and parallel polarization, respectively, are given as

$$T_{\perp} = \frac{n_t \cos\theta_t}{n_i \cos\theta_i} t_{\perp}^2 \tag{4.7a}$$

$$T_{\parallel} = \frac{n_t \cos\theta_t}{n_i \cos\theta_i} t_{\parallel}^2. \tag{4.7b}$$

Thus we have,

$$I_{t\perp} = \frac{n_t}{n_i} t_{\perp}^2 I_{i\perp} \tag{4.8a}$$

$$I_{t\|} = \frac{n_t}{n_i} t_{\|}^2 I_{i\|}, \tag{4.8b}$$

where I_i denotes the incident scattered light intensity at an interface, while I_t denotes the transmitted scattered light intensity.

The Mie spatially distributed scattered intensity is projected onto the CCD screen. Snell's Law has been used for the multilayer ray trace as shown in Fig. 4.1. At each interface, the intensity transfer is performed by using Equations (4.8). To compare with experimental results, we also take into account the light intensity cosine dependence on the incident angle to the CCD screen surface, as will be discussed later in this chapter, and the high refractive index of the silica material of the CCD screen.

4.3.2 Validation of Mie mapping ray trace results in the waveguide cytometer

The validation of the ray tracing component of the Mie mapping simulation was performed by comparing results with those found with the BEAM FOUR (Stellar Software, Berkeley) ray trace. For the waveguide structure shown in Fig. 4.1, we assume that the bead is 100μm away from the glass substrate (refractive index 1.47, 1.2mm in thickness). The air gap "1" between the CCD detector and the microchip is 350μm in thickness. The cover glass thickness of the CCD detector is 0.75mm (refractive index 1.5), and the distance between the cover glass and the CCD sensor is 1.25mm – air gap "2". The BEAM FOUR ray trace results are shown in Fig. 4.6, where an offset of $z = 0.1$ mm is also considered. As also can be seen from Fig. 4.6, even if there is no total internal reflection at the large scatter angles, the scattered light will diverge quickly, and will be out of the CCD effective detection region.

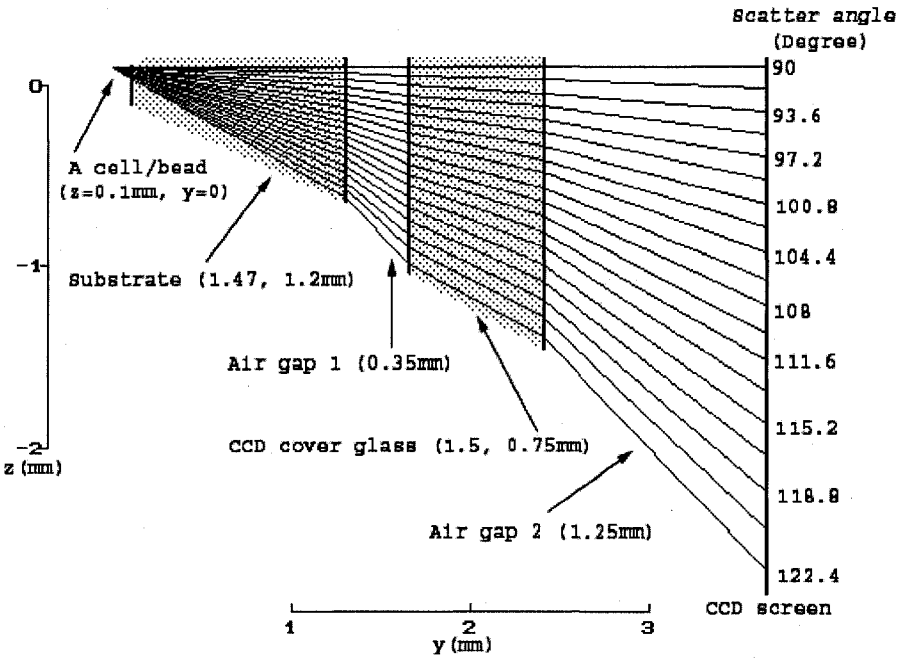

Figure 4.6 BEAM FOUR ray trace of the scattered light in the planar waveguide structure. The side-scattered light ($\geq 90^0$) is shown here in the *yz* plane.

As shown in Fig. 4.6, the BEAM FOUR ray trace gives the position of the projected light on the CCD screen (4.6mm along z) as a function of the polar angle (angle between the light ray direction and the $+z$ direction) from a point source. Mie mapping simulations were also performed with the same configuration as shown in Fig. 4.6. Figure 4.7 shows the comparison between the Mie mapping results and the BEAM FOUR ray trace results. The circles denote the BEAM FOUR ray trace results, while the crosses show the results of my Mie mapping simulations. The Mie mapping simulation results fit well with the BEAM FOUR ray trace results (uncertainty less than 0.001mm). At each interface, Equations (4.8) are applied for intensity transfer. Thus the Mie mapping simulation can give the spatial distribution of the scattered light intensity on the CCD screen in terms of scatter polar angle and position on CCD.

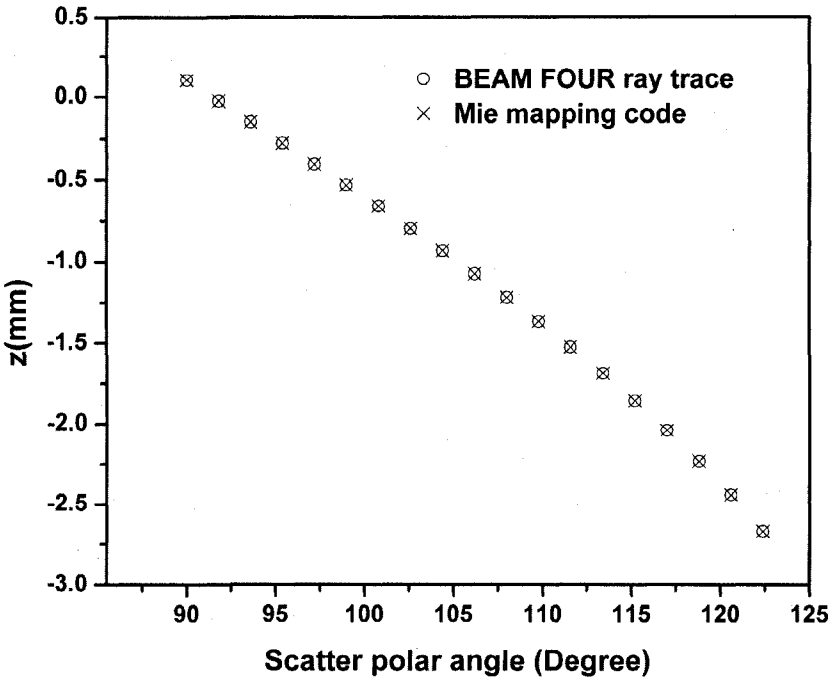

Figure 4.7 Comparison of the BEAM FOUR ray trace results and the Mie mapping simulation results. The positions on the CCD (z axis) are plotted against the scatter polar angle.

4.3.3 Mie scatter spectra in the waveguide cytometer

The Mie mapping simulation maps the calculated light distribution onto the plane CCD in the multilayer planar waveguide structure. Figure 4.8 shows the Mie simulation intensities versus polar angle for different spherical cells. The spherical cells have different diameters and refractive indices. The incident wavelength is 632.8nm, and the surrounding medium has a refractive index of 1.334. Note that intensity variations of several orders of magnitude are obtained among the three cases. Figure 4.8 also shows that changes in the scatterer size and refractive index will change the scatter spectra.

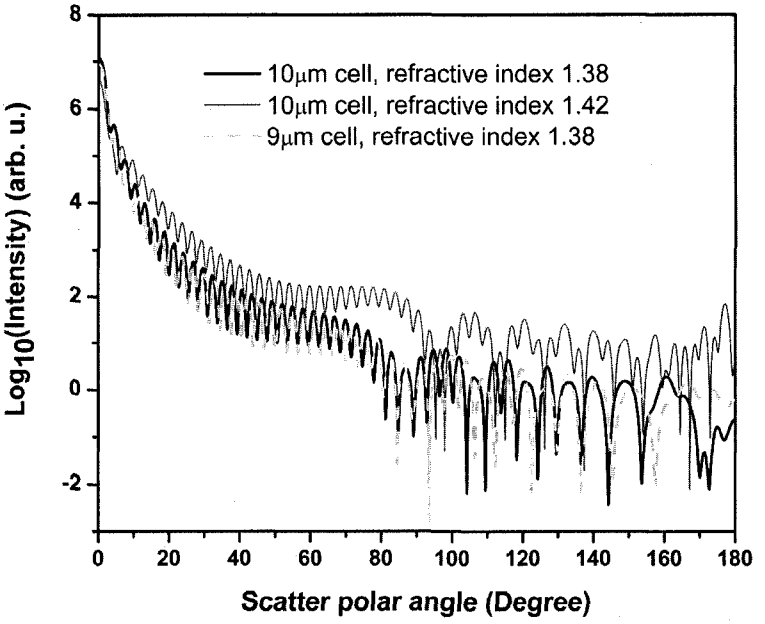

Figure 4.8 Mie simulation results for scatterers with different sizes and refractive indices. The scattered light shown here is in the polar angle range from $0\sim180^0$.

The Mie simulations results as shown in Fig. 4.8 are mapped onto the CCD screen by using the Mie mapping simulation. The scatterer is assumed to be centered at the origin as shown in Fig. 4.1. The constants for the layer structures are the same as for the BEAM FOUR ray trace. Figure 4.9(a) shows the Mie mapping results for the different cell models. Here in Fig. 4.9 we consider only the multilayers between the scatterer and the CCD screen (Fig. 4.1) in order to show the multiple refection effects. There are obvious differences between the cell modes with diameters of 9μm and 10μm (with a constant refractive index 1.38), and between the cell models with a refractive index of 1.38 and 1.42 (with a constant diameter of 10μm). The linear Mie intensities versus the spatial location in the CCD are shown in Fig. 4.9(a) (compared with logarithm results as shown in Fig. 4.8), where the CCD size along z axis is 4.6mm. Another difference between Fig. 4.8 and Fig. 4.9(a) is that Fig. 4.9(a) shows the scattered intensity distribution in the side-scatter angular range of $61\sim119^0$.

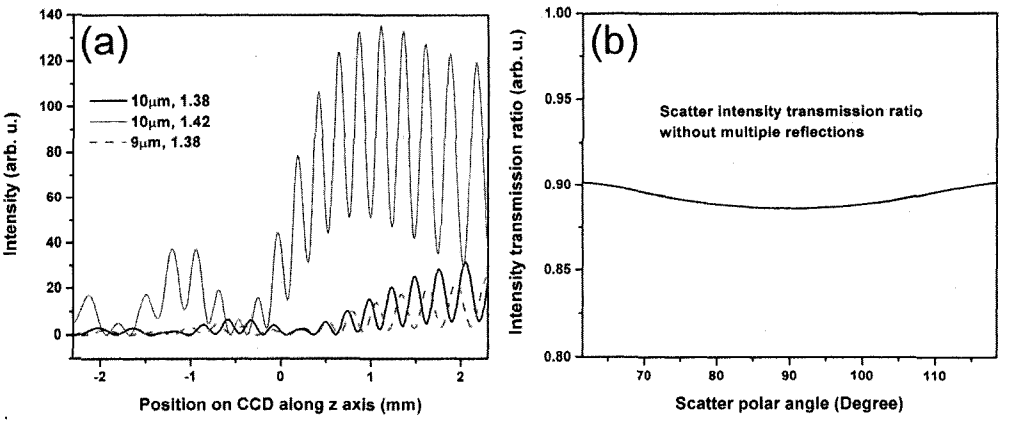

Figure 4.9 Mapping the Mie results onto a CCD screen after the multilayers.

In the Mie mapping code, we do not account for the multiple reflections. To show what fraction of the incident light intensity will be transmitted by the multilayered structure without considering the multiple reflections, we take the 10μm cell (refractive index 1.38) far field Mie intensity as shown in Fig. 4.8, and calculate its intensity after the multilayer propagation using our Mie mapping code. The intensity transmission ratio is defined as the transmitted intensity to the incident scattered light intensity at any given polar angle, as shown in Fig. 4.9(b). From Fig. 4.9(b), we find that about 90% of the scattered light intensity will be transmitted without multiple reflections. The multiple reflections only account for around 10% of the incident intensity. For this smaller amount of light, some will be blocked by the coated Al and some will be out of the CCD detection angular range. Thus we assume that the multiple reflections at different interfaces in the multilayer structures do not significantly alter the mapping of the scattered light intensity.

In the current experiments, the range of the scatter angle θ that can be recorded is determined by the height of the micro-channel relative to the diameter of the observation window, the CCD effective screen size (4.6mm by 4.0mm), and the integrated waveguide structure as shown in Fig. 4.1. Each layer shown in Fig. 4.1 has a tolerance in thickness. For example, the Borofloat glass slide substrate has a specified thickness of 1.1 ± 0.1mm, and the air gap "2" has a

specified thickness of 1.2 ± 0.15mm. In order to account for the tolerances of each layer in the waveguide structure, we assume only the air gap "1" is varied for simplification and assume the other layers have constant thickness. The constants used for the different layers in the planar waveguide structure are shown in Fig. 4.6. As will be described later in this chapter, the experimental results fit well with an air gap "1" of thickness 350~550μm. If not otherwise specified, the air gap "1" thickness used is 550μm in the following analysis. From here on, we consider the light intensity cosine dependence on the incident angle to the CCD surface and the high CCD dielectric constant (refractive index 1.39), for the comparisons with experimental results. In Fig. 4.10 we give a sample calculation for a 9.6μm polystyrene bead (refractive index 1.591) at $z_0 = 0$ (as shown in Fig. 4.1) in a surrounding medium of filtered water (refractive index 1.334), illuminated by a laser with a wavelength of 0.6328μm. Figure 4.10(a) shows the scattered intensity distribution on the CCD screen versus the scatter angle θ. Figure 4.10(b) gives the relationship between the position on CCD and the scatter polar angle. The relationship between the position on CCD and the scatter polar angle is not linear, and this relationship is determined by the integrated waveguide structure - it is the same for all the polystyrene beads used in this study. From Fig. 4.10(b), an angular resolution of approximately 0.09^0 (420 pixels in the angular range 63~99.6 degrees) for the light scattering measurements can be achieved in our integrated waveguide cytometer. Figure 4.10 shows only the scattering angular range that will be considered in detail in the following study from 63^0 to 100^0, which corresponds to approximately 3mm on the CCD.

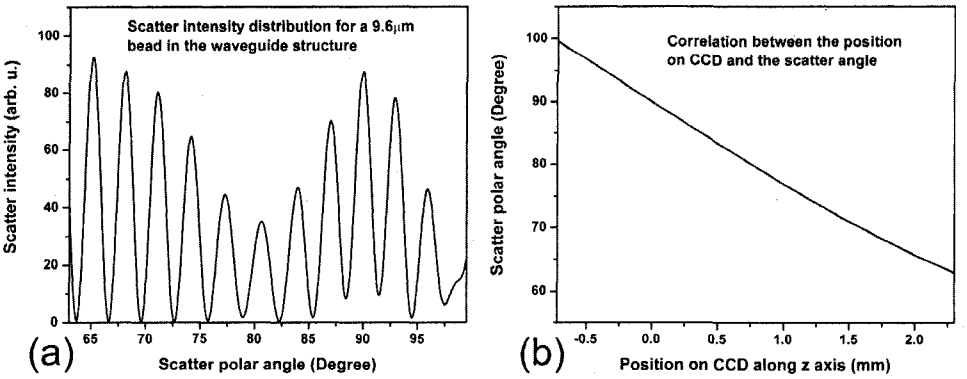

Figure 4.10 Mie simulation results for scattering from a polystyrene bead on the CCD screen. (a), angular distribution of the scattered intensity from a 9.6μm polystyrene bead on the CCD screen. (b), the correlation between the position on CCD and the scatter polar angle for the integrated waveguide structure used in this study.

4.4 2D light scattering patterns from polystyrene beads

4.4.1 Determination of the location of 90^0 scatter

The polystyrene beads used in this study included 4μm and 9.6μm diameter (Interfacial Dynamics Corp.), and 15μm and 20μm diameter (Fluka, Sigma-Aldrich) beads. The beads were in suspension in filtered water (0.8μm filter, Millipore Corp.), which was diluted to a concentration of ~2000 beads/ml and sonicated for 2 minutes. The well diluted bead solution made single bead observations in the observation window area possible. The solution was then pumped into the channel which was pre-filled with filtered water by using a syringe pump. The observation window (as shown in Fig. 4.1) was 400 microns in diameter. Once the system was in good micro alignment (ideally, the observation is projected right onto the center of the CCD although experimentally there might be an offset of several hundred microns), we focused the microscope on the observation window. Positive pressure was applied to induce flow along the $+z$ direction until a single scatterer was seen in the observation window. The micro-size beads were immobilized in the observation window area by using the method described in Chapter 3. Knowledge of the scatterer position relative to the detector

enables one to determine whether the scattered light intensity distribution corresponds to forward, side or backward scattering.

After positioning a microbead in the observation window using the digital camera mounted on top of the microscope, 2D scatter patterns were taken by using the CCD detector located beneath the microchip (more details were discussed in Chapter 3). In Figs. 4.11(a) and (b) the arrow indicates the direction of the mode propagation, which is the same direction as the flow in the channel. Note that the flow and mode propagation directions obtained from the camera (Figs. 4.11(a) and (b)) are opposite to those obtained from the CCD (Figs. 4.11(a') and (b')). As the bead entered the observation window area from right to left, the defocused scatter images as shown in Figs. 4.11(a) and (b) were obtained.

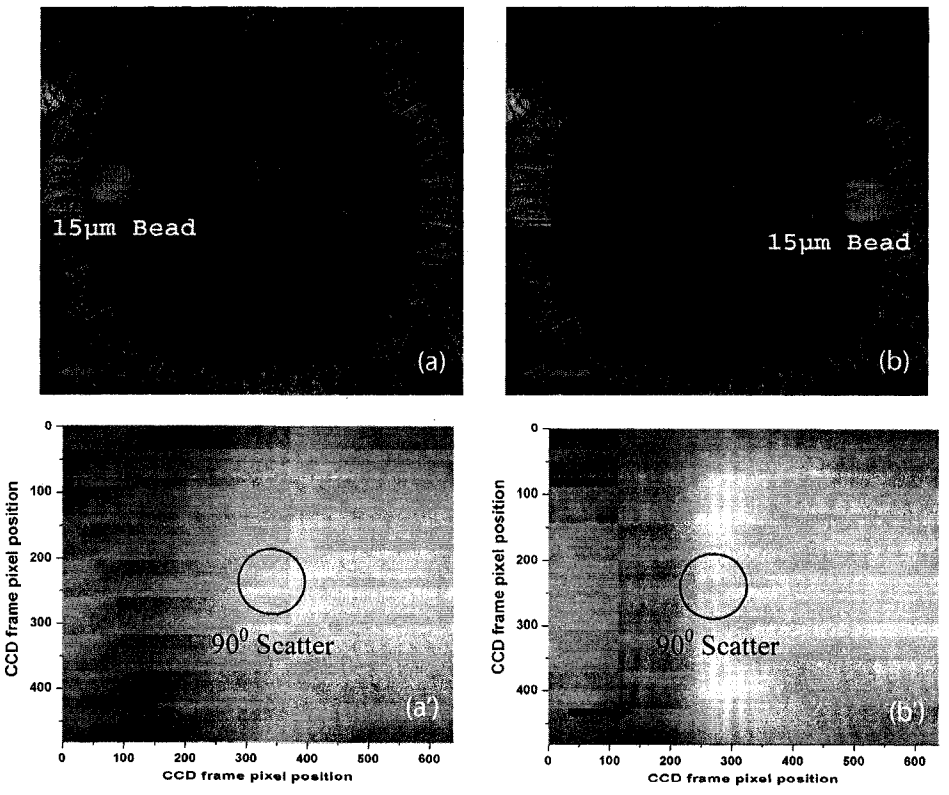

Figure 4.11 Identifying the location of 90^0 scattering in our system. Figures (a) and (b) are the defocused scatter images obtained from a digital camera mounted on the top of the microscope, (a') and (b') are the 2D scatter patterns obtained from the CCD beneath the

microchip. The arrows show the direction of waveguide mode propagation. The center of the circles indicates the 90^0 scatter locations.

A 2D ray trace of the scattered light from a homogenous spherical scatterer is illustrated as in Fig. 4.12. The scattered light into the space forms different cones, while the scatterer sits at the vertex of the cones. The intersection of the cones with the CCD plane gives rise to a series of hyperbolas with varying curvatures. The 90^0 scatter will give vertical bands as shown in Fig. 4.12. The forward scatter gives hyperbolic fringes open to the $+z$ direction ($<90^0$), while the backward scatter gives hyperbolic fringes open to the $-z$ direction ($>90^0$). These features are shown in Figs. 4.11(a') and (b') experimentally. When the defocused image shows the bead at the right side, as in Fig. 4.11(b), its 90^0 scatter in Fig. 4.11(b') is centered to the left side of the CCD frame. When the defocused image shows the bead at the left side, as in Fig. 4.11(a), its 90^0 scatter in Fig. 4.11(a') is centered to the right side of the frame. In Fig. 4.11(a') the 90^0 scatter is centered about pixel column 340, while in Fig. 4.11(b'), the 90^0 scatter is centered about pixel column 290. This 50 pixel difference corresponds to a distance of 0.35mm, which is approximately the distance that the bead has traveled from Fig. 4.11(b) to Fig. 4.11(a). In the analysis that follows, the 90^0 scatter location in the 2D scatter patterns is determined by using the above method.

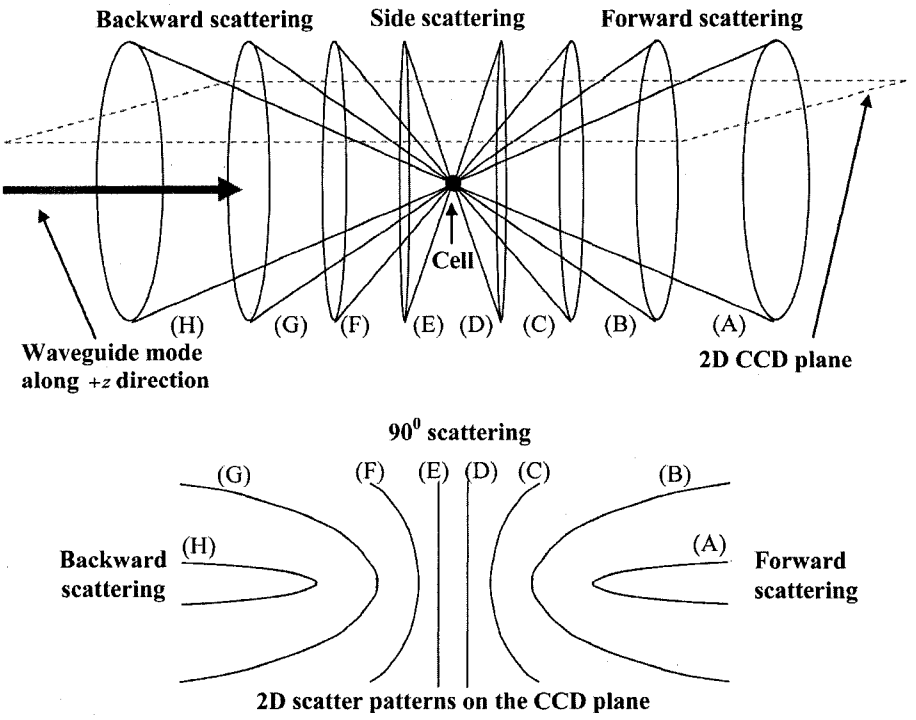

Figure 4.12 Illustration of the 2D scatter pattern onto a plane CCD. As shown here are the representative 2D scatter patterns of forward scattering, side scattering and backward scattering.

4.4.2 High resolution 2D side-scatter patterns

Figures 4.13(a) to (d) are the defocused scatter images taken by using a digital camera for different size polystyrene beads. Clear fringes are obtained which show that the bead is stationary over a time period of 1/4s. For the defocused scatter patterns shown in Fig. 4.13, the bigger the scatterer size, the greater are the numbers of the fringes detected. This information helps one to infer the size of the bead in the fluidic flow.

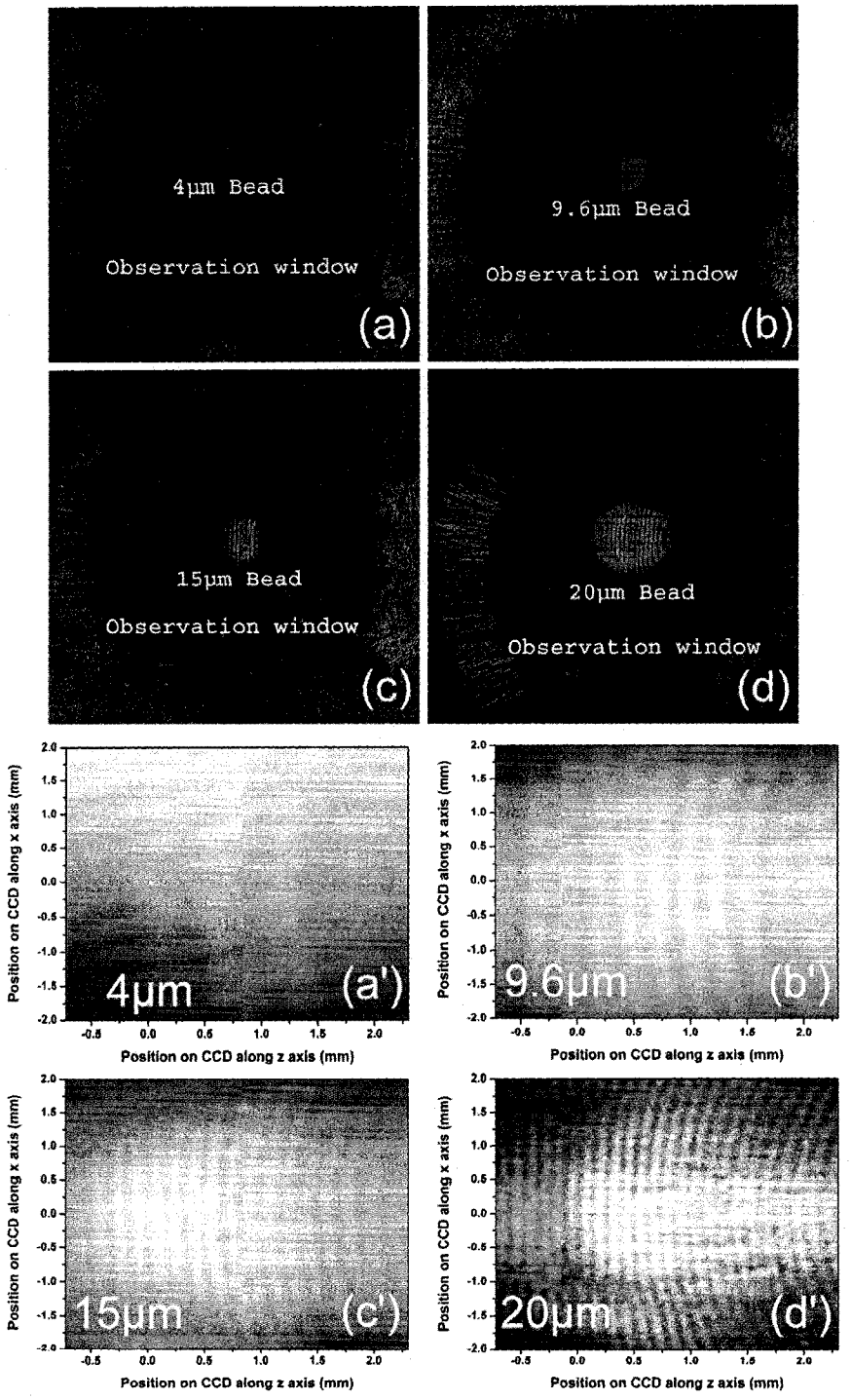

Figure 4.13 2D scatter patterns from different size immobilized beads. (a), (b), (c) and (d) are the defocused scatter images for 4μm, 9.6μm, 15μm and 20μm beads, respectively. The dark circular area in (a), (b), (c) and (d) is the observation window under the

microscope. 2D high resolution scatter patterns are shown in Figs. (a') to (d') for the 4μm, 9.6μm, 15μm and 20μm beads, respectively.

The high resolution 2D scatter patterns obtained by using a CCD array for polystyrene beads for sizes ranging from 4μm to 20μm are shown in Figs. 4.13(a') to (d'). We refer to high resolution images as those with a greater number of observable fringes as compared with the defocused scatter images of the same bead. These high resolution 2D scatter patterns contain more information about the scatterers as compared with the 1D scatter intensity distribution obtained in light scattering measurements. In this report, we only explore the 2D features to determine the position for 90^0 scatter and the position for an azimuth angle $\varphi = 90^0$. However we believe that the 2D scatter patterns can be used to provide a better understanding of the light scattering problems involving single biological cells.

4.5 Wide angle comparisons of experimental light scattering spectra with Mie theory

In order to compare the experimental results and Mie simulation results, experimental scatter patterns in Figs. 4.13(a') to (d') are scanned for 420 pixels horizontally (angular range 63^0~99.6^0, determined by the 90^0 scatter method), and averaged over 3 pixels vertically (pixel 239 to pixel 241). Pixel (0, 0) is at the upper left corner, and pixel (419, 479) is at the lower right corner. Following the ray tracing procedure depicted in Fig. 4.12, the 2D scatter pattern of a bead obtained from the CCD will be symmetrical about the azimuth angle $\varphi = 90^0$. This property is exhibited by the experimental results in Figs. 4.13(a') to (d'). Thus the vertically averaged results from pixel 239 to pixel 241 give the scatter intensity distribution around the azimuth angle $\varphi = 90^0$ ($x = 0$ mm). As the waveguide mode is polarized in the x direction (shown in Fig. 4.1), the scan of the measured pattern gives the perpendicular polarization scatter results.

Wide angle comparisons between Mie simulation results and the experimental results are now given in the space domain. Figures 4.14(a) and (b) show the

representative comparisons in the space domain for 9.6μm and 15μm beads (Figs. 4.13(b') and (c')), respectively. We obtained 11 peaks for 9.6μm beads and 17 peaks for 15μm beads both from Mie theory simulations and from experimental results. The peak locations match well between Mie simulation results and experimental results for both the 9.6μm and the 15μm beads, especially in the position range 0~2.3mm, which is in the angular range of 63^0~90^0 (according to Fig. 4.10(b)). We apply a Fourier high pass filter removing spatial frequencies lower than 0.5 (1/mm) on the experimental results in Figs. 4.14(a) and (b). These low frequency components are from the experimental bumps. This can be explained as follows. We assume the background light sources are many single small scatterers in the microfluidics channel. These small scatterers can be treated as point light sources (diameter far less than the distance to the CCD screen). Most of these scatterers are in the observation window area, thus can be assumed to be above the center area of the CCD. The light intensity from a point source received by a plane CCD surface is proportional to $\cos(\theta)$, where θ is the incident angle to the CCD surface. The CCD center area receives more intensity compared to the CCD edges, causing the experimental bumps.

The filtered experimental results are shown in Figs. 4.14(a) and (b) as solid lines, which show that the experimental bumps can be removed by filtering out smallest frequency components 0~0.5 (1/mm) in the Fourier domain. The filtered experimental results give better comparisons with the Mie simulation results. The good agreements between the peak numbers and peak positions in the experimental and theoretical spectra for both 9.6μm and 15μm beads demonstrated in Figs. 4.14(a) and (b) also confirm the effectiveness of our method for determining the location of 90^0 scatter in the 2D scatter patterns.

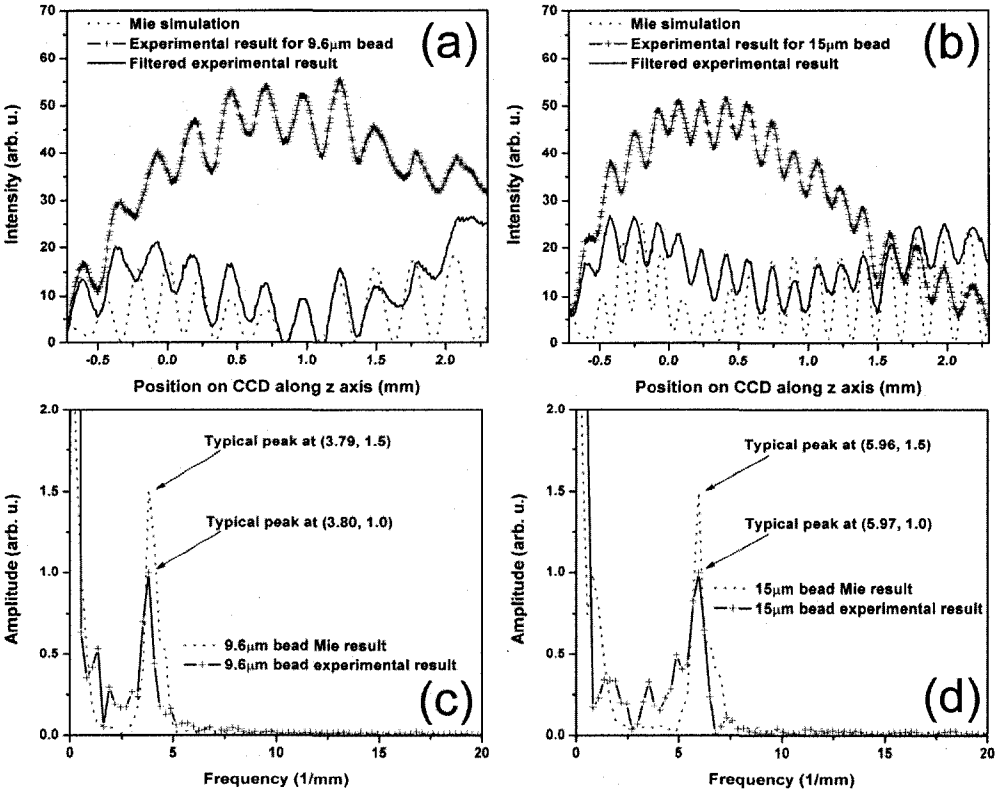

Figure 4.14 Wide angle comparisons between experimental and Mie simulation results. Figures (a) and (b) show the wide angle comparisons between Mie simulation and experimental results. The dotted line shows the Mie simulation results, the solid line with plus signs shows the experimental results, and the solid line shows the Fourier filtered results. Figures (c) and (d) show the comparisons in the Fourier domain for both 9.6 and 15μm bead results. The Fourier spectra are normalized to have typical peak amplitudes of 1.5 and 1.0 for the Mie simulation and experimental results, respectively.

Because the angular intensity distribution of the Mie results for any scatterer has an oscillatory distribution,[20, 21] we explore the application of Fourier transforms on both the Mie simulation results and the experimental results and perform wide angle comparisons in Fourier domain. Figures 4.14(c) and (d) show the representative comparisons in the Fourier domain for both 9.6μm and 15μm beads (frequency components greater than 20 (1/mm) are with very small amplitudes and not shown here), respectively. The typical peak for the experimental result was determined as the highest frequency peak from the dominant part of the full Fourier spectra. As there is no single scatterer in the

medium that is larger than the bead, the amplitudes of the higher frequency components than this typical peak frequency are significantly smaller. The comparisons show that the 9.6μm bead has a typical peak located at 3.79 (1/mm) both from Mie simulations and experimental results, and 5.97 (1/mm) for the 15μm bead. In Fig. 4.14, the Fourier transforms of the Mie simulation results give only one dominant peak in the whole Fourier spectrum for each size of beads. Thus the sizes can be estimated by the locations of this dominant peak. These typical peaks (Figs. 4.14(c) and (d)) in the Fourier domain correspond to the total peak numbers found from Figs. 4.14(a) and (b) in the space domain, and increase with the particle sizes. In Figs. 4.14(c) and (d), good agreement is obtained for the typical peak positions between the Mie theory and experimental results.

4.6 A Fourier method for quick micro-size differentiation

The above study shows that the oscillatory property of the scattered intensity distribution will give certain peaks in the frequency domain. Applying this principle to beads ranging from 4 to 20μm in diameter, a Fourier method for quick size differentiation is developed. Compared with an analysis based on matching the fringes between experimental and theoretical simulation results, the Fourier analysis offers a quicker method for size differentiation. The Fourier method developed here can potentially be useful for the real time characterization of cell samples in clinics.

The Fourier transform was applied to all the Mie simulations and the experimental results for the polystyrene beads ranging in size 4μm to 20μm. In Fig. 4.15, the open squares and triangles indicate the Fourier results for the Mie simulations of the beads with an air gap "1" (see Fig. 4.1) of thickness 350 and 550μm, respectively. The cross signs are the Fourier results for the experimental patterns as shown in Fig. 4.13. Referring back to Fig. 4.1, the thicknesses of air gap "1" and air gap "2" play important roles as the light travels from an optically dense medium into air. As shown in Fig. 4.15, an air gap thickness of 350μm

gives higher peak frequency values as compared with an air gap thickness of 550μm.

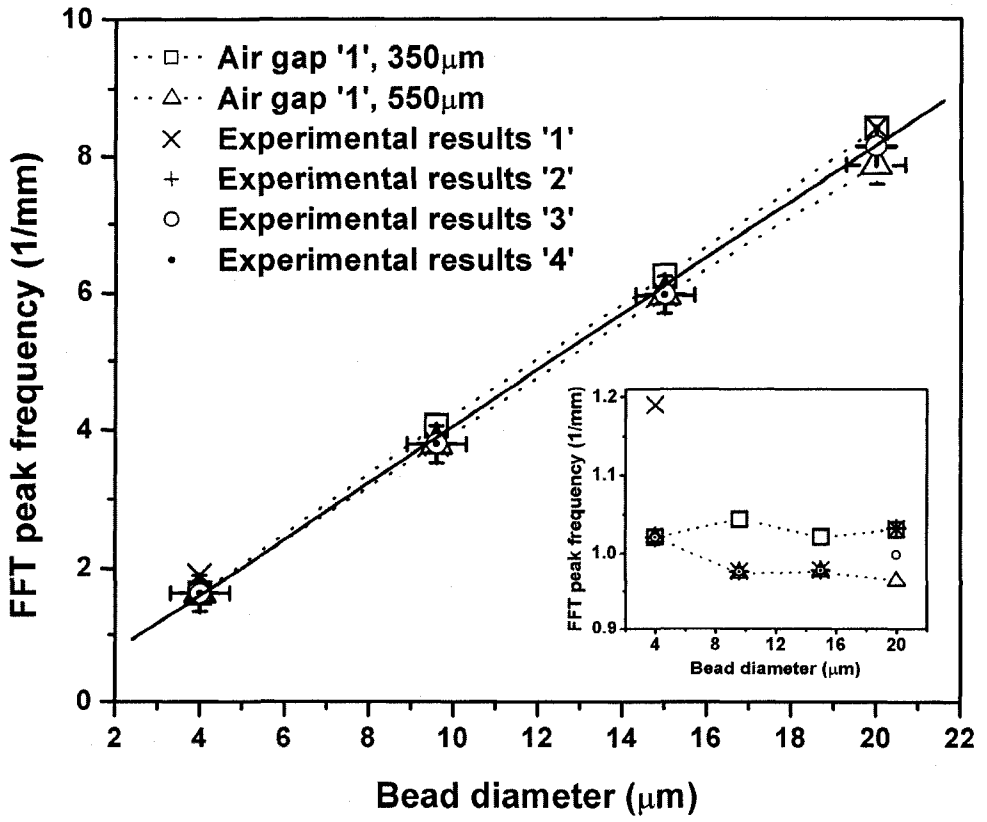

Figure 4.15 FFT method for quick micro-size differentiation. Fourier peaks of the experimental and Mie simulation results for 4, 9.6, 15, and 20μm beads are shown. The open squares and triangles are the Mie simulation results for the four different sizes of beads, for an air gap "1" thickness of 350μm and 550μm, respectively. The inset shows the experimental and theoretical results normalized to the calibration values.

The Fourier analysis was also performed on different sets of experimental results (Table 4.1). Each set of the experimental results includes 4μm, 9.6μm, 15μm and 20μm beads. The Fourier peak frequencies of the other three sets of experimental scatter patterns are denoted as plus signs, open circles and solid dots in Fig. 4.15. The 512-point Fourier transform that has been used has a resolution of approximately 0.27 in frequency (1/mm), which gives an uncertainty of approximately 0.7μm for the size estimations (from Figs. 4.14(c) and (d)), shown

as error bars in Fig. 4.15. The Fourier peaks of the experimental results shown in Fig. 4.15 fall within this uncertainty range. The solid line in Fig. 4.15 is a linear regression of all the experimental results. This linear curve can be used to perform size calibrations independent of Mie theory. To illustrate differences between data points shown in Fig. 4.15, we have normalized them by the calibration values from the linear curve. The normalized data are shown as an inset in Fig. 4.15. Despite differences that result from the air gap "1" thickness, Fig. 4.15 shows the effectiveness of the Fourier method for size differentiation.

Frequency (1/mm) / Bead size	Mie (air gap 350μm)	Mie (air gap 550μm)	Experimental Results '1'	Experimental Results '2'	Experimental Results '3'	Experimental Results '4'
4μm	1.63	1.63	1.90	1.63	1.63	1.63
9.6μm	4.06	3.79	3.80	3.80	3.80	3.80
15μm	6.23	5.96	5.97	5.97	5.97	5.97
20μm	8.40	7.86	8.41	8.14	8.14	8.41

Table 4.1 Mie simulation and experimental results Fourier peak frequencies for different size beads.

The above analysis performs a FFT on the scatter spectra in the side-scatter range. The FFT analysis in different angular ranges for a 10μm cell with a refractive index of 1.38 is shown in Fig. 4.16. The FFT is performed on the logarithm intensity distribution as shown in Fig. 4.8. The different angular ranges chosen here have the same 512 points. Fig. 4.16 shows that forward scattered light has the sharpest and highest typical peak frequency, while the backward scattered light has the broadest and lowest typical peak frequency. Although we shown that the side-scattered light can be used to perform effective micro-size differentiation, the results shown in Fig. 4.16 suggest that the forward scattered light can be used for optimal micro-size differentiation based on the Fourier method developed here.

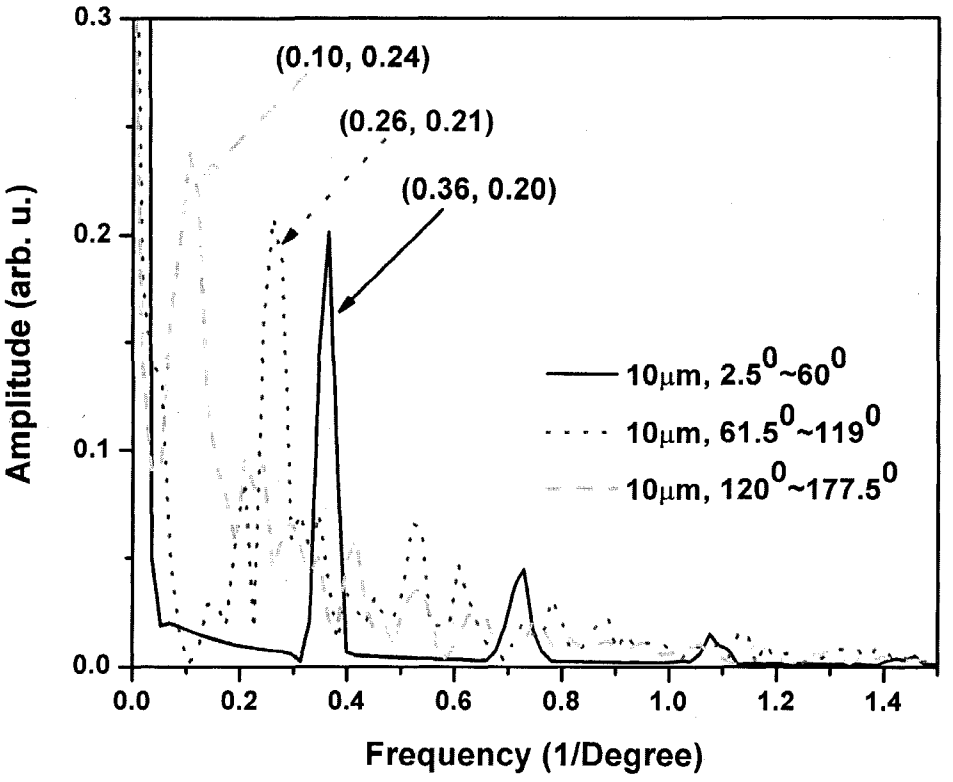

Figure 4.16 Typical Fourier peaks of a single scatterer in different angular ranges. The different angular ranges are chosen to have the same points for the Fourier peaks comparisons.

4.7 Conclusions

The integrated microfluidic waveguide cytometer has a planar structure in terms of the liquid-core waveguide and the CCD detector. A modal analysis of the liquid-core waveguide supports the assumption of plane wave propagation in the microfluidic channel. The use of Mie theory or simulation methods such as the FDTD to validate the experimental results are simplified when such an integrated structure is used. Mie theory spatially distributed intensity is mapped onto the plane CCD screen. The experimental 2D scatter patterns together with the no lens planar optical design ensure a better resolution of the angular dependence of the side-scatter spectra. A Fourier method was developed for quick size

differentiation. The analysis is confirmed by Mie theory simulations of scattering from the homogeneous spherical polystyrene beads used in the experiment.

As an integrated biomedical optics instrument, our 2D cytometer has an important potential application in biological cell diagnostics. We have developed the quantitative Fourier transform based method of size determination of polystyrene beads. Clearly this method could be very efficient in finding out the size of scattering objects, cells or beads, if the Fourier transform of the scattered light angular distribution contains a dominant peak with a finite frequency. This is the case for biological cells without internal structure, for example, isovolumetrically sphered red blood cells.[20] Alternatively, one could consider cells with one large size organelle which has the largest scattering cross-section, such as a nucleus with a large index of refraction, as for example in stem cells.

In this chapter, we extract the 1D spectra from the 2D patterns for the size differentiation of the micro-size polystyrene bead cell mimics. The 2D scatter patterns from biological cells however will contain rich information about the organelles. The method shown here is very useful as a first step in analyzing the 2D scatter patterns. This would allow us to fit and/or remove scatter-pattern effects brought on by microscale features, potentially allowing follow-up analysis of organelles in biological cells.

4.8 References

1. Z. Wang, J. El-Ali, M. Engelund, T. Gotsaed, I. R. Perch-Nielsen, K. B. Mogensen, D. Snakenborg, J. P. Kutter and A. Wolff, "Measurements of scattered light on a microchip flow cytometer with integrated polymer based optical elements," *Lab on a Chip* **4**, 372-377 (2004).

2. K. Singh, X. T. Su, C. G. Liu, C. Capjack, W. Rozmus and C. J. Backhouse, "A miniaturized wide-angle 2D cytometer," *Cytometry Part A* **69A**, 307-315 (2006).

3. J. R. Mourant, J. P. Freyer, A. H. Hielscher, A. A. Eick, D. Shen and T. M. Johnson, "Mechanisms of light scattering from biological cells relevant to noninvasive optical-tissue diagnostics," *Applied Optics* **37**, 3586-3593 (1998).

4. D. Watson, N. Hagen, J. Diver, P. Marchand and M. Chachisvilis, "Elastic light scattering from single cells: Orientational dynamics in optical trap," *Biophysical Journal* **87**, 1298-1306 (2004).

5. K. A. Sem'yanov, P. A. Tarasov, J. T. Soini, A. K. Petrov and V. P. Maltsev, "Calibration-free method to determine the size and hemoglobin concentration of individual red blood cells from light scattering," *Applied Optics* **39**, 5884-5889 (2000).

6. R. M. P. Doornbos, M. Schaeffer, A. G. Hoekstra, P. M. A. Sloot, B. G. deGrooth and J. Greve, "Elastic light-scattering measurements of single biological cells in an optical trap," *Applied Optics* **35**, 729-734 (1996).

7. X. T. Su, K. Singh, C. Capjack, J. Petracek, C. Backhouse and W. Rozmus, "Measurements of light scattering in an integrated microfluidic waveguide cytometer," *Journal of Biomedical Optics* (accepted).

8. J. Petracek and K. Singh, "Determination of leaky modes in planar multilayer waveguides," *IEEE Photonics Technology Letters* **14**, 810-812 (2002).

9. R. E. Smith, S. N. Houdewalter and G. W. Forbes, "Numerical Determination of Planar Wave-Guide Modes Using the Analyticity of the Dispersion-Relation," *Optics Letters* **16**, 1316-1318 (1991).

10. E. Anemogiannis and E. N. Glytsis, "Multilayer Wave-Guides - Efficient Numerical-Analysis of General Structures," *Journal of Lightwave Technology* **10**, 1344-1351 (1992).

11. Y. Z. Lin, J. H. Zhan and S. M. Tseng, "A new method of analyzing the light transmission in leaky and absorbing planar waveguides," *IEEE Photonics Technology Letters* **9**, 1241-1243 (1997).

12. E. Anemogiannis, E. N. Glytsis and T. K. Gaylord, "Determination of guided and leaky modes in lossless and lossy planar multilayer optical waveguides:

Reflection pole method and wavevector density method," *Journal of Lightwave Technology* **17**, 929-941 (1999).

13. J. Chilwell and I. Hodgkinson, "Thin-Films Field-Transfer Matrix-Theory of Planar Multilayer Waveguides and Reflection from Prism-Loaded Waveguides," *Journal of the Optical Society of America a-Optics Image Science and Vision* **1**, 742-753 (1984).

14. L. M. Walpita, "Solutions for Planar Optical Wave-Guide Equations by Selecting Zero Elements in a Characteristic Matrix," *Journal of the Optical Society of America a-Optics Image Science and Vision* **2**, 595-602 (1985).

15. R. P. Brent, *Algorithms for minimization without derivatives*, (Prentice-Hall, Englewood Cliffs, 1973).

16. T. J. Ypma, "Historical development of the Newton-Raphson method," *Siam Review* **37**, 531-551 (1995).

17. P. K. Tien, "Light Waves in Thin Films and Integrated Optics," *Applied Optics* **10**, 2395-2413 (1971).

18. W. T. Grandy, *Scattering of Waves from Large Spheres*, (Cambridge University Press, Cambridge, 2000).

19. E. Hecht, *Optics*, (Addison Wesley Longman, Inc., Reading, 2002).

20. N. Ghosh, P. Buddhiwant, A. Uppal, S. K. Majumder, H. S. Patel and P. K. Gupta, "Simultaneous determination of size and refractive index of red blood cells by light scattering measurements," *Applied Physics Letters* **88**, 084101 (2006).

21. C. M. Sorensen and D. Shi, "Patterns in the ripple structure of Mie scattering," *Journal of the Optical Society of America a-Optics Image Science and Vision* **19**, 122-125 (2002).

Chapter 5

Application of FDTD within the integrated cytometer

5.1 Introduction

Light scattering depends not only on the properties of the scatterer and the surrounding medium (*e.g.* size, shape, refractive index), but also on the properties of the incident wave (*e.g.* polarization, wavelength).[1-3] In the previous chapters, the dependence of the scattered light on the spherical scatterer sizes and refractive indices was studied. Recent research shows significant differences in the propagation of polarized light through biological tissue compared with tissue phantoms.[4] Polarized light has been used to isolate light scattering from epithelial cell nuclei in biological tissue.[5] Experiments have not been performed to study the dependence of light scattering on the polarization (*e.g.* parallel or perpendicular polarization) of the incident laser beam. The reason for this is that most experimental setups have not been designed with the flexibility to be able to perform these tasks.

We have further developed our integrated microfluidic waveguide cytometer motivated by studying the polarization effects on the light scattering from biological cells. As a first step, measurements are made on polystyrene beads as cell mimics. Mie theory[2, 3] can be used to predict the polarization dependence of scattering. For the simulation of light scattering from complex biological cells, a

numerical method such as the FDTD method has to be used in order to obtain accurate results. However there is lack of comparisons between experimental results with 3D FDTD simulations. One difficulty is to transform the spatially distributed 3D FDTD results through an experimental apparatus onto a detector. The design of our integrated cytometer dramatically simplifies this procedure.[6] The application of the FDTD method in the integrated waveguide cytometer is introduced in this chapter. FDTD simulations of biological cell models in the waveguide cytometer are also performed. The randomly distributed mitochondria in biological cells have been shown to break the azimuthal symmetry of the 2D light scattering patterns. This can be of interest as the recent study by Yu *et al* has shown that the cancerous tissue exhibits much greater asymmetry in the azimuthal dependence of the scattered pattern than the healthy tissue.[7]

This chapter is based on a journal paper that is in preparation by X. T. Su, *et al*.[8]

5.2 Measurements of the dependence of light scattering on the polarization of the incident laser

The integrated waveguide cytometer as discussed in Chapter 3 is further developed (see Fig. 5.1(a)) for studying of the polarization dependence of the scattered light on. A polarizer holder (Waveplate/Polarizer holder, 55010, Edmund Optics) is used as shown in Fig. 5.1(a). The polarizer can be rotated in the azimuth angle φ (Fig. 5.1(b)) in the range $0\sim360^0$. Compared with the experiments performed in Chapter 4, the illumination laser used here is a randomly polarized HeNe laser (632.8nm, 1144, JDS Uniphase). The laser beam is prism-coupled (BK7 prism, Edmund Industrial Optics) into the microfluidic channel. As can be seen from Fig. 5.1, without the polarizer the incident laser beam will be coupled into the liquid-core waveguide with a random polarization angle φ. The polarizer can be used to give a specific polarization of the incident laser.

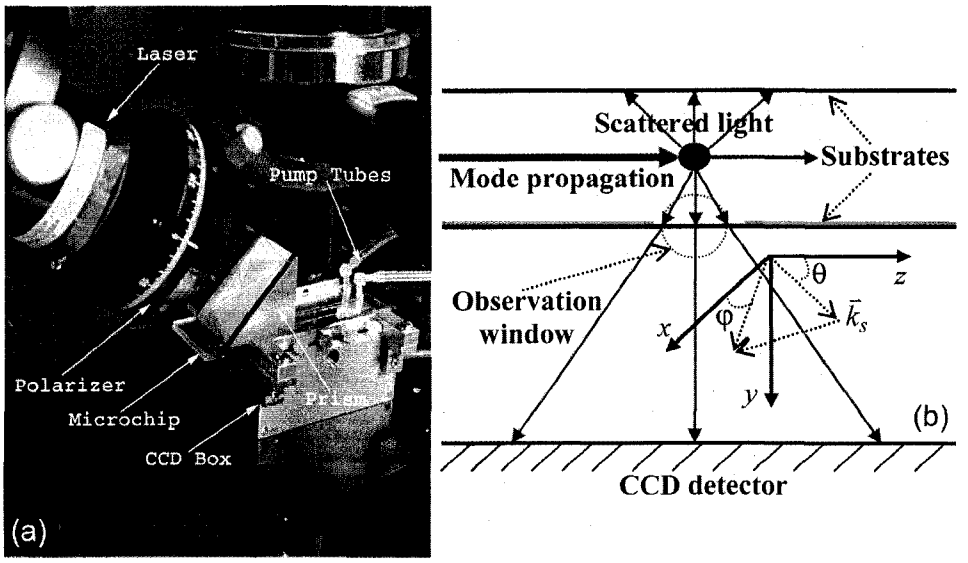

Figure 5.1 Experimental setup for measurement of the polarization dependence and the light scattering geometry. (a), experimental setup. (b), light scattering geometry. The mode in the waveguide propagates along the $+z$ direction. The scattered light has a polar angle θ, and an azimuth angle φ. The polarization angle is defined as azimuth angle φ.

The polarization dependent scattering was measured from 15μm and 20μm diameter polystyrene beads (Fluka, Sigma-Aldrich, refractive index 1.591). The bead solutions were prepared as described in Chapter 4. While a single bead was immobilized in the micro observation window area, the polarizer was rotated to change the incident beam polarization angle φ. The 2D light scattering patterns were obtained with the CCD detector for different incident beam polarizations. The CCD integration time was 1/15 second. An expanded description of the operation of the integrated cytometer can be found in Chapter 4. Figure 5.2 gives the 2D light scattering patterns obtained for 15μm and 20μm diameter beads at different polarization angles. Figures 5.2(a) and (b) are the scatter patterns at $\varphi = 90^0$ for 15μm bead and 20μm beads, respectively. Figures 5.2(c) and (d) are the scatter patterns at $\varphi = 0^0$ for 15μm bead and 20μm beads, respectively. Figure 5.2 shows that the light scattering pattern at $\varphi = 0^0$ gives clearer fringes compared with those at $\varphi = 90^0$.

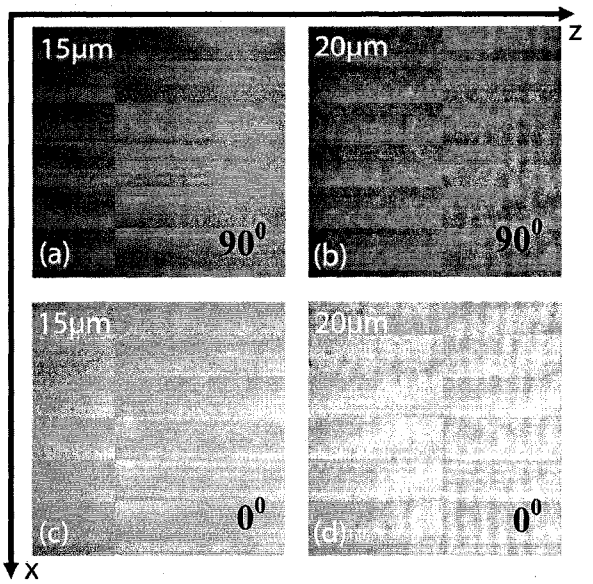

Figure 5.2 2D Light scattering patterns at different polarizations for different size polystyrene beads. Figures (a) and (b) are the scatter patterns at a polarization angle of 90^0 for a 15μm bead and a 20μm bead, respectively. Figures (c) and (d) are the scatter patterns at a polarization angle of 0^0 for a 15μm bead and a 20μm bead, respectively. All the figures (a) to (d) are illuminated by a 632.8nm laser.

5.3 Analysis of the polarization dependence of the scatter patterns

All the scatter patterns shown in Fig. 5.2 have sizes approximately 1.84mm horizontally by 2.1mm vertically on the CCD. The scatter patterns have 256 pixels horizontally and 256 pixels vertically. The (0, 0) pixel is at the left upper corner, and the (255, 255) pixel is at the right lower corner. According to the 90^0 polar angle determination method developed in Chapter 4 and the fact that the 2D light scattering patterns for homogeneous spherical particles are symmetric about azimuth angle $\varphi = 90^0$, we have determined that the pixel at (128, 128) corresponds to $\theta = 90^0$, and $\varphi = 90^0$. The 256 horizontal pixels of the scatter patterns in Fig. 5.2 corresponds to the polar angle scatter range $78\sim102^0$ as determined by the Mie mapping code in the multilayer waveguide transformation.

In order to show the differences between the light scattering patterns at 0^0 and 90^0, representative cross section scans of the 20μm bead light scattering patterns (as shown in Fig. 5.2(b) and (d)) are performed. A scan of Fig. 5.2(b) from 0~255 pixels horizontally and averaged from 127~129 vertically gives the parallel polarization scatter spectra, shown as the dotted line in Fig. 5.3. A scan of Fig. 5.2(d) from 0~255 pixels horizontally and averaged from 127~129 vertically gives the perpendicular polarization scatter spectra, shown as the solid line in Fig. 5.3. Figure 5.3 shows quantitatively the difference between the light scattering spectra at different polarization angles for a 20μm bead.

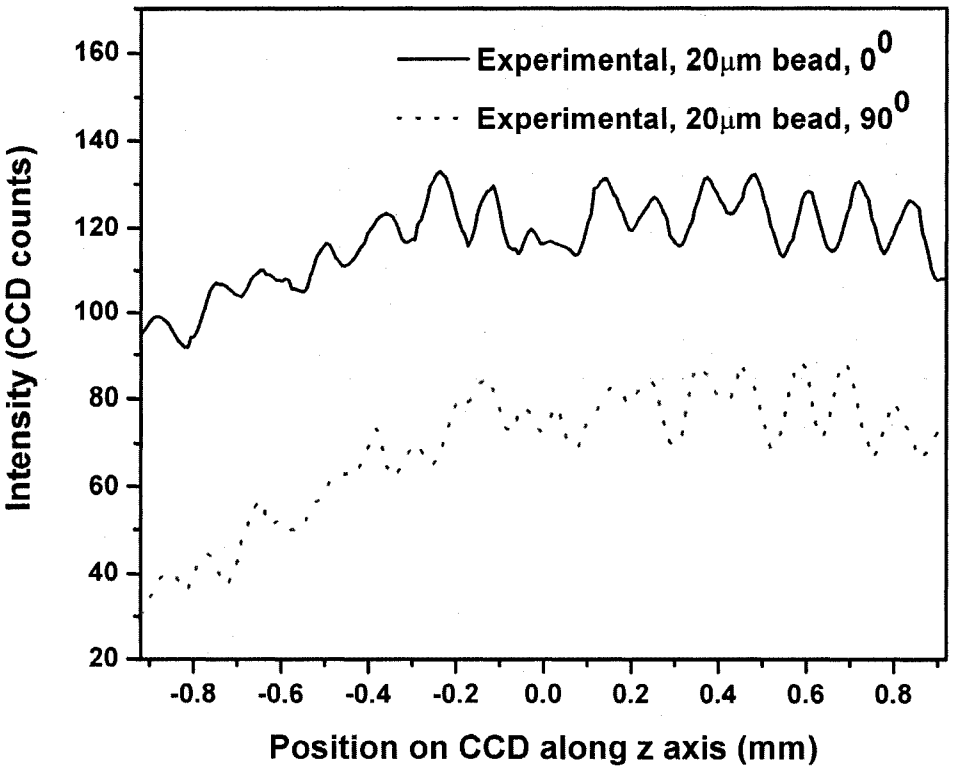

Figure 5.3 Representative light scattering spectra for a 20μm bead at different polarization angles.

In Chapter 4, a Fourier analysis has been used for size differentiation. Fourier transforms are also performed here to show the dependence of the light scattering on the incident laser polarization angles. Figure 5.4 shows the Fourier transforms

of the 20μm bead light scattering spectra as shown in Fig. 5.3. From Figure 5.4, the Fourier spectra of a 20μm bead at a polarization angle of 0^0 (perpendicular polarization) has a typical peak at frequency 8.14 (1/mm), which agrees well with the analyses performed in Chapter 4. The differences between the Fourier spectra of a 20μm bead at different polarization angles are distinguishable, as shown in Fig. 5.4.

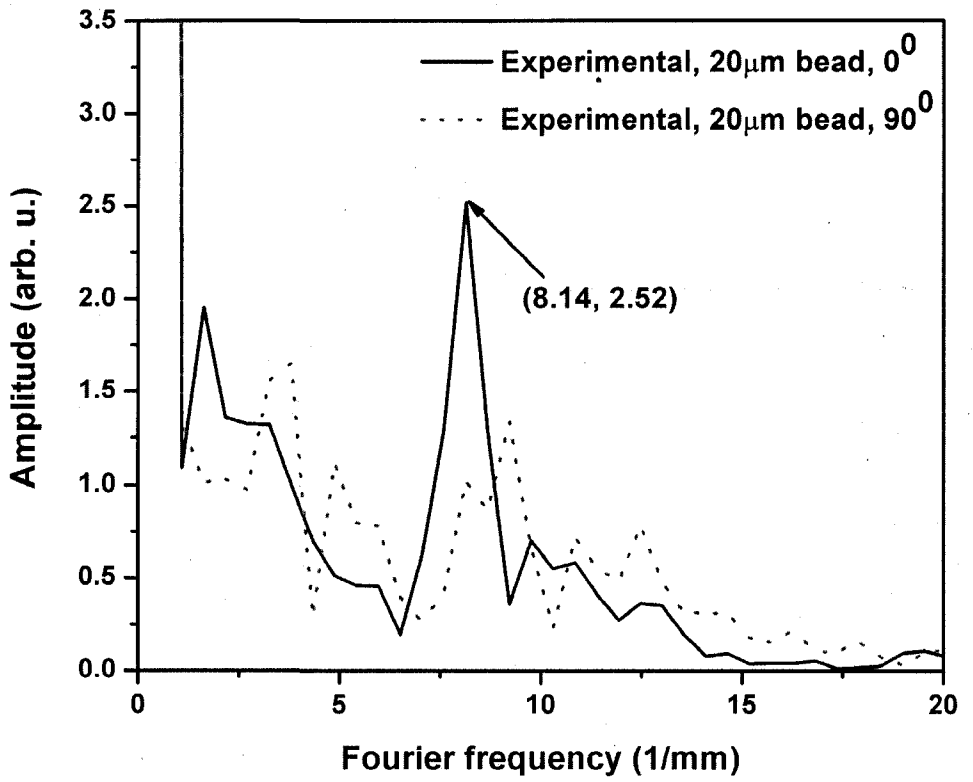

Figure 5.4 Fourier transforms of the 20μm bead light scattering spectra at different polarization angles.

5.4 Application of FDTD simulations to the integrated cytometer

5.4.1 Method to apply the 3D FDTD results onto a plane CCD

The planar waveguide structure and the FDTD geometry that was used to transfer the 3D FDTD results onto a plane CCD are shown in Fig. 5.5. In Fig. 5.5(a), G1 is a layer of Fisher glass slide (refractive index 1.5, thickness 1.0mm), G2 is a layer of Borofloat glass substrate (refractive index 1.47, thickness 1.2mm) and G3 is the CCD cover glass (refractive index 1.5, thickness 0.75mm). There are two air gap layers denoted as Air gap "1" (thickness 0.35mm) and Air gap "2" (thickness 1.25mm). The laser mode propagates along the $+z$ direction and is polarized along the x direction. For a scatterer located at the origin as shown in Fig. 5.5(a), the scattered light will be collected by a CCD detector after crossing the multilayer structure. The illustration of a scattered light ray trace is shown in Fig. 5.5(a) by the arrows.

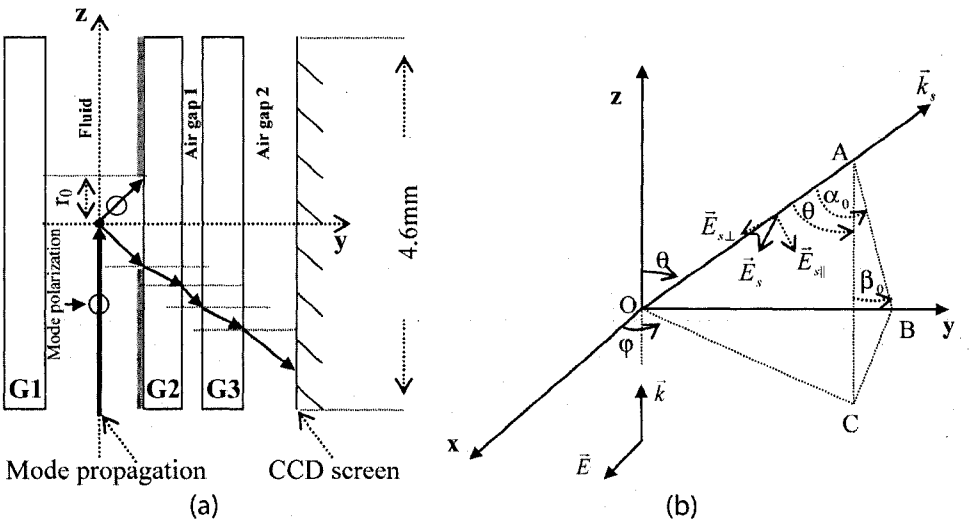

Figure 5.5 Illustrations of the transfer of the FDTD scattered light onto a plane CCD. (a), the waveguide structure contains multilayers. The light scattered by a scatterer in the micro-channel will be collected by a CCD sensor. (b), the geometry to transfer the FDTD results onto a plane CCD. Plane ABC is where the glass slide G2 sits. AC is normal to the plane OBC and OB is normal to the plane ABC.

The FDTD method was used to calculate the scattered intensity from the scatterer located at the origin. In Fig. 5.5(b), the incident laser beam is assumed to propagate along the z direction ($\vec{k}$) and is polarized along the x direction. The scattered light ($\vec{k}_s$) has a polarization ($\vec{E}_s$), which is the same as the incident laser beam.[2]

Geometry calculations in Fig. 5.5 show that,

$$\sin\alpha_0 = \sin\theta \cdot \sin\varphi \tag{5.1}$$

$$\cos\beta_0 = |\cos\theta| / \cos\alpha_0 . \tag{5.2}$$

The incident angle of $\vec{k}_s$ to the plane ABC is,

$$\theta_i = \pi/2 - \alpha_0 . \tag{5.3}$$

And $\vec{E}_s$ in the plane OAB can be decomposed as perpendicular component ($\vec{E}_{s\perp}$) and parallel component ($\vec{E}_{s\parallel}$),

$$\vec{E}_{s\perp} = \vec{E}_s \cdot \cos\beta_0 \tag{5.4}$$

$$\vec{E}_{s\parallel} = \vec{E}_s \cdot \sin\beta_0 . \tag{5.5}$$

The incident scatter intensity to the plane OAB can be decomposed as

$$I_{i\perp} = \frac{c\varepsilon_0}{2}\left|\vec{E}_{s\perp}\right|^2 \tag{5.6}$$

$$I_{i\parallel} = \frac{c\varepsilon_0}{2}\left|\vec{E}_{s\parallel}\right|^2 . \tag{5.7}$$

Since $I_i = \frac{c\varepsilon_0}{2}\left|\vec{E}_s\right|^2$, we have

$$I_{i\perp} = I_i \cdot (\cos\beta_0)^2 \tag{5.8}$$

$$I_{i\parallel} = I_i \cdot (\sin\beta_0)^2 , \tag{5.9}$$

and $I_i = I_{i\perp} + I_{i\parallel}$ is the FDTD scattered intensity calculated at point A.

Using Equations (5.8) and (5.9), the scattered intensity was transformed into the incident intensity at the interface between the fluid and the glass substrate G2. The Fresnel Equations and the transmittance T for the intensity transforms are considered at this interface. The amplitude transmission coefficients of Fresnel

Equations for perpendicular ($t_\perp$) and parallel polarization ($t_\parallel$),[9] respectively, are given as

$$t_\perp = \frac{2\sin\theta_t \cos\theta_i}{\sin(\theta_i + \theta_t)} \tag{5.10}$$

$$t_\parallel = \frac{2\sin\theta_t \cos\theta_i}{\sin(\theta_i + \theta_t)\cos(\theta_i - \theta_t)}, \tag{5.11}$$

where θ_i denotes the incident angle from medium n_i to medium n_t, and θ_t denotes the refracted angle from medium n_i to medium n_t. The following intensity transform is the same as that used with the Mie mapping code described in Chapter 4. For simplicity, only the last step used for the intensity transform is shown here. The transmitted intensity I_t after the interface of the fluid and the glass substrate G2 for perpendicular ($I_{t\perp}$) and parallel polarization ($I_{t\parallel}$) can be written as

$$I_{t\perp} = \frac{I_{i\perp}\cos\theta_i}{\cos\theta_t} T_\perp = \frac{n_t}{n_i} t_\perp^2 I_{i\perp} \tag{5.12}$$

$$I_{t\parallel} = \frac{I_{i\parallel}\cos\theta_i}{\cos\theta_t} T_\parallel = \frac{n_t}{n_i} t_\parallel^2 I_{i\parallel}, \tag{5.13}$$

where $I_t = I_{t\perp} + I_{t\parallel}$. Equations (5.12) and (5.13) are applied at each interface in the waveguide structure to finally transform the scattered intensity onto the CCD plane.

5.4.2 Comparison of FDTD and experimental results for polystyrene beads

Mie analytical results have been used to compare with the polystyrene beads experimental results. The application of FDTD simulation in the integrated cytometer aims for better understanding of light scattering from biological cells. Biological cells however are with irregular shapes and complex inner structures, making it challenging for exact simulations. Our AETHER code has been calibrated with Mie theory.[10] In order to better understand the 2D scatter patterns

of biological cells, as a first step, it is of interest to compare the 2D FDTD simulations with polystyrene bead experimental results.

In the experiments, a HeNe laser (543nm, 5mW, Melles Griot Laser Group) was prism-coupled (BK7 prism, Edmund Industrial Optics) into the waveguide. The polystyrene beads used here are 9.6 μm (Interfacial Dynamics Corp.) and 15μm (Fluka, Sigma-Aldrich) in diameter. While immobilizing a single bead in the observation window area (in Fig. 5.5(a) with a radius of $r_0 = 200\mu m$), a defocused scatter image was taken by using a digital camera, and a 2D scatter pattern was obtained simultaneously by using a CCD detector. More details about how this system works was described in Chapter 4. A plane wave with a wavelength of 543nm is assumed as the illumination source in the FDTD simulations. The polystyrene beads (refractive index 1.591) are in a surrounding medium of water (refractive index 1.334). Using the above developed equations, FDTD simulation scatter intensities were transformed onto a CCD screen.

A comparison between the experimental results and the FDTD simulations are shown in Fig. 5.6. Figures 5.6(a) and (b) show the defocused scatter images from the immobilized 9.6μm and 15μm polystyrene beads, respectively. The integration time used for the digital camera is 1/4s. The experimental scatter patterns obtained by using a CCD array (integration time 1/15s) are shown in Fig. 5.6(c) and (d) for the 9.6μm and 15μm polystyrene beads, respectively. Both Figure 5.6(c) and Fig. 5.6(d) have size of approximately 2mm horizontally and 4mm vertically. Figure 5.6(d) shows a higher frequency for the scatter pattern distribution compared with Fig. 5.6(c). This is true as the bigger the scatterer size, the higher is the frequency of the scattered intensity distribution. The FDTD simulation results for 9.6μm and 15μm polystyrene beads in the waveguide are given as in Fig. 5.6(e) and (f), respectively. Vertical lines are drawn in Fig. 5.6 to compare the experimental and simulation results, and good agreement for both 9.6 and 15μm polystyrene beads are obtained.

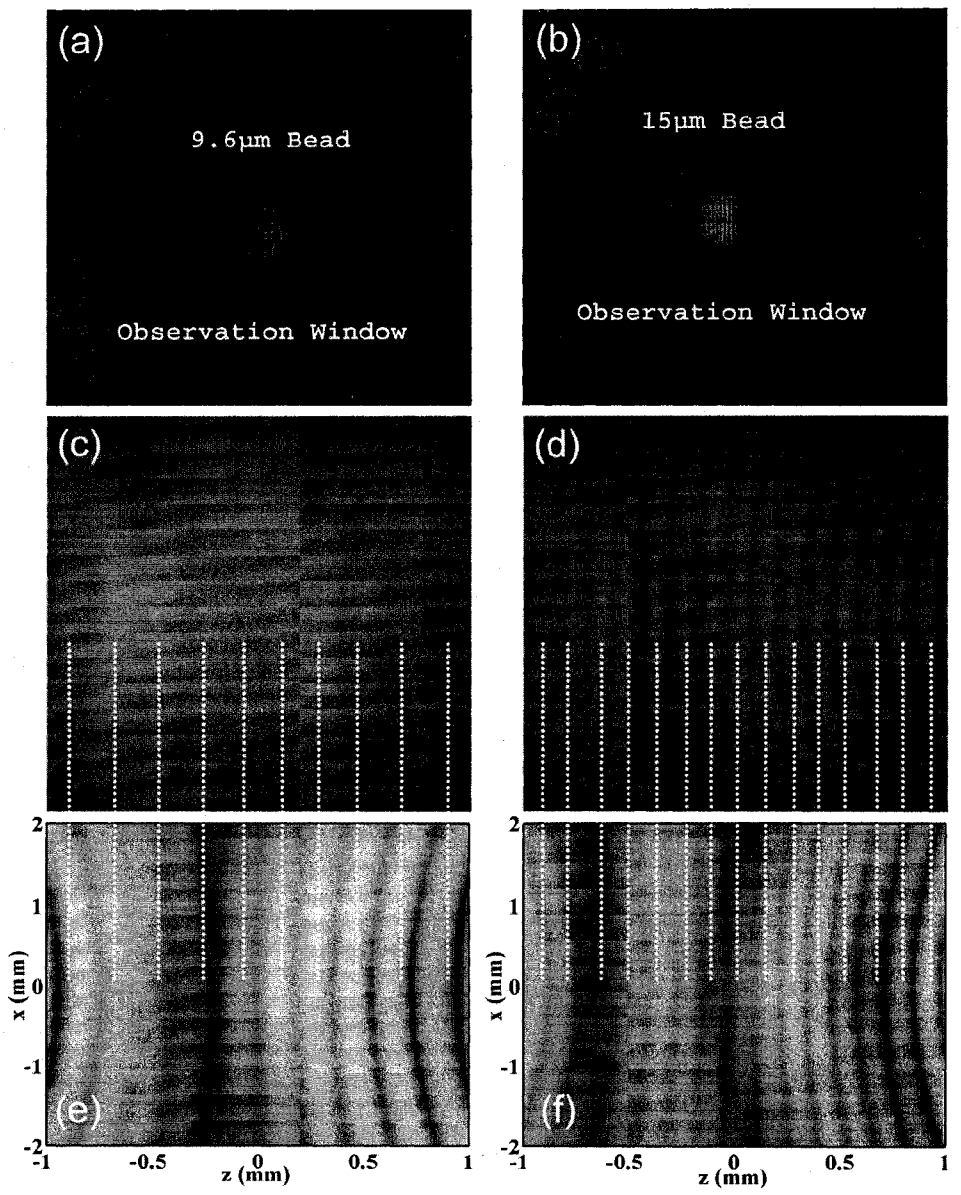

Figure 5.6 Comparisons between polystyrene beads experimental and FDTD simulation scatter patterns. (a) and (b) are the polystyrene beads defocused scatter images excited by a green laser in the micro-channel obtained by using a digital camera. (c) and (d) are the 2D scatter patterns from the 9.6 and 15μm polystyrene beads obtained by using a CCD array, respectively. (e) and (f) are the FDTD simulation results for the 9.6 and 15μm polystyrene bead scatter patterns in the waveguide cytometer, respectively. The white dotted lines between (c) and (e), (d) and (f) are drawn to show the corresponding fringe positions between experimental and FDTD simulation results.

As shown in Fig. 5.6, 10 bands are obtained for 9.6μm polystyrene bead, and 15 bands are obtained for 15μm polystyrene bead, for both experimental and FDTD simulation results. The band positions match between experimental and simulation scatter patterns for both the 9.6 and the 15μm polystyrene beads. Figure 5.7 shows a representative cross section comparison between the experimental and FDTD simulation results for 15μm bead as shown in Fig. 5.6(d) and (f).

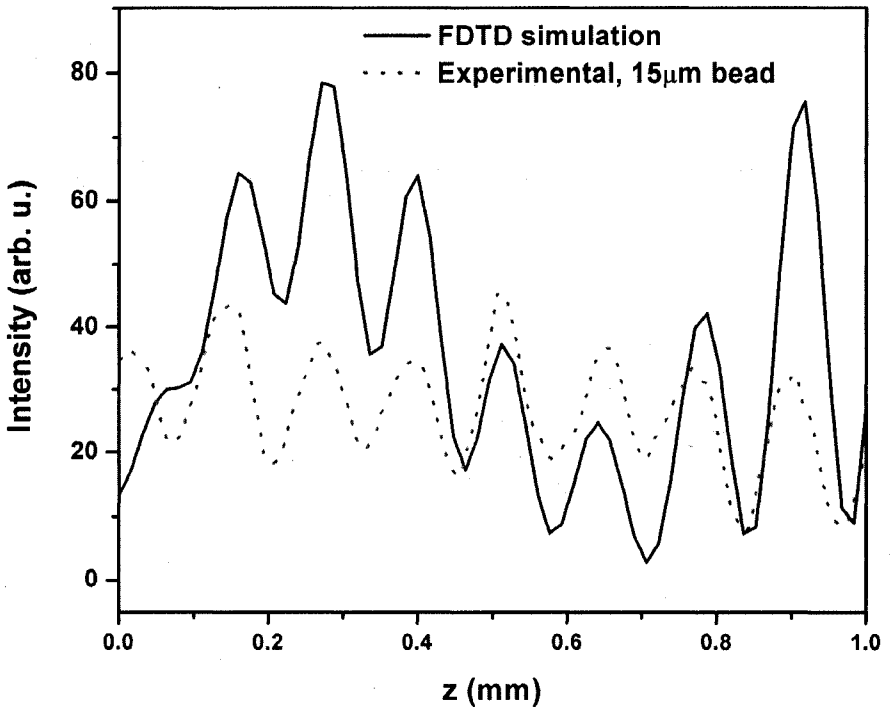

Figure 5.7 A cross section comparison between experimental and FDTD simulation results for 15μm bead. The cross sections shown here are along z axis at $x = 0$ mm as shown in Fig. 5.6.

5.4.3 FDTD simulation of biological cells within the integrated cytometer

The FDTD method can be used to predict light scattering in the integrated waveguide cytometer for cases where Mie theory is not applicable. An example is the following case where light scattering from a biological cell with randomly

distributed organelles. The models used here are white blood cells, which are spherical structures with complex inner organelle distributions. A FORTRAN program was written to generate randomly distributed organelles inside a spherical shell (or ellipsoidal structure). The program guarantees there is no overlap between the organelles inside the spherical shell. The organelles are assumed to be spherical and can be of different sizes.

Most white blood cells have a cell radius around 5μm, with a nucleus of approximately 3μm in radius. In the FDTD simulations to be described, the white blood cells are assumed to be located at the origin in the cytometer. The cell cytoplasm has a refractive index of 1.38, and the nucleus has a refractive index of 1.39 (located at the origin of the cytometer). Two different cell structures were studied, one for a white blood cell with 180 mitochondria (500nm in radius, with a refractive index of 1.42), and the other for a white blood cell without mitochondria. The illumination source is a 543nm green laser, and the surrounding medium has a refractive index of 1.334.

Figure 5.8 shows the representative FDTD light scattering intensity distributions along the z axis at symmetrical x positions about $x = 0$ mm for the cell models with and without mitochondria. The solid line in Fig. 5.8 shows the FDTD results for the cell model without mitochondria at $x = -1.33$ mm, while the triangle signs show the FDTD results for the same cell model at $x = 1.33$ mm. Similarly, the dotted line in Fig. 5.8 shows the FDTD results for the cell model with 180 mitochondria at $x = -1.33$ mm, while the circle signs show the FDTD results for the same cell model at $x = 1.33$ mm. From Fig. 5.8, we find that for the cell models without mitochondria, the light scattering intensity distributions overlap with each other at $x = -1.33$ mm and $x = 1.33$ mm. Thus the light scattering intensity distributions are approximately azimuthally symmetric about $x = 0$ mm for the cell models without mitochondria. However, for the cell models with mitochondria, this azimuthal symmetry is broken as shown in Fig. 5.8 due to the randomly distributed mitochondria. The light scattering intensity distributions

in Fig. 5.8 for the cell models with 180 mitochondria at symmetrical x positions not only have different intensity levels, but also have different intensity peak distributions. Figure 5.8 shows that the randomly distributed mitochondria in biological cells break the azimuthal symmetry (cell model without mitochondria) of the 2D light scattering patterns.

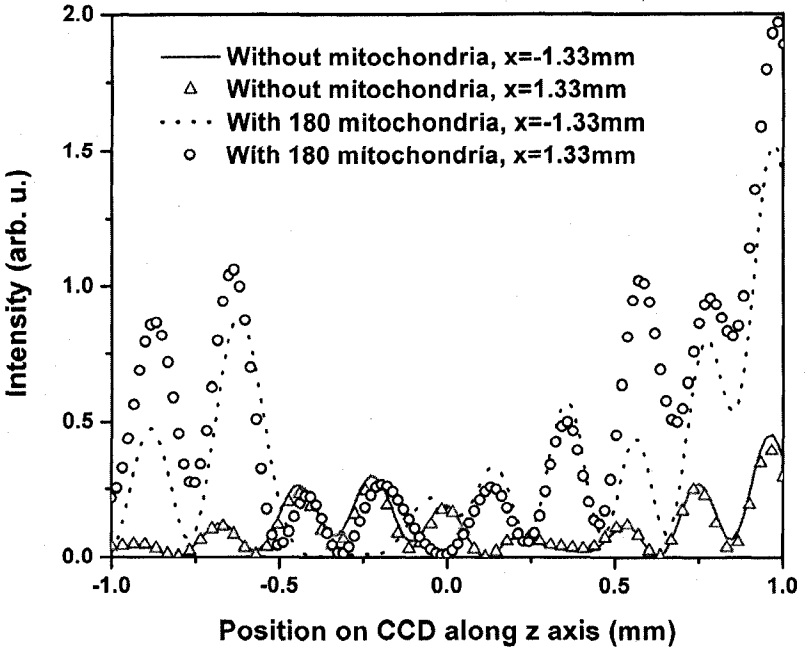

Figure 5.8 Mitochondria break the azimuthal symmetry of the 2D light scatter patterns. The results show the light scattering intensity distributions along z direction at different x positions. The light scattering intensity distributions from biological cell models with or without mitochondria are shown at symmetrical x positions.

5.5 Conclusions

The integrated microfluidic waveguide cytometer was further developed in order to examine the dependence of light scattering on polarization. The polarization dependence was studied for different size polystyrene beads. The experimental results show that the light scatter patterns depend on the incident laser polarization angles. The incident laser with a polarization angle of 0^0 gave clearer scatter patterns and sharper Fourier peaks. Thus for light scattering measurements

from biological cells, the incident wave polarization effects must also be considered.

In order to study the effects of complex incident wave properties and complex scatterer structures on the light scatter patterns, the FDTD method was applied in the integrated waveguide cytometer. The 2D FDTD simulations agreed with the experimental results from different size beads. FDTD studies of biological cells with complex inner structures showed that the randomly distributed mitochondria in biological cells break the azimuthal symmetry of the 2D light scattering patterns. This would be of interest in understanding of light scattering from biological cells with complex inner structures.

5.6 References

1. H. M. Shapiro, *Practical flow cytometry*, (John Wiley & Sons, Inc., Hoboken, 2003).

2. W. T. Grandy, *Scattering of Waves from Large Spheres*, (Cambridge University Press, Cambridge, 2000).

3. C. F. Bohren and D. R. Huffman, *Absorption and scattering of light by small particles*, (John Wiley & Sons, Inc., New York, 1983).

4. V. Sankaran, M. J. Everett, D. J. Maitland and J. T. Walsh, "Comparison of polarized-light propagation in biological tissue and phantoms," *Optics Letters* **24**, 1044-1046 (1999).

5. V. Backman, R. Gurjar, K. Badizadegan, L. Itzkan, R. R. Dasari, L. T. Perelman and M. S. Feld, "Polarized light scattering spectroscopy for quantitative measurement of epithelial cellular structures in situ," *IEEE Journal of Selected Topics in Quantum Electronics* **5**, 1019-1026 (1999).

6. X. T. Su, W. Rozmus, C. Capjack and C. Backhouse, "Side scatter light for micro-size differentiation and cellular analysis," *Proc. of SPIE* **6446**, 64460w (2007).

7. C. C. Yu, C. Lau, J. W. Tunnell, M. Hunter, M. Kalashnikov and C. Fang-Yen, "Assessing epithelial cell nuclear morphology by using azimuthal light scattering spectroscopy," *Optics Letters* **31**, 3119-3121 (2006).

8. X. T. Su, C. Capjack, C. Backhouse and W. Rozmus, "Mitochondria break the 2D light scattering azimuthal symmetry within an integrated cytometer," (in preparation).

9. E. Hecht, *Optics*, (Addison Wesley Longman, Inc., Reading, 2002).

10. C. G. Liu, C. Capjack and W. Rozmus, "3-D simulation of light scattering from biological cells and cell differentiation," *Journal of Biomedical Optics* **10**, 014007 (2005).

Chapter 6

Light scattering from biological cells in the integrated cytometer

6.1 Introduction

The integrated microfluidic waveguide cytometer described in the previous chapters is capable of obtaining 2D side-scatter patterns from single cells.[1, 2] The side scatter is rich in information about the mitochondria.[3-7] Furthermore, the capture of 2D light scattering patterns provides far more information about biological cells compared with 1D signals and may allow the characterization of cells independently of their orientation[8]. Although Mie theory[9, 10] is a useful starting point to predict light scatter by (typically) spherical structures, biological cells (with their organelles and non-spherical shapes) are far too complex to be modeled by Mie theory. Numerical simulations via Finite-Difference Time-Domain (FDTD) methods[5, 6, 11-13] have been applied to model scattering by such complex structures, allowing the study of biological cells with a spatial resolution of tens of nanometers, readily resolving the scattering effects by the various organelles (micron and sub-micron in scale) in a single cell. Although Lu *et. al.* have determined the FDTD 2D scatter patterns of a biconcave shaped human red blood cell,[12] the bulk of these FDTD simulations have focused on the characterizations of the 1D scatter spectra to extract cellular information. The application of the FDTD method in the integrated cytometer has been developed

and validated in Chapter 5. In this chapter, comparisons between the experimental 2D scatter patterns of biological cells with those obtained by 3D FDTD simulations are performed. We use these comparisons to determine the origin of the major features in the scatter patterns.

Our simulation results show that the cytoplasm and the nucleus of single cells produce fringes in the 2D scatter patterns, while the mitochondria within the cell create a pattern of localized regions of higher intensity in the scatter patterns. We refer to these localized regions as "small scale 2D structures" and we are not aware of any prior reports in the literature of such observations. As expected, the scatter patterns produced both by the FDTD simulations and from experiments involving yeast cells, show fringes. We demonstrate that the different orientations of a yeast cell in the microchannel will change the fringe patterns, but will not generate the small scale 2D structures. By contrast, FDTD simulations and experimental scatter patterns from human (Raji) cells show scatter patterns that are dominated by small scale 2D structures. We demonstrate here that the small scale 2D structures provide information about the mitochondrial distribution in a human cell. Given the important role of mitochondria in human diseases such as cancer,[14] aging,[15] Parkinson's and Alzheimer's,[16] a non-invasive method of characterizing mitochondria could be of great importance as a diagnostic tool.

The Fourier method developed in Chapter 4 is further applied to size yeast cells in this chapter.

This chapter is partly based on a recently published journal paper by X. T. Su, *et al.*[17]

6.2 Effects of mitochondria upon the scatter patterns

6.2.1 FDTD simulations of cell models in the waveguide cytometer

For the cell model in the liquid-core waveguide cytometer as shown in Fig. 6.1, the light scattering recorded by the CCD will be affected by the cell orientation and the organelle distribution. Programs were written to distribute organelles

randomly throughout the cytoplasm of the cell. The nucleus and the mitochondria were assumed to be spherical while the cell itself could be ellipsoidal. To study the cell orientation effects, the ellipsoidal cell model was used. The cell can be rotated through any polar angle θ about the x axis as shown in Fig. 6.1. The minimum distance between any two organelles is usually set to 10nm. The codes ensure that there is no overlap of organelles, and the organelles are all inside the cytoplasm of the cell. The outputs of these codes have information about the cell component size and refractive index, which can be used as the input data for the FDTD simulations. The output data of these codes are visualized by using the AVS software (Advanced Visual Systems Inc., USA). In the visualization, different colors are used to denote the refractive index for each kind of organelle. The axes in the artificial cell models show the cell orientations. Unless otherwise specified, the nucleus and the cell itself are centered at the origin. The visualization helps for better understanding of the FDTD scatter patterns related to the cellular structure and shape.

We have applied the FDTD code to the compact planar waveguide cytometer.[1] For a cell model in the liquid-core waveguide cytometer, the scattered light propagates from the liquid core through a substrate (1.2mm, refractive index 1.47), an air gap (0.35mm), a CCD cover glass (0.75mm, refractive index 1.5), and another air gap (1.25mm), until 2D light scattering patterns are obtained on the plane CCD screen. The FDTD simulations were performed on Silicon Graphics Inc. (SGI) parallel computers under WestGrid (a collaborative project that provides high performance computing and multimedia/visualization resources to researchers and educators across Western Canada). For the larger Raji cells, a large memory allocation of 120 Gigabyte (GB) is typically required to perform a simulation, and approximately 40 hours of running time is needed for a space step of 50nm. For a smaller yeast cell, a memory of 12GB is usually allocated and the simulation can be finished within 24 hours for a space step of 30nm. The number of processors required depends on the memory of each processor (typically

memory of 0.25GB, 0.5GB and 1.0GB). The inset in Fig. 6.1 provides additional information regarding the FDTD geometry.

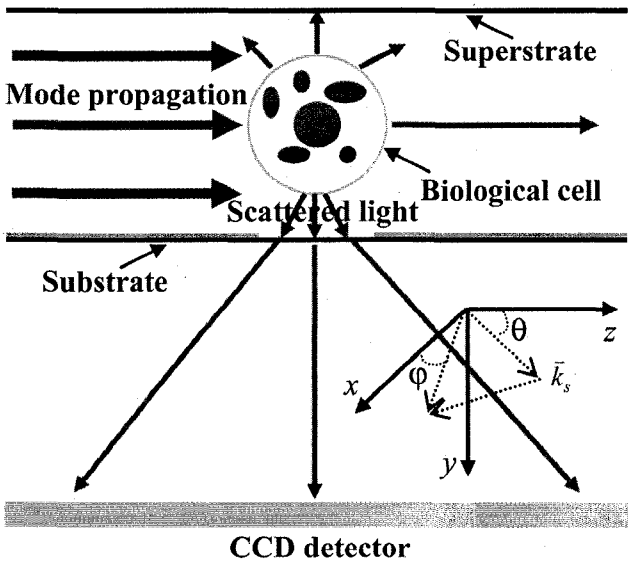

Figure 6.1 Illustration of a biological cell in the planar waveguide structure and its scattering geometry. The incident wave vector is along the z axis, while polarized along the x axis. The scattered wave vector has a polar angle θ, and an azimuth angle φ. For all the studies in this chapter, the cell is centered at the origin. The scattered light goes from the liquid core through a substrate (1.2mm, refractive index 1.47), an air gap (0.35mm), a CCD cover glass (0.75mm, refractive index 1.5), and another air gap (1.25mm) onto a CCD surface as shown in Fig. 4.6.

6.2.2 FDTD study of the mitochondria effects upon the 2D scatter patterns

For the purposes of studying light scattering, the biological cells are described in terms of size and refractive index variations. Unless otherwise specified, for the FDTD simulations in this chapter, the cytoplasm is taken to have a refractive index of 1.38,[18] the nucleus 1.39,[19] the mitochondria 1.42,[20] and the cell is immersed in phosphate buffered saline (PBS) of refractive index 1.334.[21] A program has been written to generate (3D) artificial biological cell models comprised of a membrane, a nucleus, cytoplasm and a random distribution of mitochondria throughout the cytoplasm. The visualizations of these 3D biological cells are shown in Fig. 6.2. The cell in Fig. 6.2 has a radius of 2μm, a nucleus

with a radius of 1μm, and contains 40 mitochondria, each with a radius of 250nm. In Fig. 6.2(a), the cell only has a nucleus and cytoplasm, while Fig. 6.2(b) shows a cell with only randomly distributed mitochondria (random seed I). In Fig. 6.2(c), the cell has randomly distributed mitochondria (random seed I), a nucleus, and cytoplasm. Figure 6.2(d) has randomly distributed mitochondria (random seed II), a nucleus, and cytoplasm. The FDTD method has been applied to simulate these models in an environment that includes the effects of the integrated microfluidic waveguide cytometer[1] (leading to a distortion of the scatter patterns). The FDTD geometry and the planar waveguide structure are illustrated in Fig. 6.1. The calculated 2D scatter patterns are in the zx plane, where z is the horizontal axis and x is the vertical axis. In this study, a 632.8nm HeNe laser is used to illuminate the single cells in the microchannel.

Representative 2D FDTD scatter patterns are shown in Figs. 6.2(a') to (d') for the cell models shown in Figs. 6.2(a) to (d), respectively. As is seen in Fig. 6.2(a'), when there is only the cytoplasm and a nucleus in the cell, the 2D scatter pattern has only fringes. Figure 6.2(b') corresponds to the case where only mitochondria are present and shows a 2D scatter pattern with a sparse distribution of localized regions of high intensity (i.e. "small scale 2D structures"). Figures 6.2(a') and (b') show that the microstructures in the cell, such as the nucleus and the cytoplasm, give continuous fringes in the 2D scatter patterns, while the sub-micron scale mitochondria give a distribution of small scale 2D structures. Figure 6.2(c'), corresponding to a cell model (Fig. 6.2(c)) containing cytoplasm, a nucleus, and mitochondria, shows scatter patterns containing both fringes and small scale 2D structures. Figure 6.2(d') also corresponds to a cell model (Fig. 6.2(d)) containing cytoplasm and a nucleus, but has a different distribution of mitochondria. Although Fig. 6.2(c') and (d') have the same number and position for the fringes, they have different distributions of the small scale 2D structures.

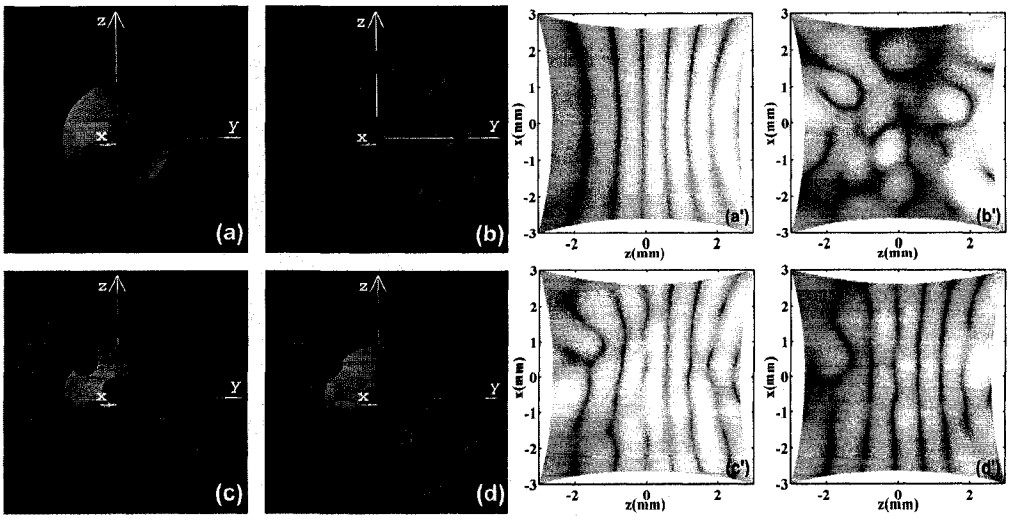

Figure 6.2 Various cell models and their corresponding 2D FDTD scatter patterns. (a), a cell with a nucleus (cyan) and the cytoplasm (magenta) only. (b), randomly distributed mitochondria (random seed I) only. (c), a cell with a nucleus, the cytoplasm, and the randomly distributed mitochondria (random seed I). (d), a cell with a nucleus, the cytoplasm, and the randomly distributed mitochondria (random seed II). (a'), (b'), (c') and (d') are the calculated 2D FDTD scatter patterns for the cell models (a), (b), (c) and (d) in the microfluidic waveguide cytometer, respectively.

The patterns shown in Figure 6.3 indicate that the position and size changes of the nucleus in a single cell do not generate small scale 2D structures. The cell models used for the simulations in Fig. 6.3 are with the same cell size as in Fig. 6.2(a), but with different nucleus size and positions in the cell cytoplasm. The AVS visualization of these cell models are not shown here. Compared with the FDTD 2D scatter patterns shown in Fig. 6.2(a'), we obtained different FDTD 2D scatter patterns for the cell models with nucleus size and position variations. Shown in Fig. 6.3 are the FDTD 2D scatter patterns obtained on the plane CCD. Figure (a) is the 2D FDTD scatter pattern for a cell with a nucleus of 1.2μm in diameter, and Fig. (b) is for the case of a nucleus with a diameter of 2.8μm. Figures (c) and (d) have the same size of nucleus as in Fig. 6.2 but at different positions. The nucleus for Fig. (c) is centered at (0, 0, 0.4)μm, and the nucleus for Fig. (d) is centered at (0, 0, -0.4)μm. Figure 6.3(e) shows the cross sections along z axis at $x = 0$ mm for (a), (b), (c), and (d).

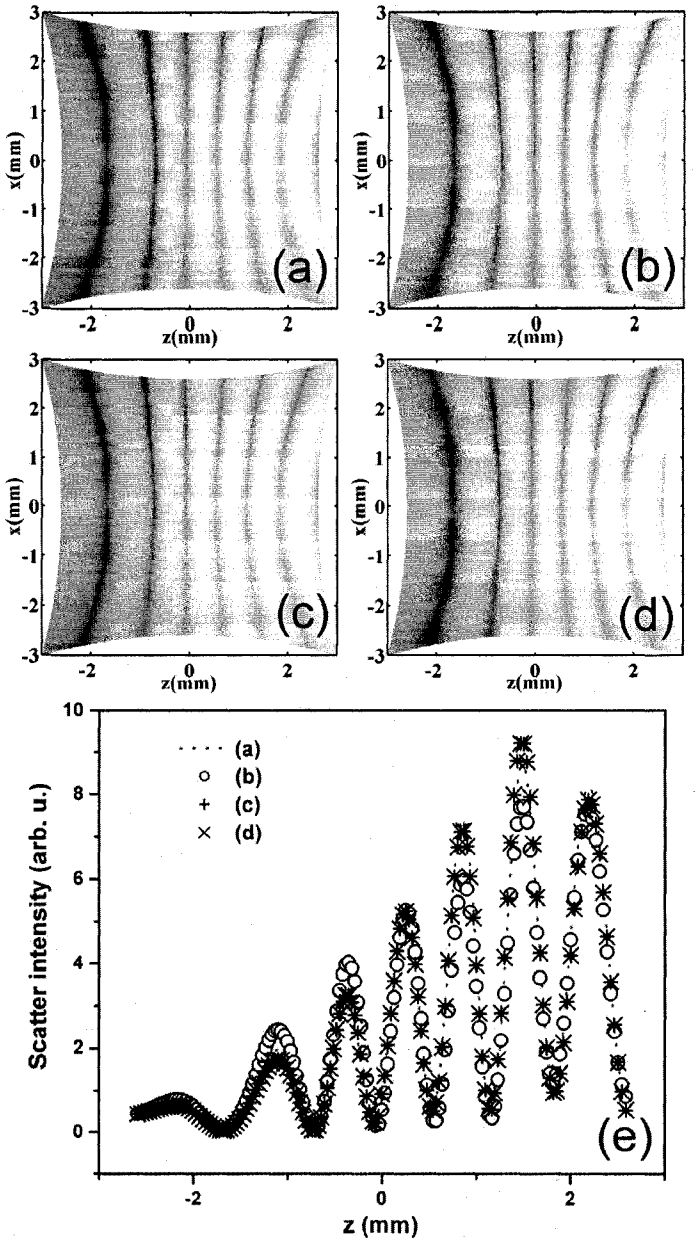

Figure 6.3 Representative figures showing nucleus size and position effects on the scatter patterns. Figure (a) has a nucleus of 1.2μm in diameter, and Fig. (b) has a nucleus of 2.8μm in diameter. Figures (c) and (d) have the same size of nucleus as in Fig. 6.2 but at different positions. The nucleus for Fig. (c) is centered at (0, 0, 0.4)μm, and the nucleus for Fig. (d) is centered at (0, 0, -0.4)μm. (e) shows the cross sections along z axis at $x = 0$ mm for (a), (b), (c), and (d). All the simulations are with the same incident intensity.

The results in Fig. 6.2 and Fig. 6.3 show that the spherical cell with a spherical nucleus generates the fringes, while the randomly distributed mitochondria generate the small scale 2D structures.

6.3Yeast cell 2D experimental scatter patterns

6.3.1 Measurements of yeast cells with the integrated cytomter

The illumination source used in the experiments was a 632.8nm HeNe laser (Melles Griot Laser Group). We performed the measurements using the integrated microfluidic 2D cytometry system described in Chapter 3.

After positioning a cell in the window we verify its identity (as a cell rather than a dust particle, bubble or other contaminant) by photographing it from above, and then acquiring its scatter pattern by integrating for 1/15 seconds. The scatter patterns shown here are reproducible, representative and typically give a signal of about 20 counts for a yeast cell, while the signal of the brighter mitochondrial small scale 2D structures are typically 30~50 counts out of a maximum CCD signal of 256 counts.

Saccharomyces cerevisiae yeast cells were prepared in our lab by resuspending the dried cells in filtered water (0.8μm filter, Millipore Corp., USA), diluting the resulting cells to a concentration of ~2000 cells/ml and sonicating for 2 minutes. The yeast cell sample was prepared and used the same day.

The *Saccharomyces cerevisiae* yeast cells used in this study are ellipsoidal structures, with a thick cell wall of about several hundred nanometers, a nucleus size of about 1μm in radius, and a few to tens of mitochondria, each with a radius of several hundred nanometers.[22, 23]

In Fig. 6.4, we show the 2D scatter pattern with fringes from a single yeast cell immobilized in the observation window area. Images of the same yeast cell taken with the Axiovert microscope show that it is an elliptical structure, with a semimajor axis of approximately 3μm, and a semiminor axis of approximately 2.5μm.

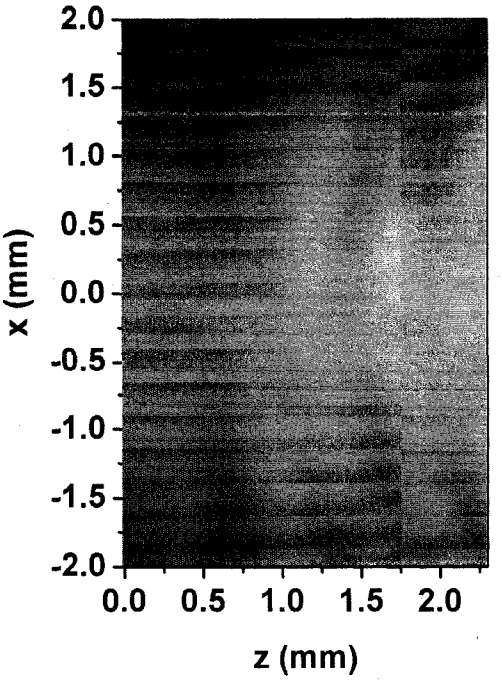

Figure 6.4 The 2D scatter pattern (showing several fringes) experimentally obtained from a yeast cell located within an integrated waveguide cytometer.

6.3.2 Yeast cell orientation effects

The orientation of a cell has a strong effect on its 1D elastic light scattering spectrum.[8] In order to show how strongly the orientation changes of a cell affect the 2D scatter patterns, FDTD simulations were performed on the ellipsoidal yeast cell models. Figures 6.5(a) and (b) show the AVS visualizations of the yeast cell models in the microchannel. The cell wall has a thickness of 200nm, the nucleus has a radius of 1.2μm, and the 40 randomly distributed mitochondria are assumed spherical with radii of 250nm. The refractive index for the cell wall is 1.45,[24] 1.42 for the mitochondria, 1.39 for the nucleus, and 1.38 for the cytoplasm. Each of the simulated yeast cells had the same number and distribution of mitochondria prior to rotation. Figures 6.5(c) and (d) show that distinctly different fringe patterns result from the different cell orientations in the microchannel. Comparing Figs. 6.5(c) and (d) with Fig. 6.4, we find similar fringe distributions from the experiment and the FDTD simulation - there are around 5 fringes in the same

CCD dimensions and neither Figure 6.5(c) nor (d) have obvious small scale 2D structures.

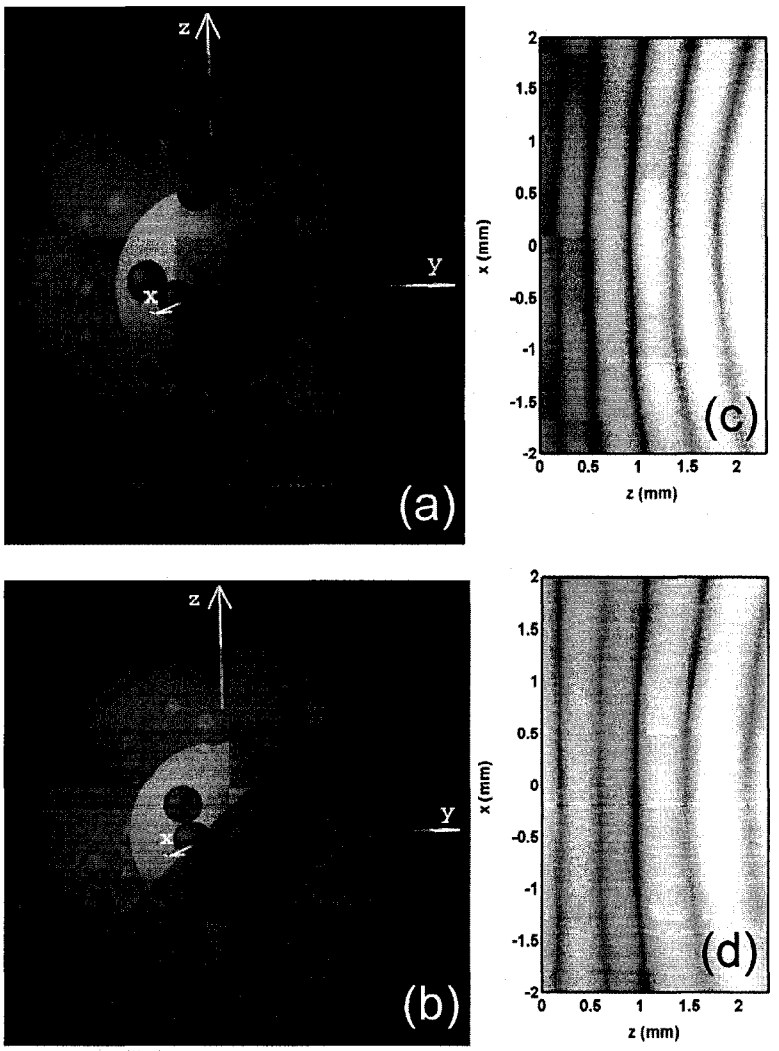

Figure 6.5 Yeast cell 2D FDTD scatter patterns with fringes. (a), a yeast cell model with its long axis along the *z* direction. (b), same yeast cell as in Fig. 6.5(a) rotated along x axis by 45^0. The yeast cell has a long axis of 2.9μm in radius, and both the two short axes have a radius of 2.4μm. The cyan sphere is the nucleus centered at the origin. The blue spheres are the random distributed mitochondria. The yeast cell wall and cytoplasm are shown in different colors of grey and magenta, respectively. (c) and (d) are the FDTD scatter patterns for the cell models (a) and (b), respectively.

Figure 6.6 shows yeast cell models and scatter patterns for cells with the same structures as those in Fig. 6.5 except that they do not have the mitochondria.

Comparing Fig. 6.6 with Fig. 6.5, we find that the mitochondria effects in the yeast cell models will not generate the small scale 2D structures. Figure 6.4, Fig. 6.5 and Fig. 6.6 show that the yeast cell scatter patterns are dominated by the fringes from the microstructural cytoplasm, nucleus and cell wall.

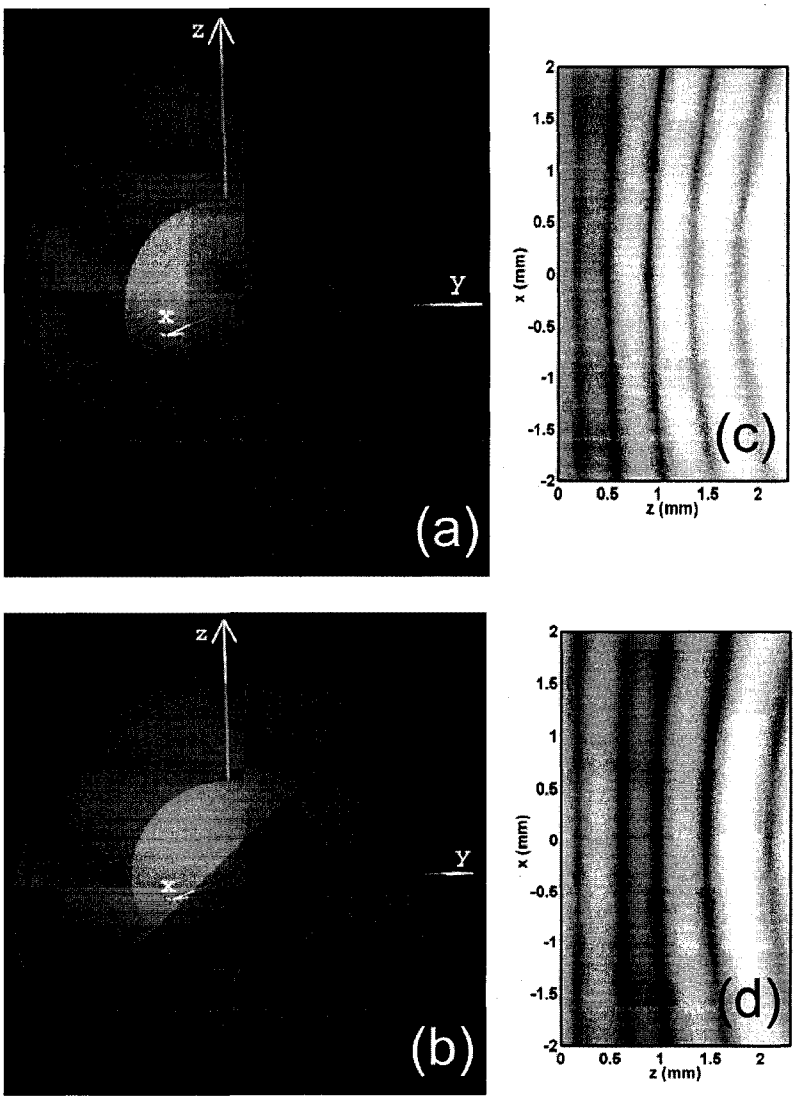

Figure 6.6 Representative figures showing that yeast cell orientation effects (cells without mitochondria) will not generate small scale 2D structures. Figures 6.6(a) and (b) are the same yeast cells as in Fig. 6.5, but without the mitochondria. Figure 6.6(a) is the yeast cell with the cell wall, the cell cytoplasm and the nucleus at an orientation of polar angle 0^0, while Fig. 6.6(b) at an orientation of polar angle 45^0. Figure 6.6 shows that the

orientation effect of the microstructures in a yeast cell will not generate the small scale 2D structures. The orientation effects change the fringe distributions.

In contrast to the simulations of Fig. 6.2, there are no obvious small scale 2D structures in the yeast cell 2D scatter patterns either experimentally as in Fig. 6.4, or in the simulations as in Fig. 6.5. This is despite having the same number and size of mitochondria in the simulations of Fig. 6.2 as in those of Fig. 6.5. We attribute this difference to the very strong role played by the yeast cell wall (not present in the simulation of Fig. 6.2). This wall is not only thick, but also occupies a substantially higher volume, with a higher refractive index, than the mitochondria. In the yeast cell models used here, the volume ratio for the mitochondria (refractive index 1.42) to the whole yeast cell is 3.74%, and the volume ratio for the cell wall (refractive index 1.45) to the whole yeast cell is 21.77%. As such it would appear that for yeast cells the microstructure (here the thick yeast cell wall) dominates the side-scatter patterns and no small scale 2D structures are generated.

6.4 Human cell 2D scatter patterns with "small scale 2D structures"

6.4.1 Measurements of Raji cells with the integrated cytometer

We have used Raji cells from a lymphoblast-like cell line created from a human Burkitt's lymphoma (ATCC (American Type Culture Collection), CCL-86). The Raji cells we used were grown in 90% RPMI-1640 (Roswell Park Memorial Institute) medium with 2mM L-Glutamine (Gibco, Invitrogen Corporation, Canada) supplemented with 10% Fetal Bovine Serum (Gibco, Invitrogen Corporation, Canada) plus 10μg/mL Gentamicin (Gibco, Invitrogen Corporation, Canada) and 10mM Hepes Buffer (Gibco, Invitrogen Corporation, Canada). Cells were cultured in a six-well multiwell plate (Becton Dickinson, USA) at 105/mL for 3-4 days before reaching confluency. They were incubated at 37^0C (Forma II, Thermo Electron Corp., USA) in 5% CO_2 (Praxair, Canada).

In order to more easily handle these biohazardous cells, they were fixed (i.e. killed) using a formaldehyde fixation method. They were centrifuged at 2000rpm for 5 minutes in a 15mL Falcon conical tube (Becton Dickinson, USA). The supernatant was then removed and cells were washed with 1x phosphate buffered saline solution (PBS). After removing the final supernatant, cells were re-suspended in a 2% formaldehyde solution (FA) (Fisher, Canada) at a concentration of 10M cells per 250μL FA, for 10 minutes at room temperature. The cells were again washed, centrifuged, and re-suspended in 1x PBS. The final cell concentration was transferred to a micro-centrifuge tube (Fisher Scientific, USA), stored on ice, and used the same day. In order to more easily use the Raji cells in a single-cell observation mode, the solution was diluted to a density of 2000 Raji cells per milliliter. This method ensured that the cytometer only used intact cells by imaging each cell prior to acquiring the scatter pattern.

As seen under the Axiovert microscope, the Raji cells are spherical with a radius of about 8μm and are almost transparent in the PBS solution. Figure 6.7 shows the scatter pattern obtained from a Raji cell, consisting of a sparse distribution of small scale 2D structures without any clear fringes.

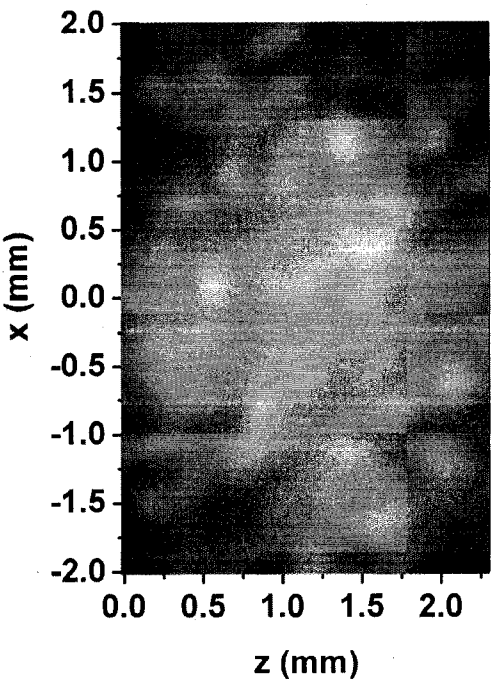

Figure 6.7 The 2D scatter pattern (showing a sparse distribution of small scale 2D structures) experimentally obtained from a human Raji cell within an integrated waveguide cytometer.

6.4.2 Mitochondria dominate the 2D Raji cell scatter patterns

In order to compare the experimental scatter pattern with FDTD simulations, we use the Raji cell models shown in Fig. 6.8. The Raji cell model has a radius of 8μm and a nucleus with a radius of 4μm. There are 300 randomly distributed mitochondria (an average number, as observed mitochondria numbers per cell varies in different cell types from 83~677)[25] with radii of 500nm (intermediate size within the observed range 0.25~1μm in radius)[26]. The cell cytoplasm has a refractive index 1.35[27] (almost transparent in the PBS buffer), the nucleus has a refractive index of 1.39, and the mitochondria have a refractive index of 1.42.

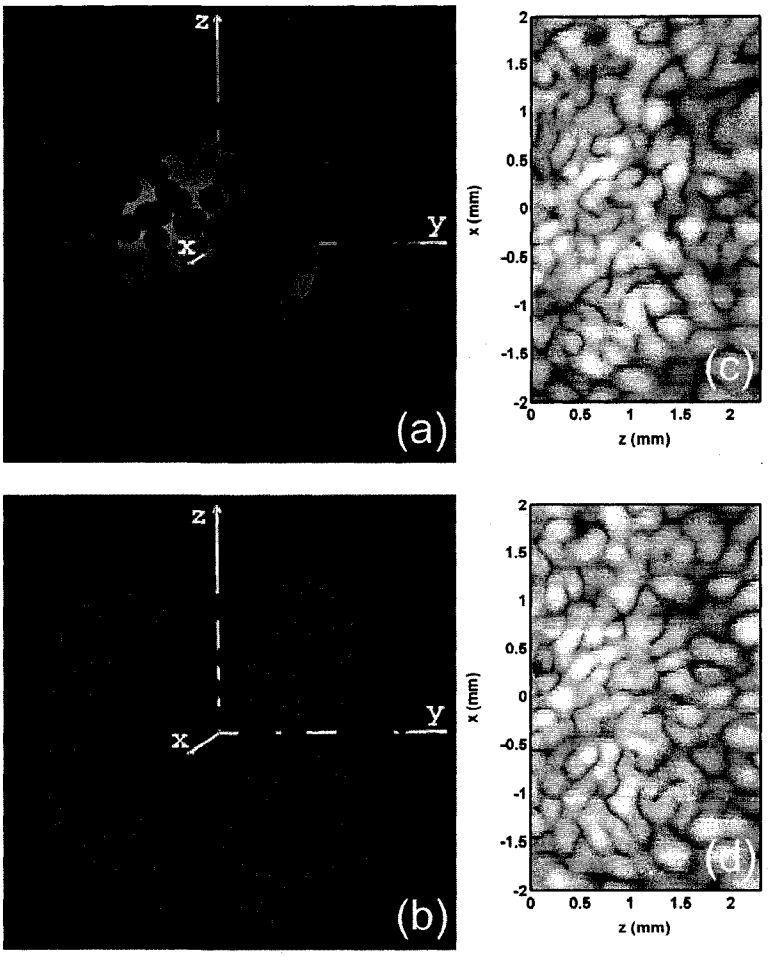

Figure 6.8 Raji cell models and their 2D FDTD scatter patterns. (a), a Raji cell with 300 randomly distributed mitochondria, a nucleus and cytoplasm. (b), a "cell" with only the 300 randomly distributed mitochondria. (a) and (b) have the same mitochondrial distribution. (c) and (d) are the 2D FDTD scatter patterns for (a) and (b), respectively.

Typical human cell membrane has a thickness about 10nm[18] with a refractive index 1.46.[28] FDTD simulations show that for a 1.5μm cell (in radius), the 10nm cell membrane (volume ratio of 1.99%) contributes significantly less than the 1.5μm cell cytoplasm. Figure 6.9(a) is the FDTD 2D scatter pattern obtained on the CCD screen for a spherical cell (1.49μm in radius) with a layer of cell membrane (10nm), and Fig. 6.9(b) is the FDTD 2D scatter pattern obtained on the CCD screen for a spherical cell (1.5μm in radius). As can be seen in Fig. 6.9, the cell membrane will not generate the small scale 2D structures.

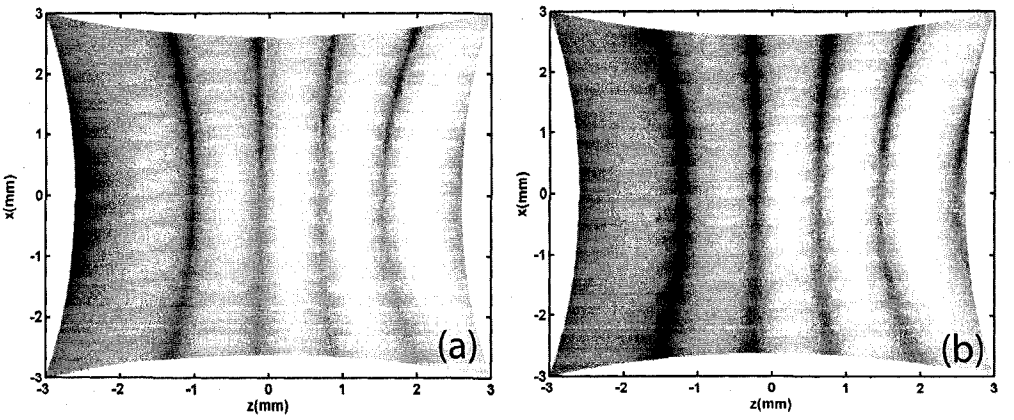

Figure 6.9 Cell membrane effects on the 2D FDTD scatter patterns. (a), FDTD scatter pattern for a spherical cell model (1.5μm in radius) with a layer of membrane (thickness 10nm). (b), FDTD scatter pattern for a spherical cell model (1.5μm in radius) without membrane.

To show the mitochondrial contribution to the 2D scatter patterns, various cell models are produced as shown in Figs. 6.8(a) and (b). Figure 6.8(b) has the same mitochondrial distribution as in Fig. 6.8(a) but without the microstructures (cell cytoplasm and cell nucleus) of the cell. The corresponding 2D FDTD scatter patterns, shown in Figs. 6.8(c) and (d) are dominated by small scale 2D structures.

The experimental (Fig. 6.7) and the simulation (Fig. 6.8) results for human cells show no obvious fringes but a significant distribution of small scale 2D structures. There are no clear fringes in Fig. 6.8(c), although the Raji cell model Fig. 6.8(a) has both the cytoplasm and the nucleus. Figure 6.8(d) has only the sparsely distributed small scale 2D structures, as the corresponding cell model in Fig. 6.8(b) has only the randomly distributed mitochondria. From Fig. 6.7, Fig. 6.8(c) and Fig. 6.8(d), we find that the small scale 2D structures dominate the Raji cell 2D scatter patterns. We attribute this to the large number of mitochondria, their large size (this leads to stronger side scatter), and the absence of a thick cell wall.

6.5 Different cellular component contributions in yeast and Raji cells

Our simulation results indicate (*e.g.* Fig. 6.2) that the microstructure generates fringes whereas the distributed mitochondria generate small scale 2D structures. On this basis, we initially expected to see similar behavior with yeast and human cells. Instead we encountered two extremes with the yeast cells producing no small scale 2D structures and human cells producing only small scale 2D structures.

In order to quantify the reason for the observed fringes with yeast cells and the observed small scale 2D structures with Raji cells, FDTD simulations are performed separately on various components of the yeast cell shown in Fig. 6.5(a). In the first case, only the 40 randomly distributed yeast mitochondria are considered without the presence of a nucleus, cytoplasm or the cell wall. In the second case, only the thick yeast cell wall is considered. The individual scatter pattern contributions from the 40 yeast mitochondria and the thick cell wall are shown in Figs. 6.10(a) and (b), respectively. From Fig. 6.10(a), the 40 yeast mitochondria give small scale 2D structures in the 2D scatter patterns, while the yeast cell wall gives the fringes in the 2D scatter patterns. The representative intensity levels for the scatter patterns from different cell component are shown in Fig. 6.11. As shown in Fig. 6.11, the solid line is the intensity level of the 40 yeast mitochondria with an intensity peak of approximately 0.5×10^{-9} (arbitrary units.). The line of dashed plus symbols is the scatter intensity level from the yeast cell wall with an intensity peak of approximately 1.0×10^{-8} units, and the dotted line is the intensity level for the 300 Raji mitochondria (cell model Fig. 6.8(b)) with an intensity peak of approximately 3.0×10^{-8} units. From the different intensity levels we notice that the contribution to the scattering from the yeast cell wall is approximately 20 times larger than that from the 40 yeast mitochondria, while the scattering from the 300 Raji mitochondria is approximately 60 times larger than

that from the 40 yeast mitochondria. The intensity level of the 300 Raji mitochondria is approximately 3 times larger than that of the yeast cell wall.

Experimentally, we obtain an intensity level of 20 counts for the yeast cell, and 30~50 counts for the Raji cell. Based on the experimental CCD counts, the yeast cell's mitochondrial scattering will contribute only one count to the CCD detector. Such a low intensity level is undetectable in the experimental background and only the effects of the cell wall will be detected.

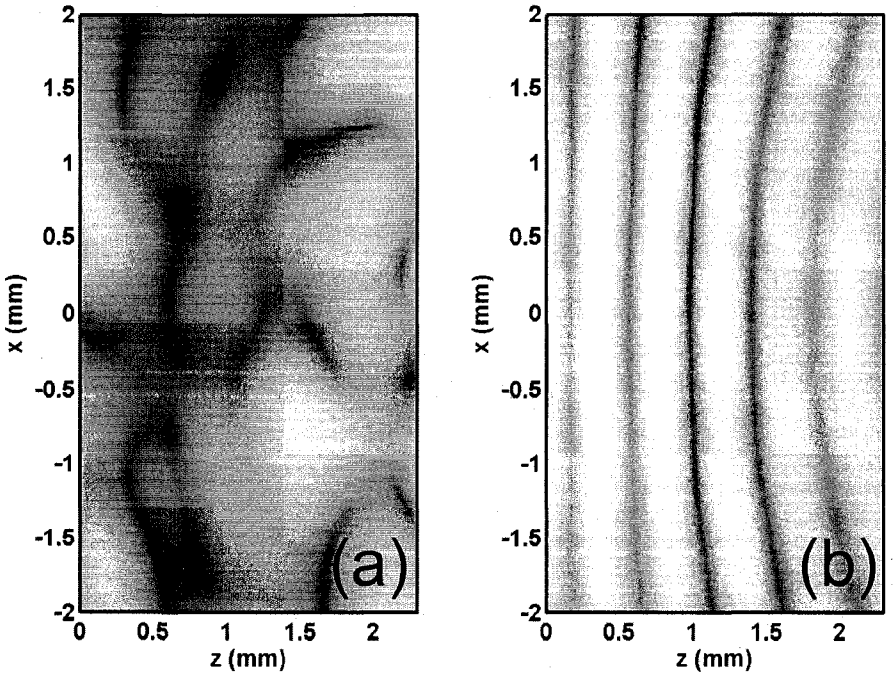

Figure 6.10 Scatter patterns from different cell components. (a) is a scatter pattern from only the 40 randomly distributed yeast cell mitochondria shown in Fig. 6.5(a). (b) is a scatter pattern from only the yeast cell wall shown in Fig. 6.5(a).

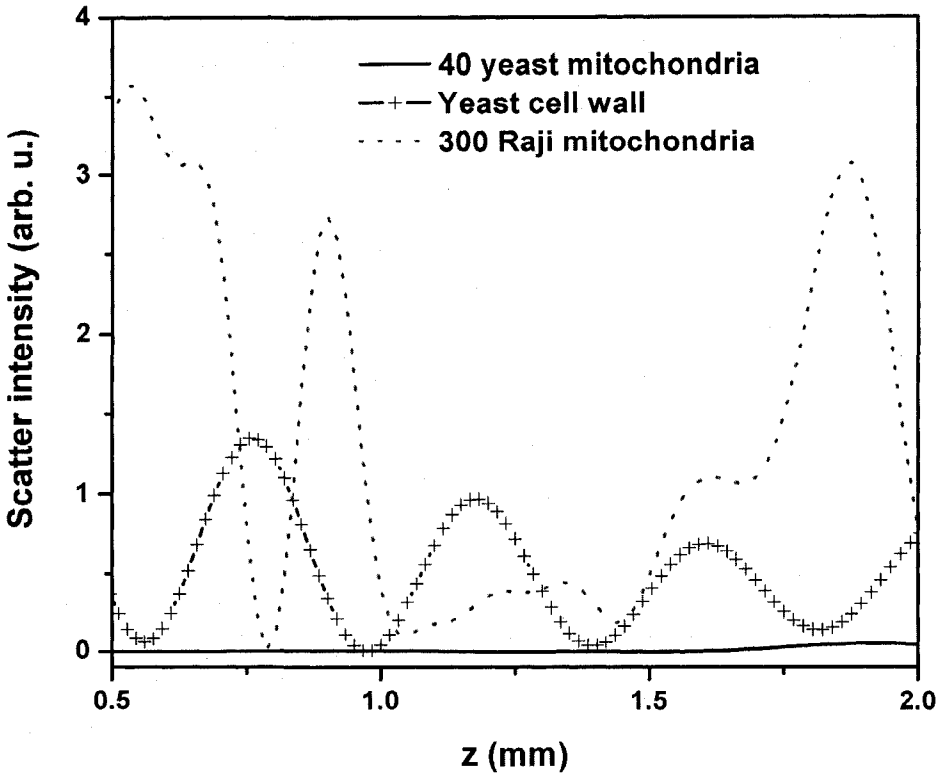

Figure 6.11 Scatter intensity level for different cell components. The scanning is performed for the same region in Fig. 6.10(a), Fig. 6.10(b) and Fig. 6.8(d), which are the scatter patterns for the 40 yeast mitochondria, the yeast cell wall and the 300 Raji mitochondria, respectively. All the simulations are with the same incident intensity.

In past work, our use of the new 2D cytometry method was intended to provide a more complete characterization of individual cells.[1] The present work demonstrates a novel method that provides information not only on the microstructure within the cell, but also on the distribution of mitochondria within the cell. Although imaging methods exist to detect mitochondria (*e.g.* with mitochondrially selective fluorescent dyes), these often perturb the function of the cell and are complicated by the size of the mitochondria being near or below the resolution limitation of the microscopes used. The present method, is based on scattering principles, and will be relatively unaffected by such effects. It is apparent then that the scatter patterns from experiment and simulation are

consistent in terms of overall behavior (i.e. fringes versus small scale 2D structures) and in terms of the relative magnitudes of the scatter intensities.

Clearly there is much to do in terms of extracting information from the scatter patterns. An example is the challenge of solving an inverse problem – we can simulate the scatter pattern of a parameterized cell, but given the scatter pattern of a cell it is far from straightforward to obtain estimates of the optimal set of parameters to describe that cell. This is a problem often encountered in imaging applications and is an active area of research. We are investigating several approaches (with an emphasis upon less computationally challenging ones) to better analyze the 2D scatter patterns. With such techniques, a brief (< 1 second) capture of the scatter pattern could provide information on the mitochondria of a living (and unperturbed) cell. Such information on the mitochondria within a cell could be extremely important in the detection and monitoring of disease conditions such as cancer, where normal and cancerous cells are reported to have different mitochondrial distributions.[29, 30]

6.6 Determination of yeast cell sizes by using the Fourier method

The above study has shown that yeast cell scatter patterns are characterized by fringes, while Raji cell scatter patterns are dominated by small scale 2D structures. The similarity between yeast cell scatter patterns and polystyrene bead scatter patterns allows us to adopt the Fourier method developed in Chapter 4 to size yeast cells.

Representative 2D light scattering patterns from different yeast cells are shown in Fig. 6.12 (a) and (b). They are in the same angular ranges as the polystyrene bead light scattering patterns studied in Chapter 4. Cross section scans of the 2D yeast cell scatter patterns are performed horizontally, and are integrated over 3 pixels around $x = 0$ mm vertically. Fourier transforms are then

performed on these scanned light scattering spectra. Figure 6.12 (c) and (d) show the Fourier spectra for yeast cell scatter patterns (a) and (b), respectively.

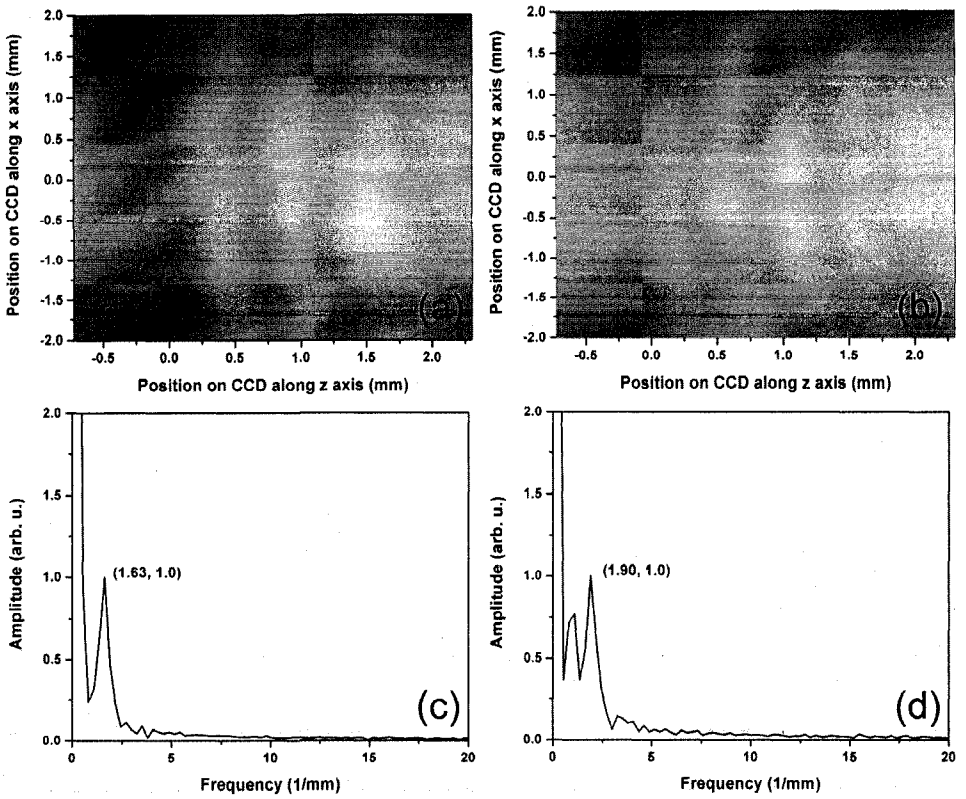

Figure 6.12 Yeast cell scatter patterns and their Fourier spectra. (a) and (b) are scatter patterns for different yeast cells. (c) and (d) are the Fourier transforms of the cross section scan of the light scattering patterns (a) and (b), respectively.

Calibration of our 2D cytometric technique for particle sizing has been performed in Chapter 4 by using different size polystyrene beads. The dotted line in Fig. 6.13 shows the linear fit of the experimental bead results with a refractive index 1.591. This linear fit can be used to determine the particle sizes with a constant refractive index. To size yeast cells, Mie theory simulations of different size spherical cells (with a refractive index of 1.42) in the waveguide cytometer are performed. Fourier transforms of the obtained Mie theory spectra give peak frequencies (1/mm) at 1.39, 3.60, 5.82 and 7.76 for cells with diameters 4μm, 9.6μm, 15μm and 20μm, respectively. These are plotted as peak frequency versus

different scatterer size in Fig. 6.13 (black dots). The solid line in Fig. 6.13 shows the linear fit of these Mie theory results.

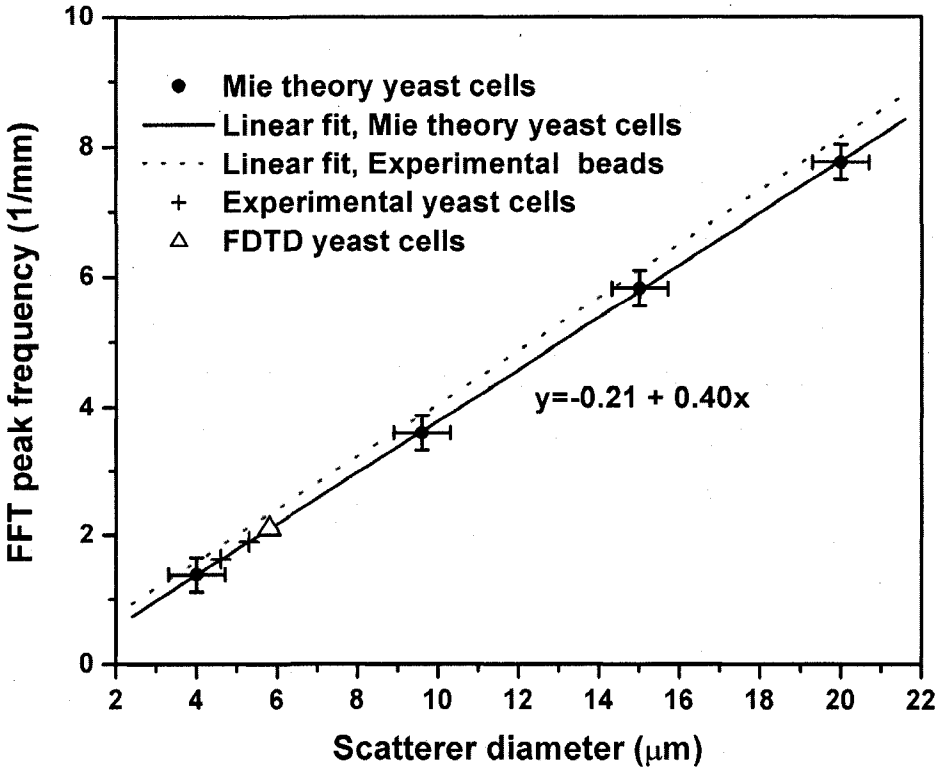

Figure 6.13 Sizing yeast cells by using the Fourier method. The yeast cell sizes can be determined by using the linear fit equation. The Fourier method has a resolution of 0.27 (1/mm), which gives a resolution of 0.7μm to estimate the scatterer diameter as in Chapter 4, shown as the error bars.

The solid line in Fig. 6.13 has a linear equation,

$$y=-0.21+0.40x \tag{6.1}$$

where y is the Fourier peak frequency (1/mm), and x is the scatterer size to be determined. The yeast cells in Fig. 6.12 have Fourier frequency peaks at 1.63 and 1.90 (1/mm). Substituting these Fourier frequency peaks into Equation 6.1, we obtain the yeast cells with sizes 4.6μm and 5.3μm for the yeast cell scatter patterns Figs. 6.12 (a) and (b), respectively. Fourier transforms on another four

yeast cell experimental results all give a peak frequency at 1.90 (1/mm). The yeast cell experimental results are plotted in Fig. 6.13 as plus signs.

Figure 6.14 (a) shows a yeast cell image. The yeast cell is approximately 5 to 6μm in diameter. The size estimation of yeast cells (here 4.6μm and 5.3μm in diameters) by using the Fourier method agrees with the measurements of yeast cells under a Zeiss Axiovert microscope, within error of 0.7μm. Figure 6.14 (b) shows a Raji cell image with rich inner structures, which generate small scale 2D structures in the scatter patterns. This limits the application of the Fourier method to size Raji cells. The yeast cell has a thick cell wall, which generates the fringes in the yeast cell 2D scatter patterns. This enables the adoption of the Fourier method to size yeast cells.

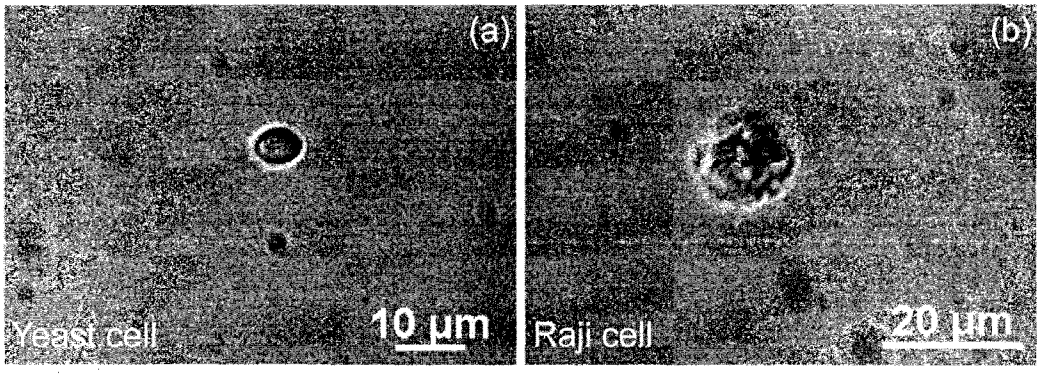

Figure 6.14 Yeast cell and Raji cell images under an Axiovert microscope.

FDTD simulations on more realistic yeast cell models with different orientations were presented in Fig. 6.5. Fourier transforms of the scanned light scattering spectra (along $x = 0$ mm) from these simulations are shown in Fig. 6.15 as a solid line and a dotted line at rotation angles of 0 degree and 45 degree, respectively. It is approximate from Fig. 6.15 that the cell models with different orientations give the same Fourier frequency peak at 2.10 (1/mm). Substituting this into Equation 6.1 gives the yeast cell sizes of 5.8 ± 0.7 μm in diameter. This agrees with the yeast cell size constants that are used in Fig. 6.5, with a long axis of 5.8μm.

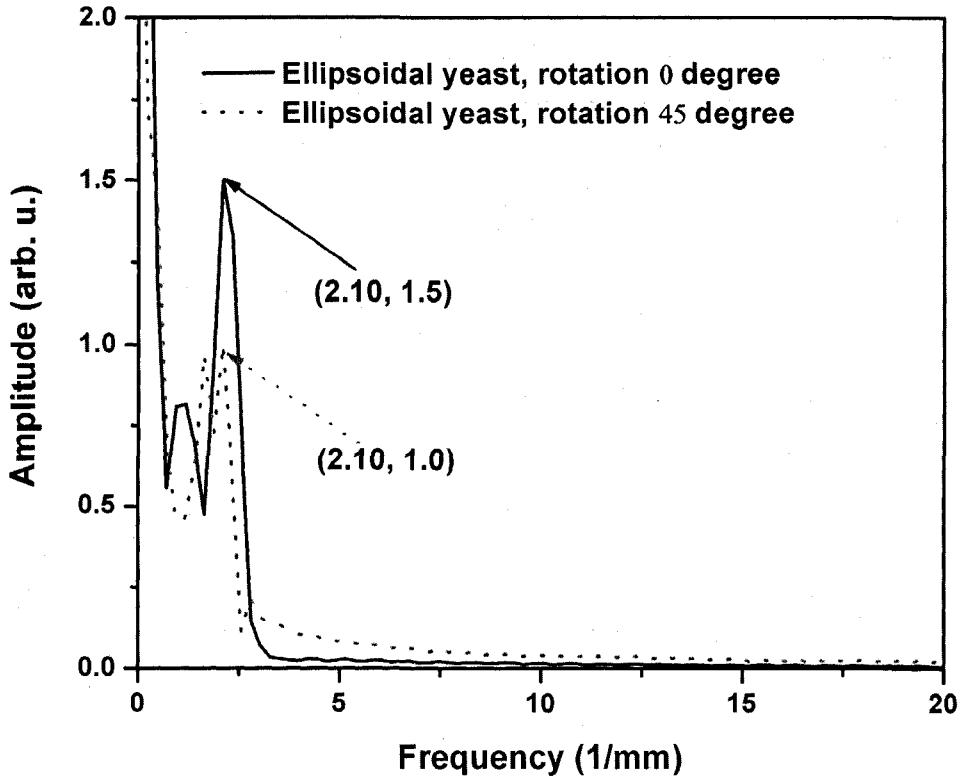

Figure 6.15 Fourier spectra of the FDTD simulation results of the cell models shown in Fig. 6.5. They have the same Fourier peak frequencies at 2.10 (1/mm).

6.7 Conclusions

The ability to characterize the mitochondria in single living cells may provide a powerful tool in clinical applications. Here we have applied a 2D (both polar angle and azimuth angle dependences) light scattering cytometric technique to assess experimental 2D light scattering patterns from single biological cells (yeast and human). We compare these patterns to those obtained from simulations using a 3D FDTD method and demonstrate that the microstructure (*e.g.* the cytoplasm and/or nucleus) of cells generates fringes of scattered light, while in the larger human cells the light scattered by the mitochondria dominates the scatter pattern, forming compact regions of high intensity that we term as "small scale 2D structures". These small scale 2D structures provide information on the

mitochondria within the cell and their analysis may ultimately be useful as a diagnostic technique.

The yeast cell scatter patterns with clear fringes allow the use of the Fourier method to size yeast cells. The size estimation of yeast cells by using the Fourier method agrees with the Axiovert microscope measurements.

6.8 References

1. X. T. Su, W. Rozmus, C. Capjack and C. Backhouse, "Side scatter light for micro-size differentiation and cellular analysis," *Proc. of SPIE* **6446**, 64460w (2007).

2. X. T. Su, K. Singh, C. Capjack, J. Petracek, C. Backhouse and W. Rozmus, "Measurements of light scattering in an integrated microfluidic waveguide cytometer," *Journal of Biomedical Optics* (accepted).

3. J. R. Mourant, J. P. Freyer, A. H. Hielscher, A. A. Eick, D. Shen and T. M. Johnson, "Mechanisms of light scattering from biological cells relevant to noninvasive optical-tissue diagnostics," *Applied Optics* **37**, 3586-3593 (1998).

4. H. B. Steen and T. Lindmo, "Differential of Light-Scattering Detection in an Arc-Lamp-Based Epi-Illumination Flow Cytometer," *Cytometry* **6**, 281-285 (1985).

5. C. G. Liu, C. Capjack and W. Rozmus, "3-D simulation of light scattering from biological cells and cell differentiation," *Journal of Biomedical Optics* **10**, 014007 (2005).

6. A. Dunn and R. RichardsKortum, "Three-dimensional computation of light scattering from cells," *IEEE Journal of Selected Topics in Quantum Electronics* **2**, 898-905 (1996).

7. J. D. Wilson, C. E. Bigelow, D. J. Calkins and T. H. Foster, "Light scattering from intact cells reports oxidative-stress-induced mitochondrial swelling," *Biophysical Journal* **88**, 2929-2938 (2005).

8. D. Watson, N. Hagen, J. Diver, P. Marchand and M. Chachisvilis, "Elastic light scattering from single cells: Orientational dynamics in optical trap," *Biophysical Journal* **87**, 1298-1306 (2004).

9. G. Mie, "Articles on the optical characteristics of turbid tubes, especially colloidal metal solutions," *Annalen Der Physik* **25**, 377-445 (1908).

10. W. T. Grandy, *Scattering of Waves from Large Spheres*, (Cambridge University Press, Cambridge, 2000).

11. R. Drezek, A. Dunn and R. Richards-Kortum, "A pulsed finite-difference time-domain (FDTD) method for calculating light scattering from biological cells over broad wavelength ranges," *Optics Express* **6**, 147-157 (2000).

12. J. Q. Lu, P. Yang and X. H. Hu, "Simulations of light scattering from a biconcave red blood cell using the finite-difference time-domain method," *Journal of Biomedical Optics* **10**, 024022 (2005).

13. A. Karlsson, J. P. He, J. Swartling and S. Andersson-Engels, "Numerical simulations of light scattering by red blood cells," *IEEE Transactions on Biomedical Engineering* **52**, 13-18 (2005).

14. P. Huang, L. Feng, E. A. Oldham, M. J. Keating and W. Plunkett, "Superoxide dismutase as a target for the selective killing of cancer cells," *Nature* **407**, 390-395 (2000).

15. Y. Michikawa, F. Mazzucchelli, N. Bresolin, G. Scarlato and G. Attardi, "Aging-dependent large accumulation of point mutations in the human mtDNA control region for replication," *Science* **286**, 774-779 (1999).

16. P. A. Trimmer, R. H. Swerdlow, J. K. Parks, P. Keeney, J. P. Bennett, S. W. Miller, R. E. Davis and W. D. Parker, "Abnormal mitochondrial morphology in sporadic Parkinson's and Alzheimer's disease cybrid cell lines," *Experimental Neurology* **162**, 37-50 (2000).

17. X. T. Su, C. Capjack, W. Rozmus and C. Backhouse, "2D light scattering patterns of mitochondria in single cells," *Optics Express* **15**, 10562-10575 (2007).

18. J. Beuthan, O. Minet, J. Helfmann, M. Herrig and G. Muller, "The spatial variation of the refractive index in biological cells," *Physics in Medicine and Biology* **41**, 369-382 (1996).

19. A. Brunstin and P. F. Mullaney, "Differential Light-Scattering from Spherical Mammalian-Cells," *Biophysical Journal* **14**, 439-453 (1974).

20. H. L. Liu, B. Beauvoit, M. Kimura and B. Chance, "Dependence of tissue optical properties on solute-induced changes in refractive index and osmolarity," *Journal of Biomedical Optics* **1**, 200-211 (1996).

21. F. Giess, M. G. Friedrich, J. Heberle, R. L. Naumann and W. Knoll, "The protein-tethered lipid bilayer: A novel mimic of the biological membrane," *Biophysical Journal* **87**, 3213-3220 (2004).

22. C. Charpentier, T. N. Vanlong, R. Bonaly and M. Feuillat, "Alteration of Cell-Wall Structure in Saccharomyces-Cerevisiae and Saccharomyces-Bayanus During Autolysis," *Applied Microbiology and Biotechnology* **24**, 405-413 (1986).

23. C. Bauer, V. Herzog and M. F. Bauer, "Improved technique for electron microscope visualization of yeast membrane structure," *Microscopy and Microanalysis* **7**, 530-534 (2001).

24. R. E. Marquis, "Immersion Refractometry of Isolated Bacterial Cell-Walls," *Journal of Bacteriology* **116**, 1273-1279 (1973).

25. E. D. Robin and R. Wong, "Mitochondrial-DNA Molecules and Virtual Number of Mitochondria Per Cell in Mammalian-Cells," *Journal of Cellular Physiology* **136**, 507-513 (1988).

26. T. G. Frey and C. A. Mannella, "The internal structure of mitochondria," *Trends in Biochemical Sciences* **25**, 319-324 (2000).

27. M. Kohl, M. Cope, M. Essenpreis and D. Bocker, "Influence of Glucose-Concentration on Light-Scattering in Tissue-Simulating Phantoms," *Optics Letters* **19**, 2170-2172 (1994).

28. J. S. Maier, S. A. Walker, S. Fantini, M. A. Franceschini and E. Gratton, "Possible Correlation between Blood-Glucose Concentration and the Reduced

Scattering Coefficient of Tissues in the near-Infrared," *Optics Letters* **19**, 2062-2064 (1994).

29. P. L. Gourley, J. K. Hendricks, A. E. McDonald, R. G. Copeland, K. E. Barrett, C. R. Gourley and R. K. Naviaux, "Ultrafast nanolaser flow device for detecting cancer in single cells," *Biomedical Microdevices* **7**, 331-339 (2005).

30. N. Haga, N. Fujita and T. Tsuruo, "Mitochondrial aggregation precedes cytochrome c release from mitochondria during apoptosis," *Oncogene* **22**, 5579-5585 (2003).

Chapter 7

Light scattering analysis of mitochondrial aggregation in single cells

7.1 Introduction

A better understanding of apoptosis, or programmed cell death, is important in determining the evolution of cancer. Cancerous cells fail to undergo apoptosis, and therefore exhibit expanded life spans compared to the normal cells.[1-3] A possible reason for this failure is that environmental pressures force cancerous cells to acquire resistance to apoptosis.[4] Mitochondria, the nanostructures in a single cell, serve as the central control point of apoptosis by releasing cytochrome *c*.[5] Although many other proteins are released during apoptosis, only cytochrome *c* appears to be essential for apoptosis.[6] Recent studies have shown that the release of cytochrome *c* is an early event in apoptosis,[7, 8] and substantial evidence indicates that peri-nuclear mitochondrial aggregation (most mitochondria in a biological cell cluster to the nucleus periphery) is an event that is upstream of cytochrome *c* release.[9]

Compounds which can induce apoptosis in tumor cells can be novel anti-tumor drugs. Mitochondria have been shown to serve as cancer drug targets.[10] It has been reported that arsenic trioxide (As_2O_3) can induce apoptosis in tumor cells by affecting the mitochondria. In untreated cancerous cells, mitochondria are

broadly distributed in the cytoplasm, while mitochondrial aggregation to the nucleus periphery is observed in As_2O_3 treated cell lines.[11] Peri-nuclear clustering of mitochondria has also been observed in other anti-cancer agent treated malignant cells by different research groups, while mitochondria are widely distributed in the untreated malignant cells.[12-16] Interestingly, recent research has reported that mitochondrial aggregation to the nuclear periphery has been observed in normal cells (no anti-cancer agent treatment), forming mitochondrial network, while mitochondria are randomly distributed in cancerous cells.[17]

The above research shows that in cancerous cells, the mitochondria are randomly (widely) distributed in the cell cytoplasm, while the mitochondria are aggregated to the nucleus periphery in both normal cells and anti-cancer drug treated malignant cells. Based on this observation, different cell models can be generated to simulate cancerous cells or normal cells with different mitochondrial distributions. A detection method that can distinguish these different models may ultimately be used as a new technique for cancerous cell detections.

Fluorophore-labeling techniques have been used to observe mitochondrial distributions in cells.[9, 11-17] These are invasive techniques to the biological cells. A label free, non-invasive method that could detect mitochondrial aggregation in single cells would be extremely useful in clinical cancerous cell detection. Light scattering techniques have been reported to provide a non-invasive study of biological cells.[18-24]

In this chapter, a light scattering approach is presented for cancerous cell detection. The small angle forward scattering is used to differentiate normal cell models from cancerous cell models. A method based on Fourier transform of wide angle side scattered light is introduced for better determination of biological cell sizes.

This chapter is based on a journal paper that is in preparation by X. T. Su, *et al.*[25]

7.2 3D biological cell model for the study of mitochondrial distribution in single cells

A computer code was written to generate different mitochondrial distributions in single cells in order to simulate both normal and cancerous cells. The probability of finding a mitochondrion at a distance R_d (center of a mitochondrion to the center of the nucleus) in a cell is given as (all sizes in μm):

$$\rho = \rho_0 \exp(-(R_d - r_n - r_m - \delta m)/(\alpha \times 10^{-6})) \tag{7.1}$$

$$\rho = 0.5 \tag{7.2}$$

$$\rho = \rho_0 \exp(-(r_c - R_d - r_m - \delta m)/(\alpha \times 10^{-6})). \tag{7.3}$$

Here r_n is the radius of the nucleus, r_m is the radius of the mitochondrion, r_c is the radius of the cell, and δm is the smallest distance between any two organelles. ρ_0 and α are constants for the probability distribution. Equation (7.1) describes mitochondrial aggregation to the nuclear periphery (normal cell), Equation (7.2) is for the randomly distributed mitochondria (cancer cell), and Equation (7.3) is for mitochondrial aggregation to the cell membrane (this is an extreme status of cancer cell for the completeness of our cell models, and there are few mitochondria at the nuclear periphery in this case.). The geometry for these models is shown in Fig. 7.1. The inner circle (r_n) shows the location of the nucleus, and the outer circle (r_c) shows the cell membrane. Zones I, II and III are used to show how many mitochondria are centered in each of these zones, and will be used to determine whether the mitochondria are aggregated to the nuclear periphery, have a random distribution, or are aggregated to the cell membrane. The thickness of zone I and zone III is defined as $r_m + \delta d$. In this study, we use $\rho_0 = 0.6$, $\alpha = 0.1$, $\delta d = 0.3\mu m$, and $\delta m = 0.01\mu m$. We assign different random seeds to generate different cell models. For each random seed, the mitochondria have three different distributions as determined by Equations (7.1) to (7.3).

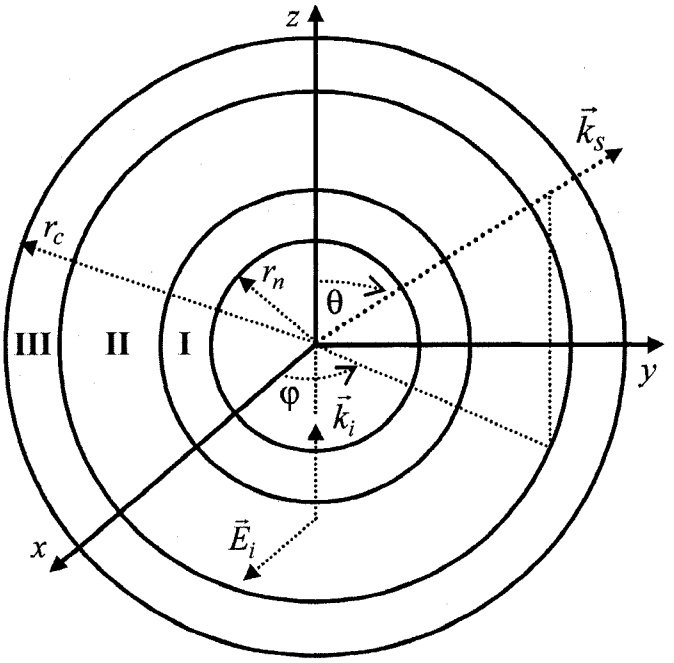

Figure 7.1 Geometry for the study of mitochondrial distributions in single cells. The scattered light $\hat{k}_s$ has an azimuth angle φ, and a polar angle θ. Zone I, zone II and zone III are used to show the different mitochondrial distributions in single cells.

We consider models for white blood cells (leukocytes). The typical radius of a white blood cell is about 5μm, with a nucleus that is about 3μm in radius.[26] Unless otherwise specified, these are the cell size and nucleus size that will be used in Chapter 7, each centered at the origin as in Fig. 7.1. A total of 180 spherical mitochondria with radii of 400nm are contained in each of the cell models. The refractive index for the cell cytoplasm is 1.38, 1.39 for the nucleus, and 1.42 for the mitochondria. The surrounding medium has a refractive index of 1.334. The AVS (Advanced Visualization System Inc.) visualizations of the representative 3D biological cell models are shown in Figs. 7.2(a) and (b). Figure 7.2(a) is for randomly distributed mitochondria (cancer cell) in a white blood cell. There are 36 mitochondria in zone I, 67 in zone II, and 77 in zone III. The mitochondrial aggregation to the nuclear periphery (normal cell) is shown in Fig. 7.2(b). There are 142 mitochondria in zone I, 33 in zone II, and 5 in zone III. With the same random seed as in Fig. 7.2(a) and (b), a model of mitochondria aggregate

to the cell membrane has 0 mitochondria in zone I, 13 in zone II, and 167 in zone III. Note the mitochondria number changes in zone I from Fig. 7.2(a) to Fig. 7.2(b). In Figs. 7.2(a) and (b), different colors are used to denote the mitochondria distributed in different zones.

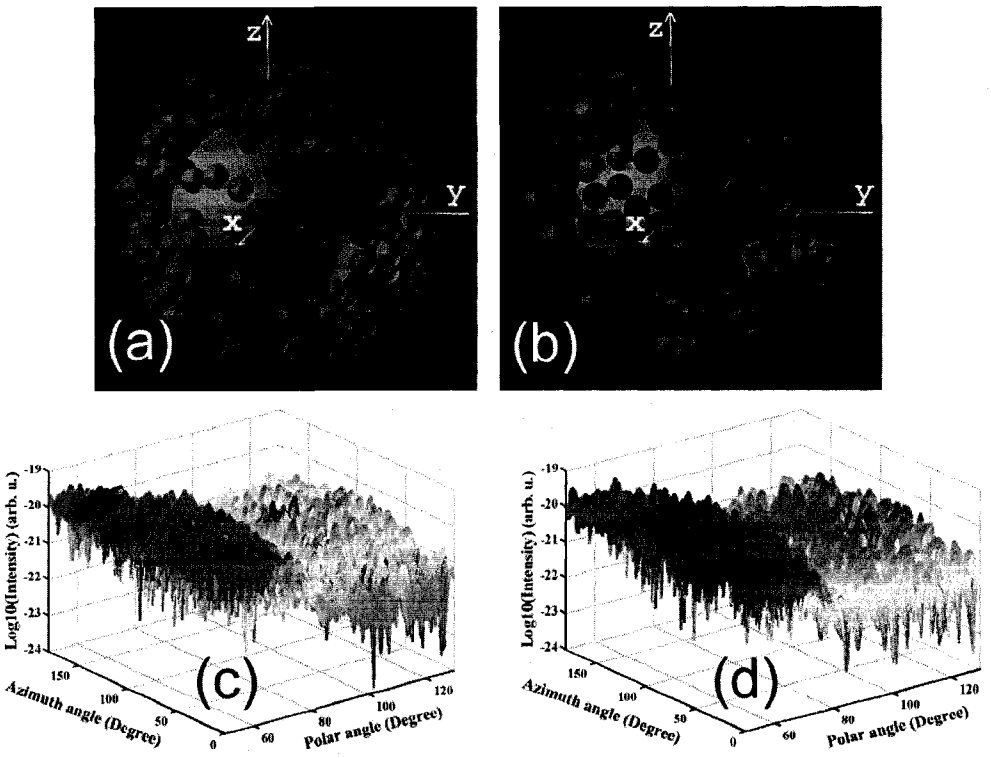

Figure 7.2 3D biological cell models and their FDTD 3D scatter spectra. (a), randomly distributed mitochondria in a white blood cell. (b), mitochondrial aggregation to the nuclear periphery in a white blood cell. Blue spheres denote the mitochondria centered in zone I, green in zone II, and red in zone III. The cell has a nucleus (cyan color) centered at the origin. The cell cytoplasm is shown in magenta. (c), FDTD 3D light scattering pattern for cell model (a). (d), FDTD 3D light scattering pattern for cell model (b).

7.3 Small angle forward scattering to differentiate normal cell models from cancerous cell models

Three dimensional Finite-Difference Time-Domain (FDTD)[21, 23] simulations are used to study light scattering from different mitochondrial distributions in single cells. Owing to recent advancements in computational technology, the FDTD

method can be used to simulate cells using nanometer space steps, which will cover the typical organelle sizes found in a biological cell.[21, 23] We use a spatial size of $\lambda/15$, where λ is the wavelength of the incident laser (here $\lambda = 632.8\,\text{nm}$). The geometry for the FDTD simulation is shown in Fig. 7.1. The incident plane wave has a wave vector $\hat{k}_i$ along the $\hat{z}$ direction, and is polarized along the $\hat{x}$ direction. The scattered wave $\hat{k}_s$ has an azimuth angle φ, and a polar angle θ.

In order to study the mitochondrial aggregation effects in biological cells, eight different random seeds are used to generate the cell models. For each random seed, we will have three different cell models as guided by Equation 7.1 to Equation 7.3. In order to show the organelle' effect, a cell model without organelles is also generated. This cell model is homogeneous, with a radius of 5μm and a refractive index of 1.38. Three dimensional FDTD simulations are then performed on these different cell models. The representative scatter patterns for the cell models Figs. 7.2(a) and (b) are shown in Figs. 7.2(c) and (d), respectively. These 3D scatter patterns contain rich information about the biological cell models. As a first step, in the study that follows, we perform an analysis of the scattered light for a given range of polar angle θ with the azimuth angle fixed at $\varphi = 90$ degrees.

In Fig. 7.3, we show the light scattering spectra of different cell models in different angular ranges. All the light scattering spectra are normalized so that the integrated area under the light scattering spectrum in the angular range from 0~130 degrees of the cell model without organelles is equal to "1". The light scattering spectra for the random distribution of mitochondria and mitochondrial aggregation to the nucleus shown in Fig. 7.3(a) are for the cell models Fig. 7.2(a) and (b), respectively. In Fig. 7.3(b), the cases for different mitochondrial distributions are shown in the angular range 0~10 degrees. Notice that the light scattering intensity distributions in the small angle forward scattering are quite distinctive for different cases. For each case of mitochondrial distribution in Fig. 7.3(b), there are eight different realizations. Figure 7.3(c) shows the results for the

eight different realizations of random distribution of mitochondria at very small angles. Figure 7.3(d) shows these eight different realizations around the 90^0 scatter from 85 to 95 degrees.

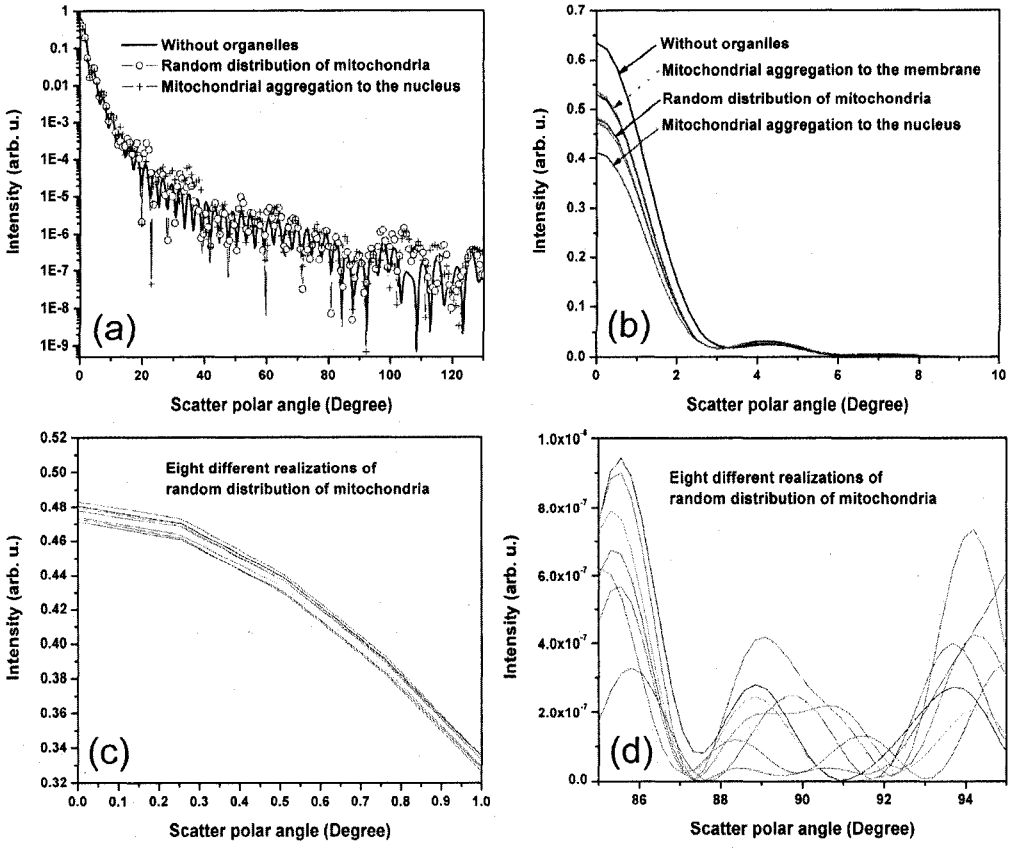

Figure 7.3 Light scattering spectra in different angular ranges. (a), light scattering spectra from different cell models in the scatter angular range 0~130 degrees. (b), light scattering spectra from different cell models in the scatter angular range 0~10 degrees. (c), results for the case of random distribution of mitochondria as shown in (b) at very small angles. (d), eight realizations of random distribution of mitochondria in the scatter angular range 85~95 degrees.

Two-parameter histograms have been used in cytometry to give better understanding of the cellular measurements.[27] In Fig. 7.4, we construct two-parameter light scattering histograms based on the FDTD simulation of different cell models. The vertical axis shows the integration of the scattered light in the small angle forward scattering (approximately 0~5 degrees), while the horizontal

axis shows the integration of light scattering around the 90 degree scatter (85~95 degrees). The histograms show that the different mitochondrial distributions can be well differentiated.

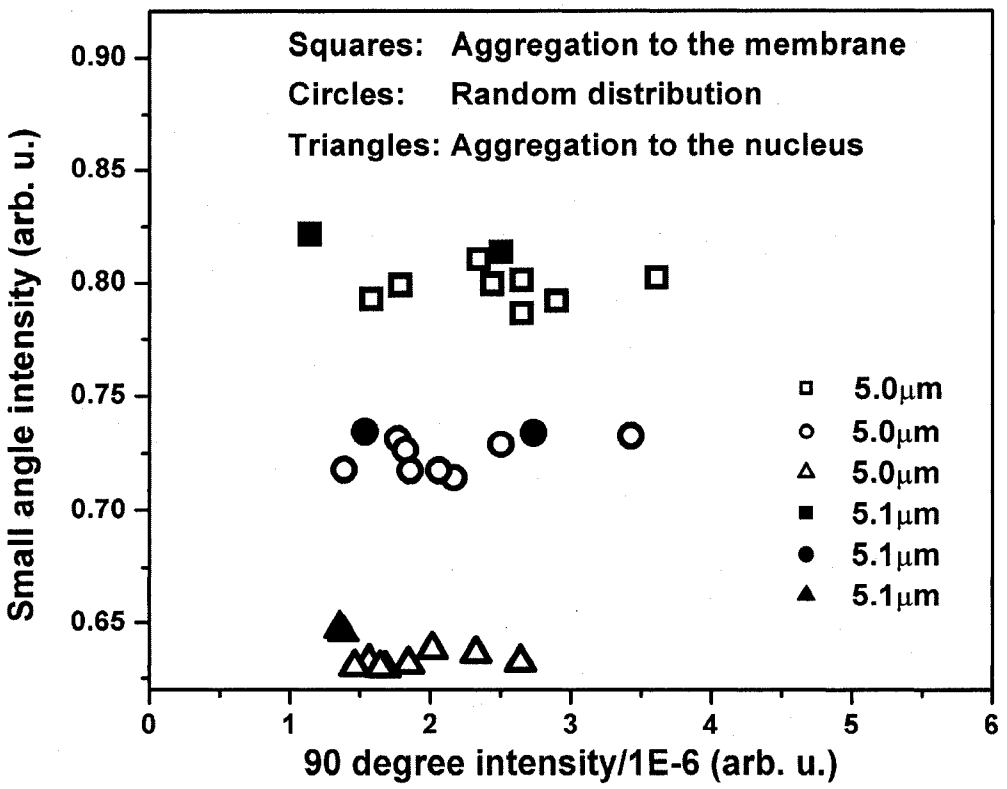

Figure 7.4 Two-parameter histograms to differentiate normal cell models from cancerous cell models.

The three different mitochondrial distribution cases that are considered lead to different results along the horizontal axis as shown in Fig. 7.4. However the more distinctive differences between the three cases are along the vertical axis, which is in the small angle forward scattering. To quantify the difference between normal cell models and cancerous cell models, the mean and standard deviation (SD) of the intensity of different cases are calculated. For the case of mitochondrial aggregation to the cell membrane (cancerous cell models), the mean is 0.79788 (arb. u.) with a SD of 0.00728 (arb. u.). The mean is 0.72344 (arb. u.) with a SD

of 0.00729 (arb. u.) for the case of random distribution of mitochondria (cancerous cell models), while the mean is 0.6326 (arb. u.) with a SD of 0.00307 (arb. u.) for the case of mitochondrial aggregation to the nucleus periphery (normal cell models). The differences between the means of the normal cell models and cancerous cell models are 0.16528 (arb. u.) and 0.09084 (arb. u.), which are at least 10 times bigger than any SD of the three different cases of mitochondrial distribution. The effects of cell size variations on the intensity integration are also considered as shown in Fig. 7.4 with solid signs. The normal cell models can be well differentiated from the cancerous ones for a cell volume variation of 6.12% as considered here. In this case, the small angle forward scattering can be used to differentiate the normal cell models from cancerous cell models.

7.4 Fourier transform of wide angle side scattered light for biological cell size determination

In conventional cytometry, the measurements of the small angle forward scattering intensity (0~5 degrees) are used to determine cell sizes.[27-29] The above results in this chapter have shown that the mitochondrial distributions in a biological cell can change the small angle forward scattering intensity distributions. This usual method is not accurate for biological cell size measurements.[27, 29]

We have recently developed a Fourier method for size determination of micro-scale beads.[30] This was discussed in Chapter 4 and was further applied in Chapter 6 to size yeast cells. However the micro-scale beads are homogeneous spheres and the yeast cells can be treated as homogeneous ellipsoids. Following we introduce the Fourier analysis of biological cells with complex inner structures.

Figure 7.5(a) shows the light scattering spectra of different cell models in the wide angle side scatter range (57.5~122.5 degrees). The cell model without organelles, the cell model with randomly distributed mitochondria and the cell

model with mitochondrial aggregation to the nucleus are the same as used for Fig. 7.3(a). The cell model with mitochondrial aggregation to the membrane was discussed in section 7.2. Fourier transforms are performed on these light scattering spectra (Fig. 7.5(a)) and are shown in Fig. 7.5(b). The Fourier spectra show that there is always a typical peak for the different cell models at frequency 0.32 (1/Degree). This highest dominant frequency determines the scatterer size,[30] and here corresponds to the overall size of the biological cells. Compared with the Fourier spectra from the cell model without organelles, the mitochondria inside biological cells mainly contribute to frequency components lower than this typical peak frequency.

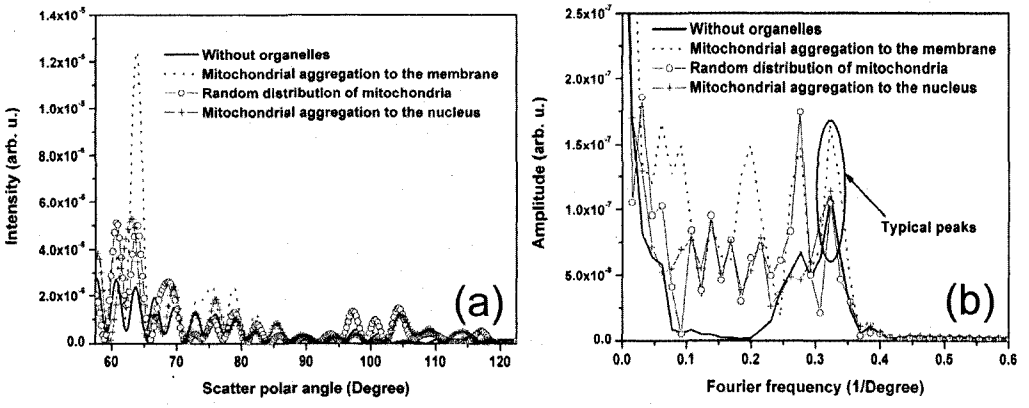

Figure 7.5 A Fourier method for better determination of biological cell sizes. (a), light scattering spectra from different cell models in the angular range 57.5~122.5 degrees. (b), Fourier transforms of the light scatter spectra as shown in (a).

Fourier analyses are also performed for the eight realizations of randomly distributed mitochondria in biological cell models used in Fig. 7.3. Figure 7.6(a) shows the light scattering spectra from these eight realizations in the angular range 57.5~122.5 degrees and Fig. 7.6(b) shows the Fourier spectra. The results further confirm that the typical peak at a frequency 0.32 (1/Degree) can be used to determine the biological cell size, while the inner organelles contribute to the lower frequency components.

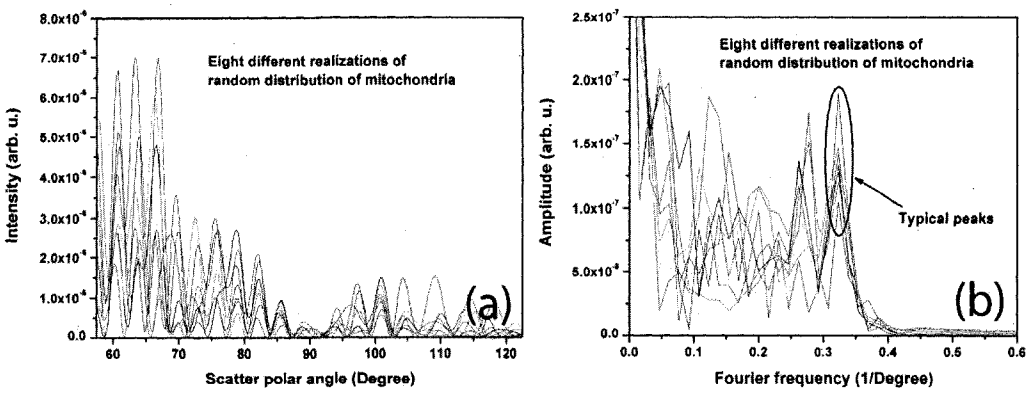

Figure 7.6 Different random distributions of mitochondria with the same typical peak frequency. (a), eight different realizations of random distribution of mitochondria. (b), Fourier transforms of the light scattering spectra in (a).

7.5 Conclusions

Different cell models were developed to simulate normal cells and cancerous cells. Three dimensional FDTD simulations were performed on these different cell models to obtain the light scattering patterns. Analyses of the FDTD light scattering spectra show that the small angle forward scattering can be used to differentiate normal cell models from cancerous cell models. Compared with the fluorescence technique, this method may be used as a non-invasive technique for precancerous cell detection in clinics. Our current integrated cytometer can not measure this small angle forward scattering. Future development of our cytometer will be able to measure both the small angle forward scattering and wide angle side scattering. For example, our current 4.6mm (H) CCD detector can be used to measure small angle forward scattering excited by a focused laser beam (for example, 300μm in diameter) from approximately 0.5 to 5 degrees, by putting the CCD screen perpendicular to the illumination laser beam with an offset of 500μm away from the laser beam central line.

The mitochondrial distributions inside biological cells change the small angle forward scatter intensity distributions. The measurements of the small angle forward scatter intensity to determine cell sizes may not always be an accurate

method if the mitochondrial distributions are unknown. Here we showed that the highest dominant frequency of the wide angle side-scatter Fourier spectra can be used to determine the biological cell sizes, while the mitochondria mainly contribute to the lower frequency components. Future analysis of the lower frequency components in the Fourier spectra will help provide a better understanding of mitochondrial effects inside biological cells.

7.6 References

1. G. M. Cooper and R. E. Hausman, *The cell: A molecular approach*, (ASM Press, Washington, D. C., 2004).

2. J. F. R. Kerr, C. M. Winterford and B. V. Harmon, "Apoptosis - Its Significance in Cancer and Cancer-Therapy," *Cancer* **73**, 2013-2026 (1994).

3. G. I. Evan and K. H. Vousden, "Proliferation, cell cycle and apoptosis in cancer," *Nature* **411**, 342-348 (2001).

4. D. R. Green and G. I. Evan, "A matter of life and death," *Cancer Cell* **1**, 19-30 (2002).

5. S. Desagher and J. C. Martinou, "Mitochondria as the central control point of apoptosis," *Trends in Cell Biology* **10**, 369-377 (2000).

6. K. Li, Y. C. Li, J. M. Shelton, J. A. Richardson, E. Spencer, Z. J. Chen, X. D. Wang and R. S. Williams, "Cytochrome c deficiency causes embryonic lethality and attenuates stress-induced apoptosis," *Cell* **101**, 389-399 (2000).

7. J. Yang, X. S. Liu, K. Bhalla, C. N. Kim, A. M. Ibrado, J. Y. Cai, T. I. Peng, D. P. Jones and X. D. Wang, "Prevention of apoptosis by Bcl-2: Release of cytochrome c from mitochondria blocked," *Science* **275**, 1129-1132 (1997).

8. R. M. Kluck, E. BossyWetzel, D. R. Green and D. D. Newmeyer, "The release of cytochrome c from mitochondria: A primary site for Bcl-2 regulation of apoptosis," *Science* **275**, 1132-1136 (1997).

9. N. Haga, N. Fujita and T. Tsuruo, "Mitochondrial aggregation precedes cytochrome c release from mitochondria during apoptosis," *Oncogene* **22**, 5579-5585 (2003).

10. A. S. Don and P. J. Hogg, "Mitochondria as cancer drug targets," *Trends in Molecular Medicine* **10**, 372-378 (2004).

11. N. Haga, N. Fujita and T. Tsuruo, "Involvement of mitochondrial aggregation in arsenic trioxide (As2O3)-induced apoptosis in human glioblastoma cells," *Cancer Science* **96**, 825-833 (2005).

12. W. D. Thomas, X. D. Zhang, A. V. Franco, T. Nguyen and P. Hersey, "TNF-related apoptosis-inducing ligand-induced apoptosis of melanoma is associated with changes in mitochondrial membrane potential and perinuclear clustering of mitochondria," *Journal of Immunology* **165**, 5612-5620 (2000).

13. L. Y. Liu, A. Vo, G. Q. Liu and W. L. McKeehan, "Distinct structural domains within C19ORF5 support association with stabilized microtubules and mitochondrial aggregation and genome destruction," *Cancer Research* **65**, 4191-4201 (2005).

14. T. N. Moss, A. Vo, W. L. McKeehan and L. Y. Liu, "UXT (Ubiquitously Expressed Transcript) causes mitochondrial aggregation," *In Vitro Cellular & Developmental Biology-Animal* **43**, 139-146 (2007).

15. K. De Vos, V. Goossens, E. Boone, D. Vercammen, K. Vancompernolle, P. Vandenabeele, G. Haegeman, W. Fiers and J. Grooten, "The 55-kDa tumor necrosis factor receptor induces clustering of mitochondria through its membrane-proximal region," *Journal of Biological Chemistry* **273**, 9673-9680 (1998).

16. Y. K. Suen, K. P. Fung, Y. M. Choy, C. Y. Lee, C. W. Chan and S. K. Kong, "Concanavalin A induced apoptosis in murine macrophage PU5-1.8 cells through clustering of mitochondria and release of cytochrome c," *Apoptosis* **5**, 369-377 (2000).

17. P. L. Gourley, J. K. Hendricks, A. E. McDonald, R. G. Copeland, K. E. Barrett, C. R. Gourley and R. K. Naviaux, "Ultrafast nanolaser flow device for detecting cancer in single cells," *Biomedical Microdevices* **7**, 331-339 (2005).

18. A. Dunn and R. Richards-Kortum, "Three-dimensional computation of light scattering from cells," *IEEE Journal of Selected Topics in Quantum Electronics* **2**, 898-905 (1996).

19. J. R. Mourant, J. P. Freyer, A. H. Hielscher, A. A. Eick, D. Shen and T. M. Johnson, "Mechanisms of light scattering from biological cells relevant to noninvasive optical-tissue diagnostics," *Applied Optics* **37**, 3586-3593 (1998).

20. R. Drezek, A. Dunn and R. Richards-Kortum, "A pulsed finite-difference time-domain (FDTD) method for calculating light scattering from biological cells over broad wavelength ranges," *Optics Express* **6**, 147-157 (2000).

21. C. G. Liu, C. Capjack and W. Rozmus, "3-D simulation of light scattering from biological cells and cell differentiation," *Journal of Biomedical Optics* **10**, 014007 (2005).

22. V. Backman, R. Gurjar, K. Badizadegan, L. Itzkan, R. R. Dasari, L. T. Perelman and M. S. Feld, "Polarized light scattering spectroscopy for quantitative measurement of epithelial cellular structures in situ," *IEEE Journal of Selected Topics in Quantum Electronics* **5**, 1019-1026 (1999).

23. J. Q. Lu, P. Yang and X. H. Hu, "Simulations of light scattering from a biconcave red blood cell using the finite-difference time-domain method," *Journal of Biomedical Optics* **10**, 024022 (2005).

24. X. T. Su, C. Capjack, W. Rozmus and C. Backhouse, "2D light scattering patterns of mitochondria in single cells," *Optics Express* **15**, 10562-10575 (2007).

25. X. T. Su, K. Singh, W. Rozmus, C. Backhouse and C. Capjack, "Light scattering analysis of mitochondrial aggregation in single cells for cancer detection," (in preparation).

26. R. H. Carlson, C. V. Gabel, S. S. Chan, R. H. Austin, J. P. Brody and J. W. Winkelman, "Self-sorting of white blood cells in a lattice," *Physical Review Letters* **79**, 2149-2152 (1997).

27. H. M. Shapiro, *Practical flow cytometry*, (John Wiley & Sons, Inc., Hoboken, 2003).

28. P. F. Mullaney, M. A. Vandilla, J. R. Coulter and P. N. Dean, "Cell Sizing - a Light Scattering Photometer for Rapid Volume Determination," *Review of Scientific Instruments* **40**, 1029-& (1969).

29. M. Kerker, H. Chew, P. J. McNulty, J. P. Kratohvil, D. D. Cooke, M. Sculley and M. P. Lee, "Light-Scattering and Fluorescence by Small Particles Having Internal Structure," *Journal of Histochemistry & Cytochemistry* **27**, 250-263 (1979).

30. X. T. Su, K. Singh, C. Capjack, J. Petracek, C. Backhouse and W. Rozmus, "Measurements of light scattering in an integrated microfluidic waveguide cytometer," *Journal of Biomedical Optics* (accepted).

Chapter 8

Conclusions

8.1 Summary

This dissertation presents a 2D cytometric technique for the study of light scattering from a single scatterer. An integrated microfluidic waveguide cytometer was developed for the measurements of light scattering from single scatterers. Theoretical studies were performed to validate the experimental light scattering measurements. This 2D cytometric technique can be of great interest for better understanding of the light scattering properties and for cellular diagnostics in clinics.

In Chapter 2 theoretical backgrounds for the study of light scattering were introduced. The Mie code that is used in this dissertation was validated by comparing with published results from other research groups. A limitation of the Mie code is that it only gives the solution for light scattering from a single homogeneous spherical scatterer that is illuminated by a plane wave. The FDTD code can be used to give numerical solutions of light scattering from inhomogeneous biological cells. The FDTD code was validated for both the microscale cell sizes and nanoscale organelle sizes by comparing results with the Mie simulations.

The development of an integrated microfluidic waveguide cytometer was described in Chapter 3. A UV-curable epoxy edge bonding method was developed for the fabrication of the microchips designed for light scattering measurements.

The chip fabrication method together with the specially designed microsize observation window makes the detection of the weakly scattered side-scatter light possible. A prism-coupling technique was adopted for illuminating the scatterers in the microfluidic channel with laser light. A simple but effective pressure control method enabled immobilization of a single microsize scatterer in the observation window area for a period of 1/4 second. Finally, the integrated cytometer was built up on an optical bench in a dark room which also serves as a high energy laser control area. This novel cytometer can image a single microsize scatterer in a fluidic flow by using a digital camera, while simultaneously obtaining its 2D side-scatter patterns by using a CCD detector.

In Chapter 4, 2D side-scatter patterns of microsize polystyrene beads were obtained and the experimental results were validated by comparing with the Mie theory simulations. Modal analysis of the planar waveguide showed that a plane wave excitation of the microsize scatterers in the cytometer can be assumed. The all planar structure of the device without any optical lens between the scatterer and the CCD detector simplified the application of Mie theory in the experimental apparatus. Two-dimensional side-scatter patterns from different size polystyrene microbeads were obtained. The 2D scatter patterns are symmetric about the azimuthal angle at 90 degrees. The vertical fringes in the 2D scatter patterns were used to infer the location of the 90 degree in polar angle. Good agreements between the experimental and Mie theory results were obtained in both the space and Fourier domains. A Fourier method was developed for microsize differentiation with the integrated cytometer.

The dependence of the light scattering on the incident wave polarizations and the inhomogeneous scatterers was studied in Chapter 5. An incident laser with a polarization angle of 0^0 provides better results compared with a polarization angle of 90^0 from an experimental side. In order to study the light scattering dependence on non-homogeneous scatters with the integrated cytometer, a simple geometric method was developed to transfer the FDTD spatially distributed intensity onto a

plane CCD. The FDTD 2D scatter patterns agree well with the 2D polystyrene microbead scatter patterns obtained with the integrated cytometer. Randomly distributed mitochondria have been shown to break the azimuthal symmetry of the 2D light scattering patterns. These are of interest for the study of real biological cells.

In Chapter 6 light scattering measurements were performed on yeast and human cells with the integrated cytometer and the experimental results were compared with FDTD simulations. Clear fringes were obtained in the 2D light scatter patterns from yeast cells, while the 2D scatter patterns from human Raji cells consisted of small scale 2D structures. Different cell models were generated for the FDTD simulations on yeast and Raji cells. The FDTD simulations together with the experimental results showed that the microstructures (*e.g.* cell cytoplasm and/or nucleus) generate the fringes, while the randomly distributed mitochondria in single cells generate the small scale 2D structures. The FDTD simulations on the ellipsoidal yeast cell models also showed that cell orientation effect will not generate the small scale 2D structures. The analysis of the small scale 2D structures that dominate the 2D human cell scatter patterns may ultimately be a useful diagnostic technique for mitochondrial differentiation in single cells. The Fourier method developed in Chapter 4 was applied to size yeast cells. The estimation of yeast cells by using the Fourier method agrees with the measurements under an Axiovert microscope.

Finally, the application of the light scattering technique for precancerous detection was studied in Chapter 7. Different 3D cell models were developed to mimic normal cell and cancerous cell statuses. FDTD simulations were then performed to obtain scatter spectra from these different cell models. Our results showed that the small angle forward scattering can be used to differentiate normal cell models (mitochondrial aggregation to the nucleus) from cancerous cell models (mitochondria randomly distributed inside the cells). Since the mitochondria can change the small angle forward scattering intensity dramatically,

the measurements of small angle forward scattering intensity may not always be an accurate method to determine cell sizes. Fourier analysis of wide angle side scatter spectra showed that the highest dominant frequency can be used to better determine the cell sizes. The mitochondria inside biological cell mainly contribute to lower frequency components.

8.2 Future work

The novel 2D cytometric technique developed in this work can be used for microscopic particle and biological cell analyses. The integrated cytometer can be further developed to obtain very wide angular range light scattering patterns. For example, if the scattered light passed through only a 100μm water layer onto a 4.6mm (H) CCD detector, light scattering over a wide angular range from approximately 2.5^0 to 177.5^0 can be obtained. The wider angular range light scattering will contain richer information about the scatterers. Automating the immobilization and the observation of single scatterers would allow the device to process cells faster and more efficiently. This 2D cytometric technique can be very useful in cellular diagnostics and clinical applications.

The integrated mcirofluidic waveguide cytometer can be miniaturized as a handheld apparatus. The ultimate goal would be to develop a portable and inexpensive cytometer with an embedded analysis software package. This requires especially new developments of methods to excite and image the scatterer. Most of these elements can be integrated on a chip ("lab-on-a-chip") with the current development of microfabrication technology.

The analysis of the scatter patterns in multi-dimensions will enable a better understanding of the scatterer properties especially for biological cells. The future development of algorithms to perform 2D space domain or Fourier domain analysis of the scatter patterns can be used to obtain such an understanding. The novel 2D cytometric technique can be developed to obtain 3D scatter patterns. The 3D cytometric technique would be able to obtain scatter patterns containing

more information about the scatterers. All these are related to a very interesting field of solving the inverse scatter problems.

The integration of the near field optics technology in the future experimental development will be of great interest. Near-field scanning optical microscopy (NSOM) can obtain a resolution of several nanometers that breaks the diffraction limit of conventional optics, which depends on the detection of the near field scattered light. The FDTD method can be used to obtain the near field scatter patterns. This will give better understanding of the NSOM technology. Secondly, it is very challenging to obtain virus information in conventional cytometers because of background scattering of the apparatus. An evanescent field as a probe, generating a dark experimental background, has the potential to obtain virus information. Such an understanding can be improved by FDTD simulations. Furthermore, surface plasmon resonance (SPR) sensors, which use evanescent light to excite the resonance, have wide applications in protein and DNA analyses. The development of evanescent field apparatus together with FDTD simulations will contribute to the SPR technique.